THE UNIVERSITY OF QUEENSLAND
AUSTRALIA

Magnetic Resonance Characterisation of Developing Hepatocellular Carcinoma in a Diet Induced Model of Liver Cancer in the Rat

By
Sami Abdulkarim Alghamdi

Bachelor degree of Radiological Science

Master of Magnetic Resonance Technology

Thesis submitted for the degree of Doctor of Philosophy at
The University of Queensland in 2017
Queensland Brain Institute (QBI)
Centre for Advanced Imaging (CAI)

Abstract

Non-alcoholic fatty liver disease (NAFLD), a disorder associated with abnormal lipid accumulation within hepatocytes, is considered benign disorder in nature. However, in some cases it may progress to inflammation, nonalcoholic steatohepatitis (NASH), then cirrhosis, precancerous nodules and finally to hepatocellular carcinoma (HCC). NAFLD and NASH are both reversible with appropriate clinical intervention and lifestyle changes. In developed countries, the non-alcoholic fatty liver disease (NAFLD) is becoming one of the most common causes of precancerous and HCC lesions [1]. Unfortunately, most nodular lesions are detected too late with a poor prognosis. The discovery of markers that can predict which livers may progress to HCC would allow early intervention and potentially halting progress to HCC. This would be of great benefit at any stage up to precancerous lesions, however the earlier the better. Development of end stage liver malignancy would be decreased, resulting in decreased mortality from this disease.

Histology is considered the reference standard for the assessment of fatty disease and nodular lesion in liver. However, there are significant drawbacks including invasiveness, small sample size and observer-dependence which limits its usefulness in evaluating liver disease. Magnetic resonance imaging is a non-invasive modality that can provide information on anatomical and physiological changes in the liver (e.g. fatty liver disease and HCC). MRI images are primarily assessed visually by expert radiologists looking for anatomical and contrast changes in the images compared to normal tissue. This qualitative method requires inspection of all datasets for abnormalities. Visual interpretation is subjective, labour intensive, and depends on the experience of the radiologist. This can introduce inter-observer variation and is suitable only when the pathology leads to sufficient contrast changes in the images acquired.

MRI also allows the calculation of quantitative parameters like T_1, T_2 and diffusion values. These parameters are dependent on physical, chemical and microstructural properties of the tissue. When standard protocols are used, the calculation of these parameters should be independent of the observer. This has the potential for more precise characterization of changes that occur over time. Clinically, here has been limited utilization of these methods, as they generally require longer acquisition times and significant post processing of the images. However, with each release of new scanners, hardware and software updates are making quantitative imaging more accessible in the clinical setting.

This thesis investigates changes in multi-exponential derived T_2 components and the

fat fraction (FF) in the liver during progression of liver disease in a rat model. The choline-deficient L-amino acid (CDAA) rat model of liver cancer exhibits the same progression of liver disease as in humans including NAFLD to NASH, fibrosis, cirrhosis, precancerous lesions and finally full HCC. This allows longitudinal characterisation of T_2 components and FF during the progression through various stages of liver disease. Changes in these components individually and/or the relationship between these components may provide an indication for tissue regions that are at risk of progressing to the next stage and ultimately to HCC. After completion of *in vivo* MR experiments, all rats were sacrificed and livers taken for *ex vivo* imaging on a 16.4T scanner and histologic evaluation. This thesis aims to develop new MR biomarkers to assess progression of liver disease.

Declaration by author

This thesis is composed of my original work, and contains no material previously published or written by another person except where due reference has been made in the text. I have clearly stated the contribution by others to jointly authored works that I have included in my thesis.

I have clearly stated the contribution of others to my thesis as a whole, including statistical assistance, survey design, data analysis, significant technical procedures, professional editorial advice, and any other original research work used or reported in my thesis. The content of my thesis is the result of work I have carried out since the commencement of my research higher degree candidature and does not include a substantial part of work that has been submitted to qualify for the award of any other degree or diploma in any university or other tertiary institution. I have clearly stated which parts of my thesis, if any, have been submitted to qualify for another award.

I acknowledge that an electronic copy of my thesis must be lodged with the University Library and, subject to the General Award Rules of The University of Queensland, immediately made available for research and study in accordance with the Copyright Act 1968 unless a period of embargo has been approved by the Dean of the Graduate School.

I acknowledge that copyright of all material contained in my thesis resides with the copyright holder(s) of that material. Where appropriate I have obtained copyright permission from the copyright holder to reproduce material in this thesis.

Publications during candidature

Conference Abstracts

- Sami Alghamdi, Gary Cowin, Ian Brereton, and Yasvir Tesiram. Magnetic resonance biomarkers of altered lipid metabolism during liver cancer development. Traditional poster presented to International Biophysics Congress, Brisbane, Australia, August 3-7, 2014
- Sami Alghamdi, Gary Cowin, Ian Brereton, and Yasvir Tesiram. T2 relaxation time and fat fraction analysis of *in vivo* hepatocellular carcinoma in a rat model at 9.4 T. Traditional poster presented to ANZMAG conference, Bay of Islands, New Zealand, 29 November-3 December, 2015.
- Sami Alghamdi, Gary Cowin, Ian Brereton, and Yasvir Tesiram. Measurement of Liver Fat Fraction and T2 Relaxation Times in an Experimental Rat Model of Hepatocarcinogenesis at 9.4T. Presented to International Society for Magnetic Resonance in Medicine (ISMRM) conference in an oral scientific session, Singapore, May 7-13, 2016.

Publications included in this thesis

No publications.

Contributions by others to the thesis

No contributions by others.

Statement of parts of the thesis submitted to qualify for the award of another degree

None

Acknowledgments

First and foremost, I offer my sincerest gratitude to my PhD supervisory team, Dr. Yasvir Tesiram (principle advisor), Dr. Gary Cowin (associate advisor), Prof. Ian Brereton (associate advisor) for supporting me during these past 4 years. My deep acknowledgment goes to my principal supervisor Dr Yasvir who has supported me throughout my thesis with his patience and knowledge. He is the funniest advisor and one of the smartest people I know. He is someone you will instantly love and never forget once you meet him. He provided me with the opportunity, the guidance, and the support to succeed at every stage of my PhD. I really appreciate his willingness to meet me with a short talk outside the CAI centre every day and going through several ideas about my research. He taught me how to write academic papers and was always there to proofread and mark up my papers and thesis. I hope that I could be as enthusiastic and energetic as him and to someday be able to convince an audience as well as he can. I am also grateful to Dr. Gary Cowin who has been supportive and has given me the freedom to discuss various projects without objection. My gratitude to him for his flawless grammatical editing and proofreading of my thesis. He has also provided me with scientific advice and knowledge and suggestions. Special thanks also given to Prof. Ian who helped me to find a PhD place when I expressed my desire to peruse my PhD research at the University of Queensland. I was so lucky when he accepted me and being one of my supervisory team. His encouragement and support never stopped during my PhD journey which made me confident to fulfil my desire and overcome any difficult moment. I am amazed that despite his busy schedule, he was able to go through any documents including papers for publication, conference posters, and thesis; and send me back within few days with comments and suggestions on almost every page. He is an inspiration.

Besides my advisors, I would like to thank the thesis committee: Dr. Katie McMahon, Dr. Mark Wellard, and Dr. Jeffery Harmer, for their encouragement, insightful comments, and Feedback every year during my PhD period.

I want to acknowledge Dr. Chiara Palmieri, a veterinary pathologist, for helping me to perform the histology of the tissue samples and analyse them.

Also, I would like to acknowledge the Saudi Government Scholarship provided by King Saud University.

Many thanks my parents who have sacrificed their lives for my brothers, sisters, and myself and provided unconditional love and care. Thank you my mother (Refah) and father

(Abdulkarim) who instilled within me a love of creative pursuits, science and language, all of which finds a place in this thesis.

I also dedicate this Ph.D. thesis to my two lovely children, Abdulkarim (6 years old) and Amal (4 years old) who are the pride and joy of my life. I love you more than anything and I appreciate all your patience and support during father's Ph.D. journey.

Keywords

Non-alcoholic fatty liver disease, Nodular lesion, Magnetic resonance imaging, Dixon method, T_2 mono- and bi-exponential models, Choline-deficient L-amino acid-defined diet, Choline-supplemented L-amino acid-defined.

Australian and New Zealand Standard Research Classifications (ANZSRC)

Fields of Research:

ANZSRC code:, 110104 Medical Biochemistry: Lipids 30%

ANZSRC code:, 110320 Radiology and Organ Imaging 30%

ANZSRC code:, 110307 Gastroenterology and Hepatology 20 %

ANZSRC code: 111202 Cancer Diagnosis 20 %

Fields of Research (FoR) Classification

FoR code: 1112 Oncology and Carcinogenesis 60%

FoR code: 1103 Clinical Sciences 40%

Table of Contents

List of Tables

List of Figures

List of Acronyms & Abbreviations

MRI	Magnetic resonance imaging
MRS	Magnetic resonance spectroscopy
DW-MRI	Diffusion-weighted magnetic resonance imaging
HCC	Hepatocellular carcinoma
SPIO	Super paramagnetic iron oxide
RF	Radiofrequency
TE	Echo time
TR	Repetition time
T1	Longitudinal relaxation time
T_2	Transverse relaxation time constant
Bi-T_2	Bi-component T_2
S0	Bulk signal intensity
T_{2L}	T_2 long
T_{2S}	T_2 short
ρ_L	Fractional contribution of the long decaying compartment to S_0
ρ_S	Fractional contribution of the short decaying compartment to S_0
FF	Fat fraction
C	Amplitude of baseline signal
ADC	Apparent Diffusion Coefficient
SD	Standard deviation
$\bar{\gamma}$	Gyromagetic ratio
B_0	Static magnetic field
$\Delta\delta$	Difference in chemical shift between water and lipid resonances
FA	Flip angle

2D	Two-dimensional
3D	Three-dimensional
9.4T	Operating magnetic field strength of 9.4 Tesla
16.4T	Operating magnetic field strength of 16.4 Tesla
MHz	Mega Hertz
rBW	Receiver bandwidth
ROI	Region of interest
ms	Milliseconds
SE	Spin echo
SNR	Signal to noise ratio
FLASH	Fast low angle shot gradient echo sequence
MESE	Multi-slice multi-echo spin echo sequence
ANOVA	Analysis of variance
r	Pearson correlation coefficient
AIC	Akaike information criterion
r^2	Coefficient of variation

Chapter 1 : Background

1.1 Introduction

Hepatocellular carcinoma (HCC) is a liver malignant tumour usually developing from a cirrhotic background [2]. The incident rate of HCC in the United States had tripled from 1975 through 2005 [3]. In Australia, the HCC was increased (tripled) between 1982 and 2007 (from 1.8 to 5.2 cases per 100,000 population) [4]. Risk factors for HCC mainly include hereditary haemochromatosis, hepatitis B and C, aflatoxin, drugs, and alcohol [5]. Pathologically, hepatocarcinogenesis is a stepwise development from regenerative nodule (RN) through dysplastic nodules (DN) to early HCC and then moderate to progressive HCC [6]. RN is considered a benign lesion and gives rise to hyperplastic nodules. DN is a premalignant nodule that contains atypical hepatic cells, without definite histological features of malignancy, which are thought to be the direct precursor of HCC. Currently most HCC are detected late leading to a poor prognosis. Early detection gives the opportunity for patients to receive potentially curative treatments. The five-year survival rate of 70% can be achieved with resection or transplant by detecting early stage of HCC [7, 8]. Diagnosis of HCC is no longer limited to invasive biopsy. Non-invasive imaging methods such as magnetic resonance imaging (MRI), ultrasound (US) and computer tomography (CT) are all being applied to detect late stage HCCs [9]. However, they are not highly sensitive for the early (premalignant stage) detection of HCC. Detection of hepatocarcinogenesis at earlier stages might help improve the clinical outcomes of HCC patients.

MR images can be sensitised to many biological characteristics of tissue using multiple sequences with and without MR contrast agents. Conventional T_2- or T_1-weighted MRI highlight anatomical changes to characterize hepatic nodules within a cirrhotic background [10, 11]. MR angiography using gadolinium agent contrast enhancement (CE) is a clinical imaging standard tool for evaluating and detection HCC based on blood supply and vascular integrity. Hepatocyte specific gadolinium contrast agents are concentrated in healthy hepatocytes increasing the contrast between healthy hepatocytes and nodules. Superparamagnetic iron oxides (SPIOs) accumulate in non-malignant lesions leading to decrease signal. Together these agents show potential to improve early detection of HCC [12].

Diffusion weighted imaging (DWI) has been applied with moderate success allowing better differentiation between solid benign and malignant lesions. DWI relies on differences in water diffusion and can provide quantitative (apparent diffusion coefficient; ADC) and qualitative information of cell membrane integrity and tissue cellularity which may help to differentiate between liver lesions [13].

MR spectroscopy (MRS) is a non-invasive technique that provides physiological and chemical information rather than anatomy in the living tissue, and is used diagnostically in brain [14], breast [15], and prostate [16]. In hepatic diseases, fatty changes and steatosis in a lipid-induced rat model have been intensively examined by MRS with few studies in patients and proven to be successful [17]. It has been reported that in an animal model of HCC metabolite signals including saturated and unsaturated lipids as well as choline play important roles in the process of hepatocarcinogenesis [18, 19]. These metabolites are potential biomarkers for evaluating HCC and are observable by MRS.

T_2 and T_1 relaxation times are sensitive to tissue structure, water freedom and tissue composition. The T_2 is determined by acquiring a series of images with increasing TE times. The T_1 value can be determined by acquiring a series of images with varying TR times, inversion times or pulse angles. Animal models of liver cancer suggest relaxation times are sensitive to tumour microenvironment. [20]. However, studies of relaxation time in animal liver cancer are still few and need further research.

It is important to understand the capabilities and limitations of current preclinical and clinical magnetic resonance (MR) protocols to identify gaps and opportunities for adding new methods to address unmet needs. A review of the development of hepatocellular carcinoma and an overview of the most currently available animal models of HCC will be presented. This will be followed by the current status of diagnostic MR methods including relaxation times, DWI, and MRS to evaluate hepatocarcinogenesis on the basis of several MR criteria using animal model of HCC.

1.2 Basic histopathological characteristic of hepatocellular carcinoma

Hepatocellular carcinoma (HCC) mainly develops in the setting of chronic liver disease and has an established pathway of hepatocarcinogenesis. The pathway of hepatocarcinogenesis shows various degrees of cytological atypia. Cells differ from normal cells beginning from precancerous nodules, including regenerative nodules (RN) and dysplastic nodules (DN), to early HCC and then moderate to progressive HCC [6]. The terminology of precancerous nodules is now standardised by International Working Party Classification (IWP) [21] which considers DNs, usually high grade, as a precursor of HCC and thus the confirmed gradual evolution of this carcinogenesis step is from DN to HCC. During this pathway unpaired arteries, due to angiogenesis, increases as the nodule develops [6, 22]. Histopathologically, the progression of HCC includes gradual diminution of portal tracts (hepatic artery and portal vein) which eventually become absent and is accompanied with with sinusoidal capillarization and growth of unpaired arteries (hypervascular tumor), whereas precancerous nodules are mainly supplied by the portal vein (hypovascular lesion) [23]. HCC can develop directly from non-malignant hepatocytes as opposed to DNs, and so called de *novo* hepatocarcinogenesis [24]. Both multistep and de *novo* hepatocarcinogenesis are shown in figure 1-1.

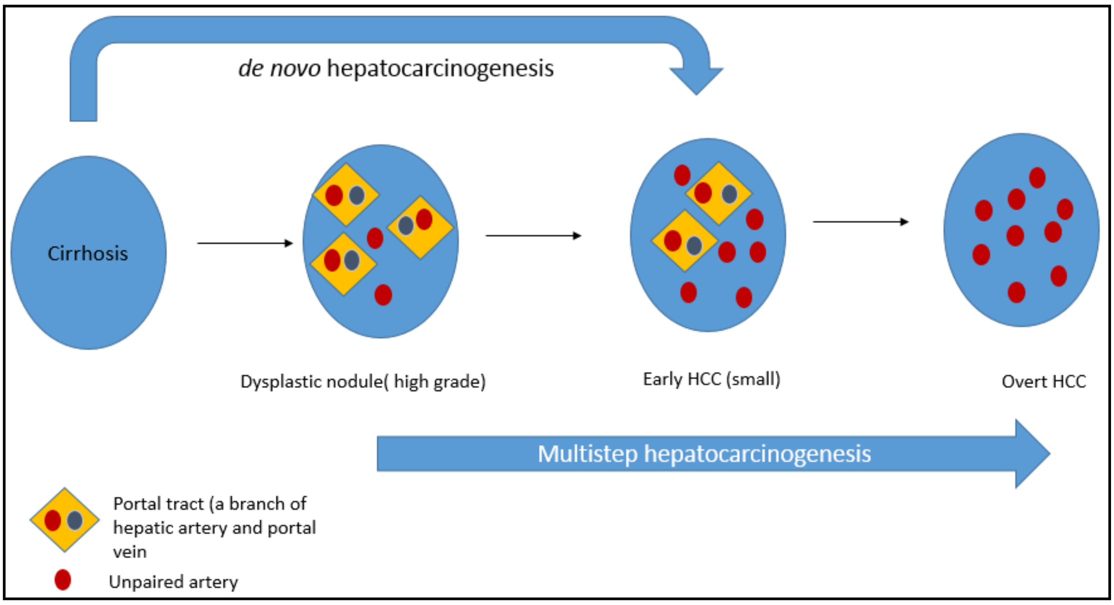

Figure 1-1: A simplified representation of the pathway of hepatocarcinogenesis. Unpaired arteries due to angiogenesis increases as nodules progress from high grade dysplastic nodule to HCC.

Small or early HCCs are characterised by well-differentiated lesions (closely resembling their tissue of origin), growing without substantial destruction of hepatic framework, and less chance of showing stromal invasion [25]. Small HCC in cirrhotic liver is usually preceded by the appearance of precancerous lesions including DN [6, 26]. Small HCCs have been classified into two types: *early vaguely nodular* with indistinct margins, and *progressed nodule* with distinct margins [27]. In early vague nodules, the nodular margins are indistinct owing to the lack of a tumour capsule. Other characteristics include increased nuclear to cytoplasmic ratio, and pseudoglandular structure [6, 26].

Fatty changes are frequently also observed in early HCC lesions [6, 28]. These fatty changes are mostly triglycerides and may be a biomarker of membrane breakdown (figure 1-2) [29]. Progressed small HCCs contain well to moderate differentiated cells rimmed often by fibrotic capsule. Fibrous capsule may be seen helping to differentiate HCC from DNs. Other abnormal changes such as hemorrhage, necrosis, fibrous septa and invasion of veins and bile ducts can also occur [30].

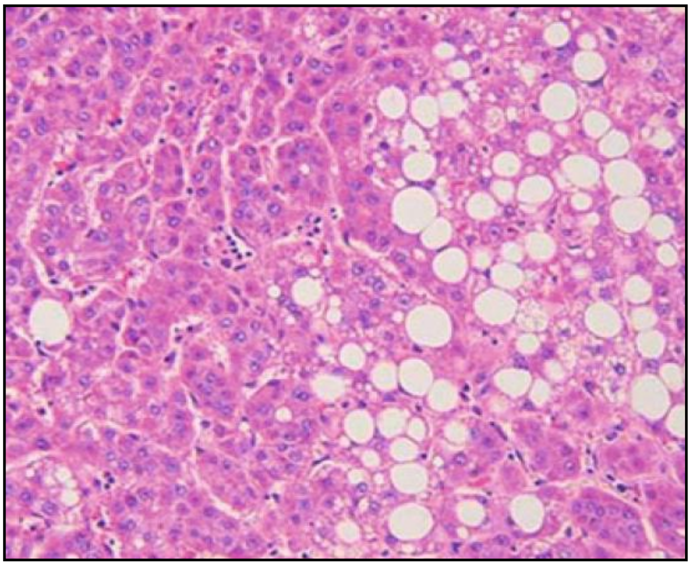

Figure 1-2: Early HCC nodule shows an irregular thin trabecular in the area where fatty change is located (right half image) [28].

1.3 Non-alcoholic fatty liver disease and HCC

The detection of fatty lesions is crucial during liver cancer development because it is considered to be a biomarker for malignant transformation of a DN to early HCC [31]. It has been observed that fatty change is frequently associated with small HCC in early stage development [32]. Fatty lesion is defined as an excess of fat accumulation (>5%), primarily as triglycerides, in the liver [33] which is associated with metabolic disorders that are related to insulin resistance and central obesity [34]. Moreover, non-alcoholic fatty liver disease (NAFLD) can increase the risk for HCC. NAFLD ranges from steatosis (simple fatty liver) to steatohepatitis (NASH). NASH involves steatosis and a specific form of inflammation with hepatocellular injury, which is commonly followed by progression to fibrosis, cirrhosis and hepatocellular carcinoma [35]. In simple steatosis, the rate of fatty acid accumulation that are imported or synthesised by hepatocytes will exceed the rate of export or catabolism, resulting in liver cells filled with multiple fat droplets [36, 37]. In NASH, the increase in fat accumulation is accompanied by various degrees of inflammation and fibrosis. Although non-alcoholic fatty accumulation generally is considered as benign, NASH increases the risk of cirrhosis and hepatocellular carcinoma [38]. HCC can develop in NAFLD without cirrhosis [39]. In human, a study reported that HCC can be associated with NAFLD in the absence of advanced hepatic fibrosis or cirrhosis [40]. The mechanisms responsible for this association are unknown, and more research are required to investigate mechanisms that promote HCC in NAFLD. Although, the progression of steatosis to cirrhosis through NASH and fibrosis has been characterized, no imaging-biomarkers have been found to accurately distinguish developmental stages of HCC, making liver biopsy the only reliable method of assessing the degree of NAFLD.

Histo-pathologically, the estimation of fat in liver relies on visual assessment of the percentage of hepatocytes with visible fat droplets. There are five typical grading scale (0%, 1-5%, 6-33%, 34-66%, or >67%). However, less than 5% of fatty accumulation is not usually considered as a true pathologic abnormality [41]. Even though histology is considered the reference standard for the assessment of fatty lesion in liver, it has drawbacks; mostly including invasiveness, small sample size and observer-dependence which limits its usefulness in evaluating fatty fraction [42]. In addition, the distribution of fat droplets in the fatty liver lesion might be heterogeneous leading to insufficient information of the fat burden in the entire liver when using single biopsy from one location [43, 44]. For these reasons, histology with biopsy is a suboptimal modality and thus imaging has become to the forefront for the diagnosis of hepatic steatosis. MRI is a non-invasive imaging technique that can quantify fat accumulation for grading [45]. In- and out-phase (IP/OP) MR imaging developed by Dixon [46] is an attractive modality, and the most common MR imaging method to estimate and evaluate hepatic fat accumulation. This method is highly sensitive to signal differences between fat and water; and has become a superior and new reference standard in quantifying fat fraction (FF), when compared with non-invasive methods [47]. This technique will be discussed later in this chapter in section 1.5 on magnetic resonance imaging of hepatocarcinogenesis.

1.4 Animal models of hepatocarcinogenesis

Most human patients are diagnosed with malignant lesions which are irreversible with poor prognosis [48]. Given that carcinogenesis has multiple steps starting with benign (initiation) to precancerous (promotion) and finally to malignant lesion (progression), there is a strong mandate for using experimental hepatocarcinogenesis models including mice and rats to give a deep insight into the pathological characteristics during liver cancer development under controlled conditions [49]. Preclinical experimental animal models of HCC enables longitudinal studies that include monitoring of the tumour growth as well as drug uptake and response to treatment. In addition, preclinical experiments enable correlation of histopathological results at various time points with imaging and serum biomarkers, which cannot be performed in HCC patients [50].

HCC is preceded in both humans and animals by the development of precancerous lesions including DNs, which exhibit a higher risk for HCC development [51, 52]. Similar to in humans, the cytological criteria of DN in rodents such as nuclear to cytoplasmic changes, nuclear crowding, and hyperchromasia are commonly seen suggesting that DN is the intermediate step to early HCC [49, 53]. Rat models of HCC are commonly used because they share features with human carcinomas at different time points [54]. For example, eosinophilia and basophilic alterations in rats are the counterparts of DN in humans [49, 55]. This introduction highlights the most currently used animal models for HCC with emphasis on chemical carcinogenesis induced by diethylnitrosamine, diet-induced carcinogenesis (choline deficient amino acid diet), and genetically modified models (Table 1-1). These models of HCC were chosen based on their usual MR imaging features of tumorigenesis that are observed in human HCC. This sequence includes fibrosis, cirrhosis, fatty lesion, angiogenesis, precancerous nodules, and finally HCC.

Table 1-1. The common MR experimental models for HCC

Model	Liver Disease before HCC incidence	HCC development	References
Diethylnitrosamine (DEN)	- 10 mg/kg of body weight of DEN dose induce fibrosis	- Varies based on species, dose, and way of administration. For example, DEN injection to mice model usually induces a multiple HCC nodules within 40 weeks	[5] [56]
Choline-deficient, L-amino acid (CDAA) diet	- Fatty lesion by 1 week - Regeneration after 2 weeks - fibrosis by 12 weeks - cirrhosis by 30 weeks	- 100% incidence by 52 weeks	[57]
C-myc transgenic mice	-	- 40% incidence by 45 weeks - 80% incidence by 65 weeks	[58]

1.4.1 Chemical carcinogenesis induced by Diethylnitosamine

Diethylnitrosamine (DEN) is the most frequently used chemical carcinogen, which has the potential to cause malignant lesion, specifically HCC [59, 60]. Diethylnitrosamine can be found in water, tobacco smoke, pharmaceutical agents, agricultural chemicals, cosmetics, and fried meals [61]. DEN occurs under the genotoxic chemical carcinogens category, causing cancer by forming DNA adducts, and defined as DNA reactive due to the reaction of multiple enzymes of P450 including cytochrome (Cy) p2E1 [62]. This reaction leads to DNA damages and genetic changes of the target cell and in consequence tumours. DEN-induced carcinogenesis has been tested in animal species including mice and rats and showed hepatic cellular alterations similar to those found in human tissues [63] which eventually lead to multifocal HCC in the background of varying degrees of cirrhosis [64]. Laboratory analyses revealed that most juvenile mouse strains reflects human HCC associated with poor prognosis [65]. The liver pathology is dependent on the dose of DEN. For example, liver fibrosis will be induced at dose 10 mg/kg of body weight [66]; however, at doses above 25–30 mg/kg, it induces stages of multistep hepatocarcinogenesis starting from precancerous nodules through to the development of HCC [67]. DEN injection in mice usually induces multiple HCC nodules within 40 weeks, which provides gene expression profiles similar to those found in in human HCC [65, 68]. A study in the DEN-rat model showed that the development of fibrosis and HCC were seen after 12 weeks and 16 weeks, respectively, from receiving DEN intraperitoneally (50 mg/kg body weight). Thus, the induction of HCC varies based on species, dose, and method of administration. DENs can be administered to animals by inhaled gas, oral gavage, intraperitoneal injection, or in drinking water [5]. DEN is typically injected intraperitoneally in mice between 12 and 15 days of age [60]. A single dose of DEN administration intraperitoneally is the simplest and most effective way to reduce the time of HCC development [69]. For example, mice at the age of 14 days injected by a single dose of DEN will form multi-neoplastic nodules in the liver within 40 to 50 weeks in 80 to 100% of the animal [56]. Another study showed that HCC developed in B6C3F1 mice 44 weeks from DEN-intraperitoneal injection [60]. Administering the DEN to older mice (e.g. 4 weeks of age) is less efficient in inducing HCCs, compared to the previously mentioned, and thus it less frequently used [70].

Morphologically, DEN induces variable numbers of tumours, generally up to 10 multifocal lesions per rat with different sizes ranging from millimetre to centimetre. A full range of angiogenesis can be evident from hypo- to hyper- or avascular tumours. Various carcinogenesis pathways including benign dysplastic to early HCC and a range of grades of HCC can develop. This closely resembles human hepatocarcinogenesis [71].

1.4.2 Diet-induced carcinogenesis (choline deficient amino acid diet)

Dietary choline is required for some mammals including human and rats. Choline is a key component of phosphatidylcholine and sphingomyelin (phospholipid classes) that are required for all cell membranes. It is also important for the synthesis of the neurotransmitter acetylcholine as well as a methyl group donor in methionine metabolism [72, 73]. Choline deficiency is the only nutrient diet that causes cancer in the absence of any additional known carcinogen [74]. Choline deficient diet (CDD) has been developed in mice and rats to induce steatosis, fibrosis and cirrhosis [75, 76].

Methionine is an amino acid and considered as a good source for synthesising the methyl groups of choline. The low intake of methionine is required for choline deficient diet preparation [77]. Choline deficient rats on a low methionine diet develop HCC in the absence of any other carcinogens. There are several mechanisms that occur in rat livers during this diet including fatty infiltration, cell necrosis and death, increase in cell proliferation, cirrhosis, and finally HCC [77]. Choline deficient amino acid (CDAA) diet given for 3 to 12 weeks, induces cirrhosis and HCC in mice and rats [52]. Nakae *et al.* reported the progression to hepatocarcinogenesis of Fisher rats fed by CDAA. Histologically, regeneration with hepatocyte death are seen after two weeks and oval cell proliferation was observed after 4 weeks. Fibrosis and cirrhotic multiple nodules were observed by week 12. By 30 weeks, cirrhosis was developed. Around 30 weeks, HCC begins to develop and reaches 100% incidence by 52 weeks [57]. Male rats are more sensitive to choline deficiency than female rats [78].

1.4.3 Genetic-modified mouse HCC

Genetic methods can be used to induce tumorigenesis in liver and show similar molecular features of HCC [79]. There are two types of transgenic mice: conditional and constitutive expressions. In conditional expression, only liver express the genetic alteration; while in constitutive expression, the alteration is in all organs [80]. The C-myc transgenic mouse (conditional expression) is the most established and well characterized transgenic model of hepatocarcinogenesis [58]. Myc acts as a transcription factor that controls expression of genes which are important in the normal cell cycle including differentiation processes [81]. C-*myc*, L-*myc*, and N-*myc* are genes belonging to the myc gene family which have neoplastic potential. When these three genes are overexpressed and aberrant, the development of tumours follow [82]. Liver tumours can be induced in c-myc transgenic mice by selecting the c-myc expression of the liver directed by the alpha 1-antitrypsin promoter or the albumin enhancer (alb)/promoter [83, 84]. The HCC lesion incidence in these c-myc transgenic mice is relatively slow and corresponds to the development of HCC in humans associated with better survival [58, 85]. The HCC incidence of alb-myc^{tg} mice are less than 40% in 45 weeks, while they can be seen by week 65 in 80% of animals with a minimum of one HCC nodule [58].

1.5 Magnetic resonance imaging for hepatocarcinogenesis

The MR imaging protocols for evaluating pathologic changes during hepatocarcinogensis include: anatomical imaging including fast spin echo T_2 (FSE) and T_1-weighted gradient-recalled echo (GRE) in-phase and opposed-phase (Dixon method, IP/OP) sequences; contrast agent enhancement imaging using T_1 weighted images before and after a bolus injection [86]; and advanced sequences such as spectroscopy and diffusion weighted imaging.

1.5.1 Anatomical imaging

1.5.1.1 Dixon method and T_2 weighted imaging

In-phase/Out-phase (IP/OP) imaging utilizes T_1-weighted dual gradient echoes to control the phase of fat proton signal relative to water protons. The relative phase of the water and fat signals can be selected by varying the echo time (TE) according to the chemical shift difference of 3.5 ppm between water and the methylene peak ($-CH_2-$) of fat. Two images are acquired, one in-phase (IP) and one out-phase (OP). Since two images are acquired, it is called a "two-point Dixon method". Addition of the IP and OP images gives signal intensity in the liver proportional to the water content since the fat signal is canceled. Subtraction of the IP and OP images cancels water signal resulting in liver signal intensity relative to the fat content. To achieve maximum contrast of lipid, the TE should be optimised to acquire IP and OP images, and other MR parameters kept consistent.

IP/OP imaging can contribute to the diagnosis of fatty lesions in the liver and help characterize liver tumors [87]. Microscopic lipid accumulation during HCC development results in a signal drop due to water-fat signal cancelation in the out-phase image [88]. An illustrative case of IP/OP showing HCC with fatty content is provided in figure 1-3. Hyperintensity in early HCC may appear due to the presence of copper, glycogen, protein [89], or related to the degree of histological differentiation [90]. Distinguishing between DNs and early HCC based on T_1 images alone is difficult since both lesions may appear as hyperintense [91, 92].

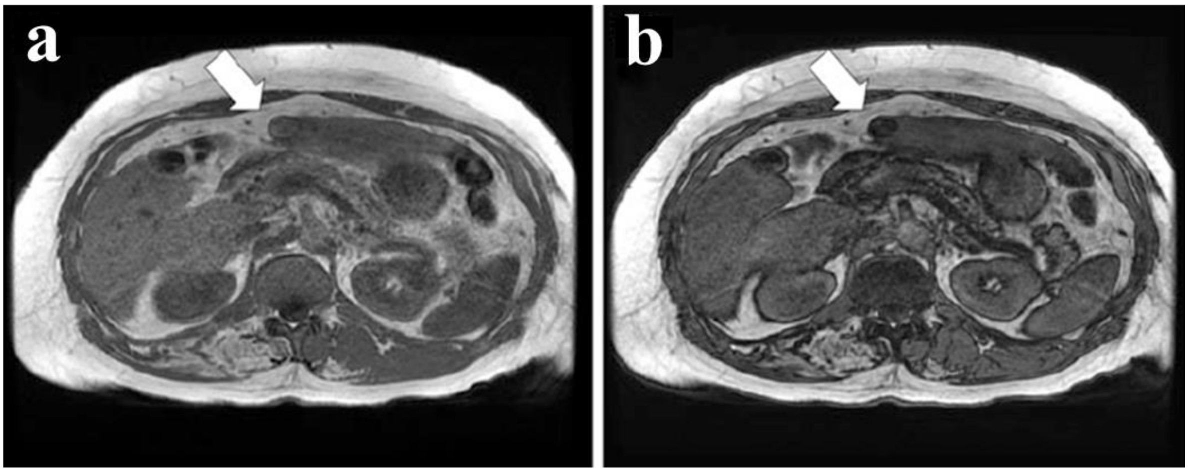

Figure 1-3: Axial IP (a) and OP (b) MRI images of patient showing focal HCC with fat content (arrows). IP shows HCC slightly iso-intense signal compared to the surrounding liver parenchyma (arrows). OP shows signal loss in HCC, indicating HCC with fat content [93]

Variable accumulation of fat in the surrounding hepatocytes also complicates the use of IP/OP for detection of early HCC. Accurate quantitative biomarkers of fatty lesions in liver may contribute to grading, prognosis, and treatment decisions. Qualitative diagnostic methods are insufficient for accurate detection, increasing the need to use a quantitative threshold to estimate fat percentage relative to a pathologic threshold [94, 95].

1.5.1.2 T_2 weighted imaging

T_2 weighted images can distinguish most early HCCs as hypointense [92, 96] becoming hyperintense with increasing degree of histological differentiation [90, 97, 98]. Signal intensity in T_2 images increases with the grade of malignancy and appear more hyperintense in advanced HCC [99]. DNs are rarely if ever hyperintense on T_2 images [100]. Infarction may associate with DNs leading to hyperintensity signal on T_2 images and can be mistaken for HCC [101]. The classical MR appearance of a central HCC within a DN “a nodule within a nodule” on T_2-weighted images is high signal intensity within a hypo-signal intensity nodule [102].

Detection of early HCC remains challenging using T_2 weighted imaging. It is variable in signal intensity and HCC is difficult to distinguish from premalignant DN. A preclinical study in the DEN-rat model of HCC performed on 1.5T scanner reported that HCC lesions had variable signal appearance compared to normal parenchyma tissues on T_2 images: smaller HCCs were iso- to slightly hyperintense, whereas larger HCC (1-1.6 cm in diameter) were observed as mosaic signal intensity patterns [103]. Another study in transgenic mice showed that among 67 histologically confirmed HCC lesions, 62 were detected by MRI. Among these 62 HCCs, 52 (83.9%) were hyperintense signal on T_1 images, while 10 (16.1%) were isointense. 46 tumours (74.2%) were hyperintense signal on T_2 images compared to hepatic parenchyma background and 16 were isointense. [104]. A preclinical study by Schmid *et al.* in DEN-treated mice indicated that liver tumours became detectable by T_2-weighted 3D imaging when they exceeded approximately 1 mm in diameter and showed signal hyperintensity (figure 1-4). However, tumors less than 1 mm in diameter were difficult to observe by the MR protocol [105].

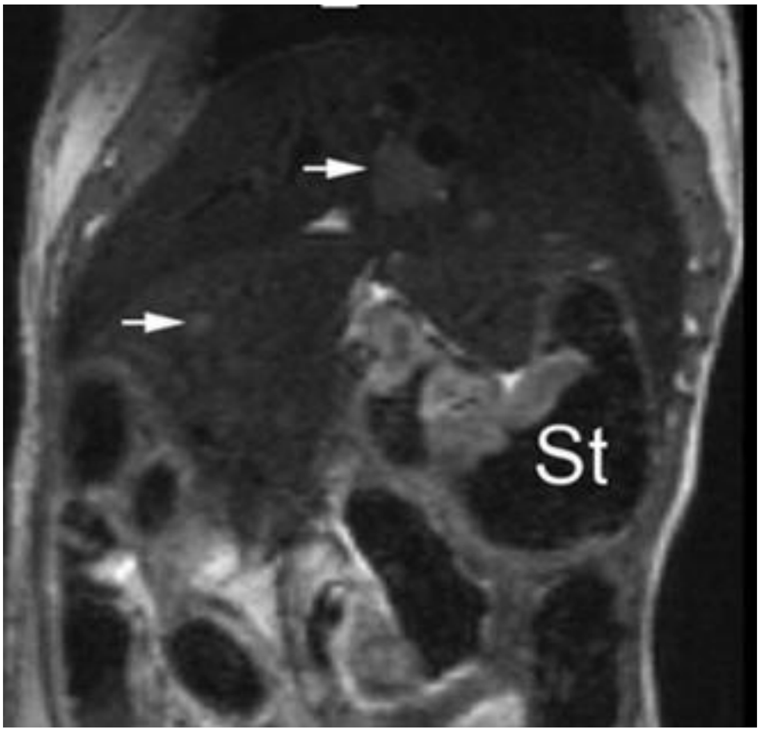

Figure 1-4: A representative 3D T_2 image of hepatic tumour in a mouse model after DEN treatment. Tumours (arrows) were shown as hyperintense signal with a minimum size of ~ 1 mm (St: stomach) [105].

1.5.2 Contrast Agent Enhancement

1.5.2.1 Vascular Agents

Gadolinium contrast agents are commonly used as vascular contrast agent that shorten T_1 relaxation time and provides information about vascularity of hepatic nodules [106]. Gadobenate dimeglumine (Gd-BOPTA) is classified as a vascular agent, mostly used clinically for dynamic contrast enhanced imaging. This contrast agent is more useful in the progressed HCC rather than the early stage HCC due to the predominant vascular supply to HCCs from unpaired hepatic arteries and the absence of the portal vein supply.

Repeated acquisition of 3D T_1-weighted gradient echo images after a bolus injection of contrast media enables assessment of the arterial-phase, portal-phase, and the equilibrium phase of signal intensity changes. The different phases of gadolinium contrast enhancement can be used as a characteristic feature in the diagnosis of hepatocarcinogenesis [23, 107]. Arterial enhancement phase and washout in the 2 late phases (high signal appearance) is regarded as a characteristic feature of HCC [108].

1.5.2.2 Hepatocellular Agents

Recently, gadoxetate acid (gadolinium ethoxybenzyl diethylene-triamine pentaacetic acid, Gd-EOB-DTPA) has become available for evaluating HCC. Gd-EOB-DTPA works as a liver-specific contrast agent allowing for both dynamic imaging and hepatobiliary phase imaging [109]. Gd-EOB-DTPA is taken up by hepatocytes and undergoes hepatobiliary excretion. The hepatobiliary phase can be acquired 20 minutes after intravenous injection in addition to the 3 early uptake phase images [110]. Consequently, dysfunctional hepatocytes in the hepatocyte-specific phase will show hypointense signal compared to hyperintense background liver and thus improves the diagnosis for liver-HCC [111, 112]. Frericks *et al.* reported a significant improvement in the HCC diagnostic performance, from 69.8% to 80%, by adding hepatobiliary phase imaging [113]. Another study showed an improvement in detection and characterization of small HCC ($\leq$1 cm in diameter) in the cirrhotic liver between dynamic phase and hepatobiliary phase imaging (85.3% versus 96.0%) [114].

The hepatobiliary phase imaging for differentiating between early HCC and DN is quite challenging. This is because the small early HCCs are often hypovascular and may mimic the DN appearance. In human beings, Kogita *et al.* reported that some DNs were hypointense and some early HCCs were isointense in the hepatobiliary phase [115]. Another study showed that approximately 70% of DNs and 97% early HCCs were hypointense on hepatobiliary phase images [116]. In animals, a study of 20 c-myc/TGFa transgenic mice with HCC showed that 12 out of 20 HCC nodules were seen as hyperintense and the other 8 appeared as hypointense compared to the liver parenchyma background [117].

1.5.2.3 Iron oxide agents

Superparamagnetic iron oxide (SPIO) agents have been investigated for detection of cirrhosis-associated HCC. SPIO particles target the Kupffer cells of the reticuloendothelial system. They increase the local field inhomogeneities leading to a decrease in the signal intensity of liver tissue on T_2 and T_2* weighted images [118]. The degree of uptake of SPIO relies on the functionality of Kupffer cells, which are rarely seen in HCCs. Thus, the detection of HCCs is improved due to little or no uptake of SPIO, whereas DN shows a significant loss of signal due to the significant uptake of SPIO [99, 119]. Guo *et al.* used both SPIO and gadolinium to differentiate HCCs from benign nodules in a rat model induced by DEN in the presence of cirrhosis. Among 82 HCC nodules, gadolinium arterial phase imaging detected 73 nodules as hyperintense enhancing nodules. Combining SPIO with gadolinium increased the detection up to 79 nodules. An additional 6 HCC nodules detected were isointense in all three dynamic phases in gadolinium-enhanced imaging with moderate hyperintensity in SPIO-enhanced imaging [120]. However, some hypervascular early HCCs, have been reported to accumulate SPIO, while other hypovascular HCC lesion may have reduced uptake. Therefore, diagnosis of early HCC with SPIO still remains a challenging issue [117].

1.5.3 Relaxation times

Contrast in MR images is based primarily on the contribution of water proton T_2 and T_1 relaxation times in various tissues within biological systems. In addition, these relaxation times can be exploited to provide useful quantitative assessment of pathology and help differentiate between normal and abnormal tissues [121]. Relaxation times have been used to evaluate rodents with infarction [122] and tumour malignancy [123]. To the best of our knowledge, most of the MR studies for malignant liver diagnosis using relaxation times were performed on liver metastasis [124] . However, even in liver metastasis, there have been limited studies.

Transverse relaxation is a reduction in the magnitude of net transverse magnetization due to spin-spin interactions (loss of phase coherence) and has a time constant, T_2. Immediately after the application of a selective RF pulse, the transverse magnetization is in phase resulting in maximum transverse magnitude. The magnitude will then decrease as spins precess out of phase. The characteristic time representing the decay of the signal is called the T_2 relaxation time [125]. T_2 is a key source of MRI contrast representing changes in molecular mobility, commonly interpreted in terms of tissue water or lipid distribution changes.

T_2 relaxation times have been used to assess tumours of experimental animal models [126]. It has been reported that superior differentiation between benign and malignant liver lesions is possible using T_2 relaxation data compared to visual signal intensity assessment [127]. In liver tumour with metastasis, higher T_2 relaxation times were reported compared to normal liver [124]. For HCC, the values of T_2 relaxation time calculated using 2 echo times (TE) were used to differentiate non-solid (such as haemangioma and abscesses) from solid liver (such as, focal hyperplasia, metastases and HCC) lesions [128]. Both malignant and benign solid lesions showed similar T_2 values. This result was in agreement with a preclinical study in DEN-rat model of which showed that the mean T_2 value of cysts was significantly higher than those of DN and HCC. However, there was no significant difference in T_2 values between DN and HCC. In general, T_2 information is not frequently used in the clinical setting [124].

Longitudinal relaxation is the process whereby the net magnetisation is re-established along the direction of the B_0 field following the application of an RF pulse. The exponential recovery has a rate constant known as the relaxation time, T_1. Limited studies have been reported investigating T_1 relaxation times in malignant liver. These studies have been performed mostly in metastases in the liver, and increased T_1 with tumour growth has been demonstrated [129]. Clinically, the use of T_1 relaxation times to differentiate and characterize liver malignancy has been less useful and not reliable for liver characterization. An early study by Goldberg *et al* showed that T_1 values cannot be used to discriminate between fluid–filled lesions and solid lesions (e.g. HCC) [130]. Another clinical study showed no difference between T_1 values for cysts and HCC. It reported that the mean T_1 values for cysts and malignant lesion were 691 ± 215 ms and was 609 ± 133, respectively [131].

1.5.4 Diffusion Weighted Imaging

Diffusion refers to the random microscopic motion of molecules owing to the thermal energy they carry (Brownian motion). Conventional MRI (e.g. T_2 weighted imaging) is well known for its ability to display deep and superficial tissue with high contrast and resolution. Conventional MRI sequences tend to minimise the contribution of diffusion to the image contrast and MR parameters such as T_2 or T_1. [132]. Diffusion weighed imaging (DWI) targets the effect of micro-molecular motion on the final echo signal [133]. It offers contrast enhancement between areas with high and low diffusion rates on MR images by inserting strong diffusion gradients into MR sequences leading to higher sensitivity to microscopic motion [134] and therefore, to tissue structure. Diffusion weighted imaging (DWI) has diagnostic potential because it allows investigation of tissue microstructural changes, quantified as the apparent diffusion coefficient (ADC). The ADC is obtained by acquiring images with multiple diffusion gradient strengths (*b* values) which decreases signal intensity relative to the diffusion rates of water molecules [135].

Cellular density and membrane permeability changes modify the diffusion characteristics of tissue water. This may result from pathologic processes following regeneration or obliteration of cell membranes or as a consequence of inflammation or neoplastic lesion formation. These aspects affect the extent and directionality of proton diffusivity which can be imaged and quantified by DWI [136, 137] and thus adds microscopic information to the structural information provided by conventional MR sequences [138]. In tumours, the cell density increases leading to a decrease in the extracellular space which is characterised by decreased mobility and restricted diffusion [139].

Early human studies have shown potential for ADC quantification to add information to MR protocols for differentiating fluid-filled lesions, such as cysts and haemangioma, from solid lesions such as HCC [140, 141]. For example, Kim *et al*. reported that neoplastic tumours have a significant lower ADC than benign nodules such as cyst and haemangioma, thus ADC has good potential for characterizing liver tumor [142]. This is in agreement with an animal study in a DEN-rat model of hepatocarcinogensis where the mean ADC of cysts was significantly higher than that found in early HCCs [103].

The pathway from DN to early HCC has some degree of increased nucleo-cytoplasmic ratio and cell density which is difficult to distinguish histologically [143]. The ADC in early HCCs is not significantly different to solid benign tumour, despite a slight increased cellularity [144]. Xu *et al*. also reported no significant difference in ADC value for the DEN-rat model in early HCC compared to DN; suggesting that the ADC alone may not be sufficient for tumour characterization [145]. This corresponds with another study with another DEN-rat model of HCC: an overlap of ADC between DN and HCC was observed [103]. In a patient study, the mean ADC of HCC was significantly lower than DN in the cirrhotic liver group [146]. However, there was no histological characterization of HCC grades in these patients.

The ADC values show large variation within each of the different HCC grades (well, moderately, and poorly differentiated HCCs). For example, studies have reported that early HCCs have higher ADC values than that of more aggressive grades [147, 148]. Others have shown the ADCs in early HCC is slightly lower than those in moderated HCC [149]. The variation of the ADC may be explained by biologic variations and/or errors in the measurements of ADCs. Some studies have reported that ADC was not related to cell density [150, 151]. A preclinical study of chemically induced experimental HCCs in rat liver showed that moderated and progressed HCC have higher ADC values than in early HCC [145]. This higher ADC can be explained by the presence of necrotic regions within these tumours which leads to loss of cell membranes and thus increases extracellular diffusion [152, 153].

An increase in the number and magnitude range of *b* values acquired increases the accuracy of the calculated ADC value. This may improve differentiation between benign and malignant liver lesions and reduce the T_2 shine through effect [154]. Applying small *b* values has been reported to improve the detection of focal lesion [142], while applying high *b* values will provide better characterization for tumours such as HCC [155]. However, the optimum higher *b* value has to be carefully selected to avoid loss of SNR [154]. The contribution of perfusion to the ADC measurement is larger when using small *b* values compared with high *b* values. This was demonstrated in a VX2 rabbit model of liver tumour reporting a decrease in calculated ADC as *b* values increased (0-100 s/mm^2 vs 0-1000 s/mm^2) [156] and in rat livers where the effect of perfusion on ADC measurement decreased with *b* values (0, 50, and 100 s/mm^2) compared to high *b* values (500, 750, and 1000 s/mm^2) [157].

In summary, ADC measurement is helpful in differentiating fluid-filled lesions from solid lesion such as DN and HCC. Given the wide variation of ADC among HCC grades, and the significant overlap distribution of ADC values between DN and HCC in both animal and human, ADC measurements are currently not a definitive marker for hepatocarcinogenesis characterization. Improved methods for determining the ADC value and a greater understanding of the biological variability in HCC progression, may improve the applicability of ADC in HCC diagnosis and grading.

1.5.4 MR spectroscopy

In vivo MRS is a non-invasive technique that provides physiological and chemical information rather than anatomy in the living tissue, and is used diagnostically in brain [14], breast [15], and prostate [16]. In hepatic diseases, fatty changes and steatosis in a lipid-induced rat model have been intensively examined by MRS with few studies in patients and proven to be successful [17]. It has been reported that in an animal model of HCC metabolite signals including saturated and unsaturated lipids as well as choline play important roles in the process of hepatocarcinogenesis [18, 19]. These metabolites are potential biomarkers for evaluating HCC and are observable by MRS. Signals obtained from saturated lipid include methyl protons (–CH3; 0.9 ppm) and methylene protons ((–CH2–)n; 1.3 ppm). Unsaturated lipid also contains diallylic protons (=C–CH2–C=; 2.8 ppm), and vinyl protons (–CH=CH–; 5.3 ppm). Choline has a characteristic N-CH3 resonance at 3.2 ppm.

The most dominant fat protons arise from methylene and methyl protons and are used in tumour spectroscopy as biomarker of membrane breakdown [29]. Choline containing compounds are a marker of cellular membrane turnover. Choline levels correspond to the degree of malignancy, cellular proliferations [19, 158, 159], and represents elevation of membrane phospholipid biosynthesis [160]. Therefore, elevation of the choline peak is used as marker for cellular proliferation during the progression of HCC.

Unfortunately, *in vivo* MR spectroscopy is not applied often in a clinical setting for evaluating liver due to technical challenges, long scan times, low signal to noise ratio, and the need for expertise in spectral interpretation.

Research using *in vivo* MRS has been carried out on experimental HCC animal models to demonstrate these metabolite changes and a correlation with HCC staging. Towner *et al.* used a DEN-rat HCC model to show alterations of lipid alterations from weeks 0 to week 24 after DEN induction. The methyl and methylene group increased from week 0 to week 6 compared with control rats and decreased by week 12. The vinyl hydrogens showed a gradual increase at week 12 peaking at week 18 and decreasing at week 24 [161]. Another study performed on the DEN-rat model HCC with different scan time-points showed that the methyl and methylene groups did not increase in the early stage (week 7 to 13) but they decreased in late stages. Choline was increased in the late group [19]. Xu *et al.* found that the choline to lipid ratio in DEN-rat model HCC increased significantly with the progression of HCC [162].

Conclusion

Currently there is not a single or a combination of MR techniques that definitively allow the detection and grading of HCC tumours. The goal is to be able to accurately grade HCC with non-invasively measured MR parameters. In addition, it is important to be able to assess precancerous lesions such as fatty lesions, cirrhosis, and DN. Further work is required to advance MR methods and build a better understanding of the relationship between MR parameters and liver pathology.

1.2 Thesis aims

The overall aim of this thesis is to improve MR methods used to assess liver pathology. In particular, for early detection of HCC and therefore providing an opportunity for early interventional treatment strategies to limit the development of end stage liver malignancy. The quantitative analysis MR protocol to be developed and assessed will include:

1) in-phase (IP) and out-phase (OP) Dixon MRI to estimate fat fraction (FF),

2) multi-slice-multi echo sequence (MSME) to obtain T_2 weighted imaging for T_2 relaxation measurements,

3) Diffusion weighted imaging to produce images for ADC measurements.

The imaging experiments will be conducted at 9.4 T in choline deficient amino acid modified (CDAA) diet induced liver cancer in the rat model to study the development of HCC *in vivo* with accurate diagnosis of HCC. We will investigate the potential of this quantitative information as imaging biomarkers of tumour development and grading. We hypothesize that quantitative multi-parametric MR parameters, T_2 relaxation times in combination with ADC values, as well as quantifying fat fraction (FF), will be powerful biomarkers of characterization and early detection of carcinogenesis in the liver.

Aims:

- Optimization of the MR protocol for in- and out-phase T_2-weighted imaging, and diffusion-weighted imaging sequences for *in vivo* CDAA-rat model of liver HCC imaging (chapter 3).
- Develop image analysis methods for liver segmentation and quantification of MR parameters including: mono and bi-exponential T_2 calculation and fat fraction. Apply these methods to obtain image maps of the calculated parameters (chapter 4).
- Apply and assess the performance of mono- and bi-exponential models in fatty liver disease (chapter 5)
- Investigate the correlation between FF and T_2 values during a sustained period of CDAA diet induced hepatocellular carcinogenesis to monitor the diffuse fatty liver and nodular lesion over time (Chapter 6).
- Compare *in vivo* MRI with MR *ex vivo* and histopathologic findings at final scan time point for conforming lesions purposes (chapter 6).

Approach:

There are numerous functions which have been applied to parameter estimation of T_2 decay data. These can be mono- and multi-exponential functions and some non-exponential functions. Each makes assumptions of some underlying biological function. We have chosen two model candidates for comparison including mono- and bi-exponential decay functions. In the mono-exponential decay function, it is implicitly assumed that within a pixel there exists only a single spin type contributing to relaxation and that T_2 is only modulated by tissue characteristics (or chemical environment). In other words, there is an assumption that within each pixel there is one dominant spin and thus one T_2 value. In fatty tissue, this is not true and thus inclusion of another spin-type logically leads to a double exponential function. For example, a T_2 bi-exponential fit model has been shown to distinguish between water and fat in living tissue [163]. In liver, Dixon's two-point MRI technique assumes that fatty lesion has two main components contributing to the total MR signal. These two components are derived from two signal sources; water and fat spins [46]. Moreover, fat-suppressed T_2-weighted imaging sequences are used in fatty liver disease to suppress fat signal, which decreases the overall liver signal in fatty liver, and then a comparison is made with T_2-weighted imaging without fat suppression. Signal loss indicates the presence of a significant fat component. Hence, a T_2 decay will exhibit a bi-exponential function yielding two T_2 decay times (short and long). Fat is known to have a longer average T_2 than liver water [164], suggesting that the long and short T_2 relaxation times originate from liver fat and water components, respectively.

Because our animal model is well known to induce early diffuse fatty liver, and later, heterogeneous nodules, we compared mono- and bi-exponentially calculated T_2 values for characterizing changes in T_2 relaxation times in healthy and CDAA rats during development of hepatocarcinogenesis over time and assessed their potential diagnostic capability.

Most studies model the T_2 signal decay by applying a mono-exponential model. It would be expected that T_2 would increase as the fat fraction increases, since the fat signal has a longer T_2 than liver water.

It has not been reported how mono- and bi-exponential components may change in diffuse fatty liver and nodular lesions. To characterize the T_2 parameters in our animal model, we proposed to assess the correlation between percent fat fraction (% FF) as measured by IP/OP imaging and ADC with transverse relaxation times determined from mono- and bi-exponential decay functions.

Chapter 2 : Method

The CDAA rat model was used to investigate progressive changes leading to HCC development. Figure 2-1 illustrates the general time line of the experiments that were performed in this work.

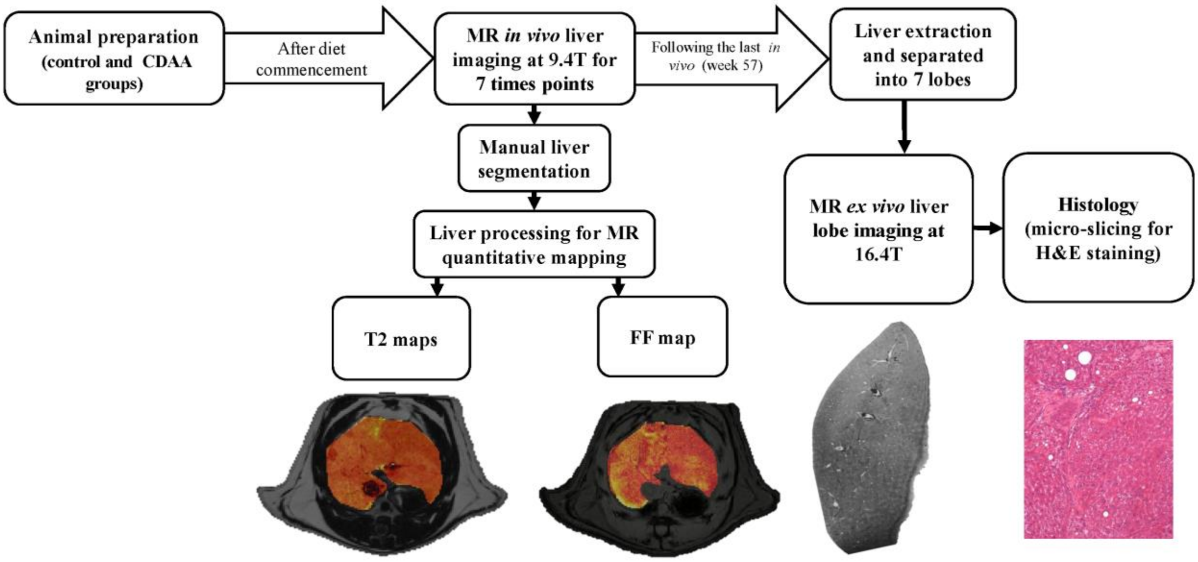

Figure 2-1: Animal preparation, *in/ex vivo* MR imaging, imaging processing, and the histology processing pipeline

In vivo quantitative MRI was performed at 12, 24, 32, 40, 48, 52, and 57 weeks at 9.4T scanner after CDAA administration. Following the *in vivo* MR experiments, rats were sacrificed and livers taken for *ex vivo* imaging at 16.4T and histologic evaluation. The overall schedule of the experiment is shown in figure 2-2.

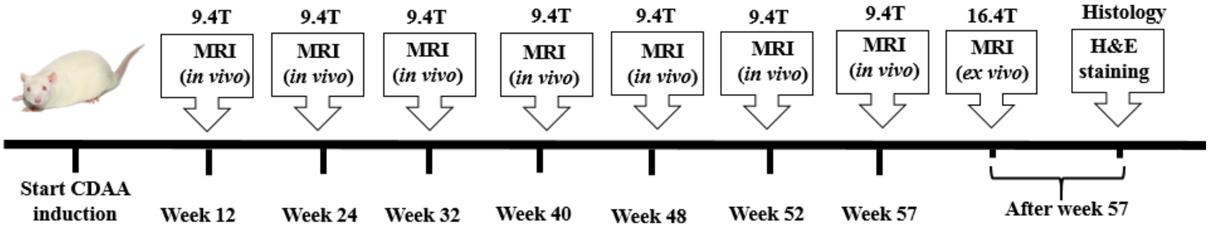

Figure 2-2: Schedule of CDAA and CSAA for in male Fisher rats for *in/ex-vivo* MRI and histology.

2.1 Animal model and experimental design

2.1.2 Animal model and Diet

Animal models of HCC have been successfully established for several purposes including evaluate malignant-host reactions, staging carcinogenesis process, understanding the pathophysiological mechanism, and examine therapeutic medication. However, not all animal are ideal for all these purpose. Therefore, investigators should be well-informed of what animal model should be selected and is it going to match their aims and final results? [165]. In our project, we found that the suitable and ideal animal model of HCC is CDAA-rat model for the following reasons:

- CDAA-rat model is affordable and easy to handle
- provides reliable experimental proof of multistep carcinogenesis; from diffuse fatty liver to HCC.
- the model mimics the human HCC behaviour
- time point stage for HCC development has been addressed in a histology paper.
- Fisher rats proved to be ideal for experimental MRI purposes

CDAA and CSAA (Choline sufficient l-amino acid) were obtained in pellet form (Diet SF13-103, Specialty Feeds, Glen Forrest, WA, Australia). The compositions of these diets are described previously [57]. The amount of choline in CDAA and CSAA diets were 6.5 mg/kg and 14.48 g/kg, respectively. CDAA diet was mixed with a small amount of peanut butter to increase appetite.

2.1.4 Numbers of experimental rats

To determine the minimum number of animals which can provide scientific validity of results we used the “resource equation” method [166]. This method is mostly appropriate for quantitative outcome studies. It is also used when there uncertainty about significant difference between groups from previously published studies [167]. Because our project is mainly concerned with MR imaging quantitative measurements and to our best of knowledge no similar studies have been published, the resource equation method is the most appropriate. The equation is:

$$\mathrm{E} = \text{Total number of animals} - \text{Total number of groups} \qquad (1)$$

Where E is the degree of freedom and should be approximately between 10 and 20. When the E is lower than 10 or higher than 20, the number of animals is either not enough or more than necessary, respectively. In our project, we have selected 12 animals divided into 2 groups (six in control and six in CDAA groups). In this case E is 10 and hence an acceptable statistical limit and adequate sample number while minimizing animal use.

Besides the resource equation, we also considered two analytic points of view for selecting the number and type of rats in our project. Firstly, repetitive measurement of the same rat at specific time points will allow a longitudinal observation of HCC in non-invasive MR without the need to sacrifice animals in cohorts at the specific time points for organ analysis. Repeating the MR scans repeatedly over time reduces the inter-animal variability and improves data comparability, thus reducing the number of required rats. Secondly, using high magnetic fields will increase the signal-to-noise ratio and thus improve visualisation of lesions and accuracy of measurements.

2.1.5 Animal preparation

Experiments were approved by the University of Queensland Animal Ethics committee. Eight-week old Fisher 344 rats (n = 6) were placed on a choline deficient L-amino acid modified diet (CDAA) diet and compared with 8 age and sex matched control rats placed on choline sufficient chow.

Both groups receive diet continuously to the end of the *in vivo* MR experiment (57 weeks). All rats were on water ad libitum. They were housed in cages in a room with controlled humidity, light and temperature; and kept on a 12:12-hour light/dark cycle. The rats were regularly monitored for any signs of discomfort or severe illness. Animal weights were recorded at each of the MR scan time points.

2.2 MRI equipment and techniques

2.2.1 In vivo MR imaging acquisition

During MRI examination, animals were anaesthetized with up to 3% isoflurane in a flow of 1.5 L/min medical grade oxygen. MRI experiments were conducted with a Bruker Biospec 9.4T/30cm MRI spectrometer. The gradient set used could produce fields of up to 14G/cm. An 86mm quadrature radio-frequency (RF) resonator tuned and matched for protons was used for all studies. Animals were placed head first in the prone position with the liver positioned at the magnet isocenter. Constant body temperature was maintained throughout the experiment using circulating warming water to keep the temperature at approximately 36^{o}. The temperature was monitored by a rectal probe connected to the physiological monitoring system (SA Instruments, CA, USA). The prone position was found to be optimal to reduce diaphragmatic motion artefacts. The liver region was located in the centre of the coil. A pneumatic pillow was placed on the rat's abdomen to monitor the respiratory rate. The respiration rate ranged from 40 to 60 beats per minute during MRI scans. Each rat was examined with a total experiment time of approximately 40 minutes. Briefly, scout images in the axial, sagittal and coronal planes were collected with a 120 mm field of view, TE/TR=6/100 ms, flip angle=30, and matrix size= 128*128. The subsequent MR protocols (Dixon method, T_2, and DWI) are addressed in chapter 3.

2.2.2 Ex vivo MR imaging

The animals were sacrificed immediately after the final *in vivo* imaging time point (week 57) and livers were excised and cut into 7 lobes. Livers were fixed in RCL2 fixative solution (3:5 v/v RCL2/Ethanol) [168] and stored at 4^0 C in a refrigerator prior to use. The RCL2 fixative liver lobes were used for MR *ex vivo* imaging and then histopathological examinations.

For *ex vivo* MR acquisition, the 7 lobes were placed separately in a 50 mm falcon tube and MR imaging was performed with a Bruker 700 WB Avance NMR spectrometer using a multi-echo gradient-recalled echo sequence (MGE). The scanner is equipped with a 16.4 T vertical magnet with a bore diameter of 89 mm and a 30-mm-diameter RF coil. Pulse sequence parameters were: TR/TE = 40/4.2ms, FOV = 55*27.5*27.5mm, matrix 512*256*256, NEX=8,

$FA=18^0$, and total imaging time was approximately 4 hours, yielding a spatial resolution of $107x107x107\ \mu m^3$.

2.3 Histology

Following *ex vivo* imaging, the tissues were embedded in paraffin wax. Sections (5 μm) were stained with haematoxylin and eosin (H&E) and examined by a veterinary pathologist. Histological lesions were classified according to Thoolen *et al*. [169]. Numerous pathologies were found with two common in all tissue analysed; microvesicular fatty change where hepatocytes were filled with numerous small lipid vacuoles and macrovesicular fatty change with hepatocytes containing a large single vacuole. These photomicrographs were further compared with the corresponding MR images at the end of the study.

Chapter 3 MR sequence optimization

3.1 Optimization of IP/OP imaging

3.1.1 Fast low angle shot sequence for IP/OP acquisition

A Fast Low Angle Shot (FLASH) sequence was used to generate IP/OP images. This sequence allows shorter repetition times (TR) and therefore faster scan times are possible. A rewind phase encoding gradient used to eliminate steady state transverse magnetization before the next RF excitation [170].

3.1.2 Phantom and pre-cohort animal for IP/OP validation at 9.4T

To quantify the optimal echo times (TE) for IP/OP in the FLASH sequence, a margarine phantom (mixture of fat and water) contained in a 5.0ml vial was used. Margarine was chosen to mimic the overlap of water and fat signal in fatty liver tissue. This methodology was applied in an established pre-cohort fatty liver rat and compared to the margarine results to test whether IP/OP imaging is a robustly quantitative method for liver fat quantification.

3.1.3 TE optimization for IP/OP at 9.4T

The difference between resonances (Δf, Hz) at any magnetic field can be given by:

$$\Delta f = \bar{\gamma} B_0 \cdot \Delta\delta \qquad (2)$$

$\bar{\gamma}$ is the gyromagetic ratio (42.6MHz/T for ^{1}H), B_0 is the applied magnetic field in Tesla (T) and $\Delta\delta$ is the difference in chemical shift between water and lipid resonances in ppm, typically 4.8 and 1.3 ppm respectively.

The periods or TEs at which the spins return to in-phase is given by,

$$\text{Period (TE)} = 1/\,\Delta f \qquad (3)$$

Therefore, water and lipid spins are in-phase initially, neglecting any spin-spin dispersion during the pulse, and out-phase at half of this period.

From equation 3, the signals at 9.4 T will be out-phase at 0.357 ms (half of 0.714ms) and back in-phase at TE=0.714 ms. If the selected TE is 0.357 plus 0.714 ms (and further multiples thereof), lipid and water within the same pixel will be out-phase, destructively interfere and so a hypo-intense signal will be observed.

The details of the IP/OP parameters used for the phantom are summarised in Table 3-1.

Table 3-1. MR IP/OP parameters for phantom

Sequences	**TR** (ms)	**TE** (ms)	**NEX**	**Matrix**	**Slice thickness**	**FOV (cm)**	**Other specific parameters**
FLASH IP	250	2.856, 3.57, 4.284, and 4.998	2	256×256	1.5	8×8	Flip angle=45^0
FLASH OP	250	3.213,3.927 and 4.640	2	256×256	1.5	8×8	Flip angle=45^0

After the phantom test was completed, the IP/OP parameters were also applied in a pre-established rat model of liver fat lesion with only two echo times (IP= 2.856, OP= 4.641 ms). The FLASH sequence diagram and MR parameters to obtain Dixon images in animal at 9.4T scanner is shown in figure 3-1.

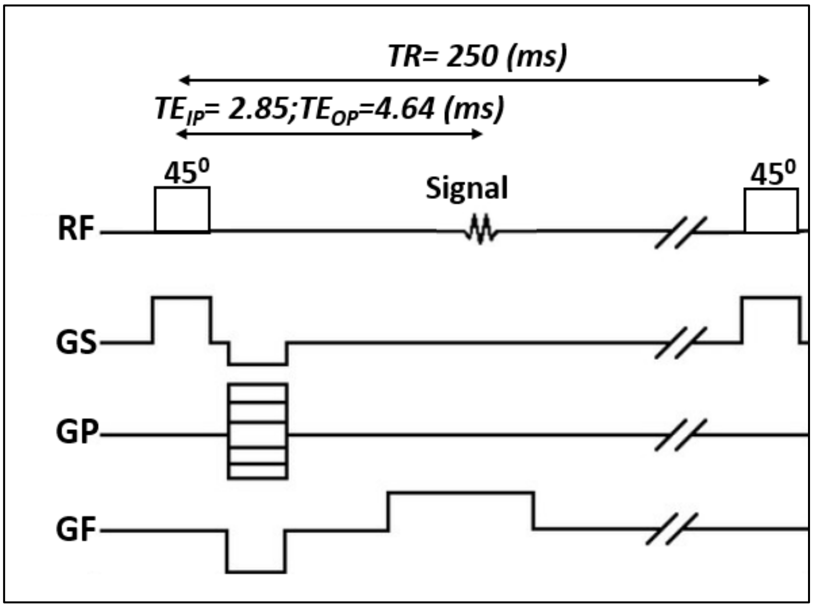

Figure 3-1: FLASH pulse sequence diagram with a variable TEs (IP= 2.85ms and OP=4.64ms), TR (250ms), RF (radiofrequency pulse), and the gradients (GS: slice gradient, GP: phase gradient, and GF: frequency gradient)

3.1.4 IP/OP optimisation results

The results of the phantom experiment with four IP and three OP TEs are presented in figure 3-2. Oscillation of signal intensity demonstrates the chemical shift difference between the fat and water protons during in- and out-phase cycle.

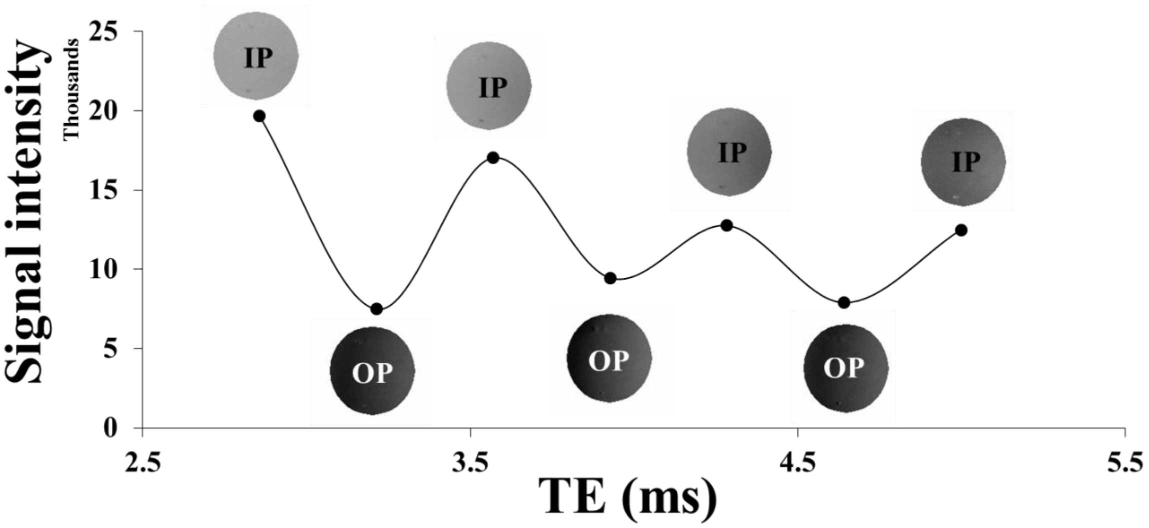

Figure 3-2: A periodic oscillation of signal intensity between IP and OP echo times resulting in overlap and void signal intensity of axial margarine phantom, respectively. IP TEs show hyperintensity signal (upper); while signal cancelation in out-phase images (lower) at OP TEs.

Figure 3-3 shows the fatty lesion with a homogeneous signal intensity in the liver area on IP images (TE= 2.856 ms) and signal cancelation on OP images (TE= 4.640 ms) compared with surrounding parenchyma. These two echo times ($TE_{IP/OP}$ = 2.856/4.640 ms) were used for IP/OP imaging *in vivo*. The choice of other imaging parameters in Table 3-1 was a balance between scan time, resolution, and signal to noise ratio (SNR).

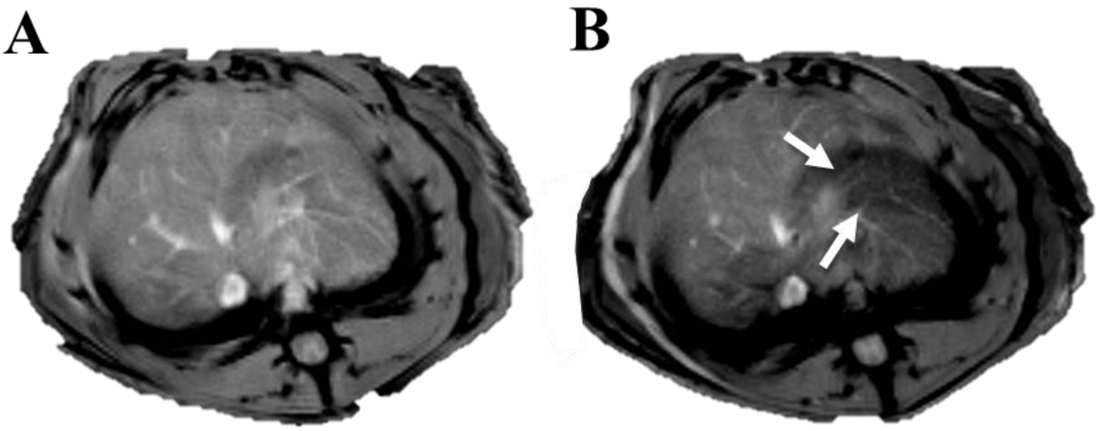

Figure 3-3: Axial images of a Fisher rat liver with fatty changes. A, signal of hepatic parenchyma is homogeneous on axial in-phase FLASH image (TE= 2.856 ms). The signal cancellation effect in pixels that contain both water and fat (B, arrows) was clearly apparent on the OP image (TE= 4.640 ms).

3.1.5 Discussion of Dixon method optimization

Protons of water and fat in living tissue have different Larmor frequencies (different chemical shifts) due to their different electron shielding [171]. In our project, we used a Dixon gradient-echo (GRE) sequence that relies on this chemical shift difference between water and fat to generate two images; in-phase (IP) and out-phase (OP) images. This is accomplished by acquiring two different suitable echo times (TEs) [46].

The efficacy of in-/out-phase parameters for overlap and signal void between fat and water was tested at 9.4 T by comparing the results of our phantom with animals. A good correspondence between theory and experiment using margarine phantom was demonstrated, and our preliminary results in rat liver *in vivo* also showed excellent results in areas involving fatty changes seen in the liver. The signal cancellation effect in pixels that contain fat and water was clearly apparent on the OP image in both phantom and animals.

For IP/OP phantom set up, the TEs chosen for IP and OP, 2.856 ms and 4.640 ms, respectively, were tested on the phantom using the FLASH sequence. These TEs were calculated from the chemical shift difference of 1401 Hz (determined from equation 3) at 9.4T between lipid and water. These TEs also produced good images for IP/OP imaging of the rat liver. IP images alone often miss detection of liver lesions due to the amount of intracellular fat

[172]. OP images are more helpful in detecting lesions that contain around 50% or less lipid than the surrounding liver tissue [171].

3.2 T_2 weighted imaging

3.2.1 Multi-slice multi-echo sequence for T_2 acquisition

Accurate estimation of T_2 values requires acquisition of multiple images acquired with a series of TE times. The T_2 weighted images were obtained using a multi-slice multi-echo sequence (MSME). MSME is made up of a series of selective 90° RF pulse – 180° refocusing pulses to generate echoes with different TEs and same phase encoding step (figure 3-4). This series is repeated at each repetition time (TR) interval with incremented phase encoding gradient (GP) to fill one line of k-space for each TE image during one TR. and, thus, images with consecutive T_2 weighting are obtained from which the T_2 value for each pixel or ROI can be determined. A phase rewind gradient is applied before the next selective RF pulse to obtain a coherent superposition of signals. This sequence generates T_2-weighted images for T_2 calculation and T_2 maps.

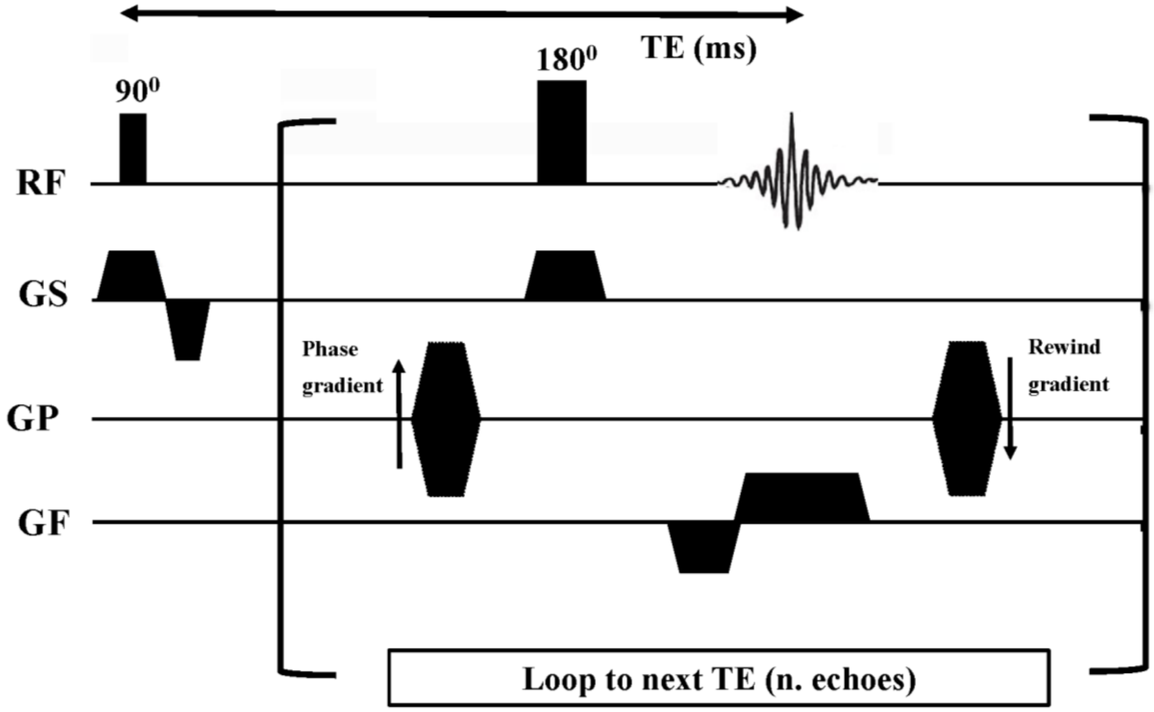

Figure 3-4: Schematic of multi-slice multi-echo (MSME) pulse sequence for acquiring

multiple T_2 images. In this sequence a slice is excited once followed by a 180° refocusing pulses. With the same phase encoding step (GP), multiple echoes can be recorded by applying subsequent 180 degree pulses.

3.2.2 Phantom and pre-cohort animal for T_2 validation at 9.4T

A phantom containing pure water was used to investigate the effect of the number of echo times (TEs) acquired using the MSME sequence at 9.4 T for T_2 data fitting. The sequence was then tested in control and pre-cohort fatty liver rat (same animals used for IP/OP optimization) for validation and set up the mono- and bi-exponential analysis methodology.

3.2.3 T_2 echo time and other parameter selection

The goal of designing echo times (TEs) for T_2 mapping is to find a set of TEs that has sufficient range to cover possible T_2 values in liver and minimize the total scan time. The TEs were selected based on the expected range of our pre-clinical T_2 values of control animals, such that T_2 values can be reliably estimated. The first echo time was chosen to be as small as possible (5 ms) and the last was as long as reasonable to allow for sufficient decay of liver signal, whilst avoiding the expense of extended imaging time and motion degradation. TE times were initially selected based on the observed decay curves of a control animal. By TE= 50 ms, about 85 % of the signal had decayed and this was selected as the maximum echo time. In the initial time points acquired with rat with fatty liver, we re-evaluated echo times based on observed decay curves of the fatty liver animals. Due to excess diffuse fat content, substantial signal remained at 50 ms (about 40 %), so echo times were extended to 130 ms, at which time (about 23%) of signal remained (figure 3-5).

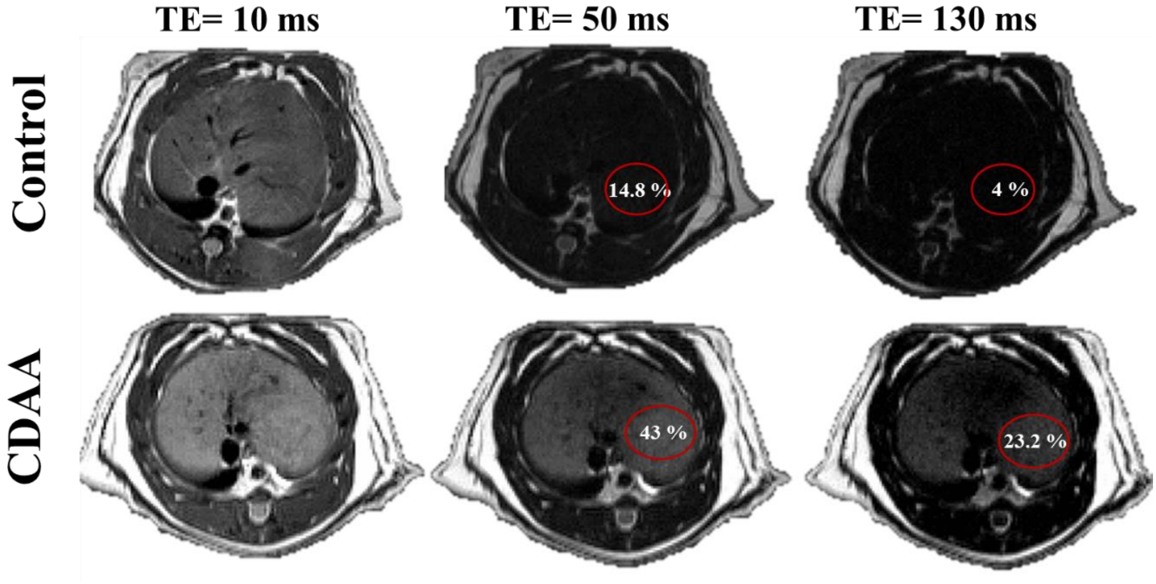

Figure 3-5: Axial T_2 images of control and CDAA rat livers show a reduction in signal intensity with increasing echo times (10, 50, and 130 ms; respectively). The percentage of signal intensity remained in the ROIs (red circles) at 50 and 130 ms of control liver compared to 10ms were 14.8% and 4%, respectively; while, 43% and 23.2 in CDAA liver rat.

Therefore, 13 echoes were collected and spaced uniformly every 5 ms from 5 to 50 ms, and then uniformly spaced every 20 ms to 130 ms. (i.e. TE =5, 10, 15, 20, 25, 30, 35, 40, 45, 50, 70, 90, 110, and, 130 ms). The first echo (5 ms) was not included in curve fitting because the signal was low in MSME sequence for all subjects and phantoms. A graph of signal intensity against TE in the water phantom is shown in figure 3-6. The first echo time (5 ms) consistently gave lower signal than the second TE value which is not consistent with mono- or bi-exponential decay. This TE point was discarded from all data sets for T_2 calculations. The rest of the parameters are shown in table 3-2. The slice selective 90° and 180° RF pulses were Gaussian pulses. The MSME was performed with one average giving a total scan time about 20 minutes.

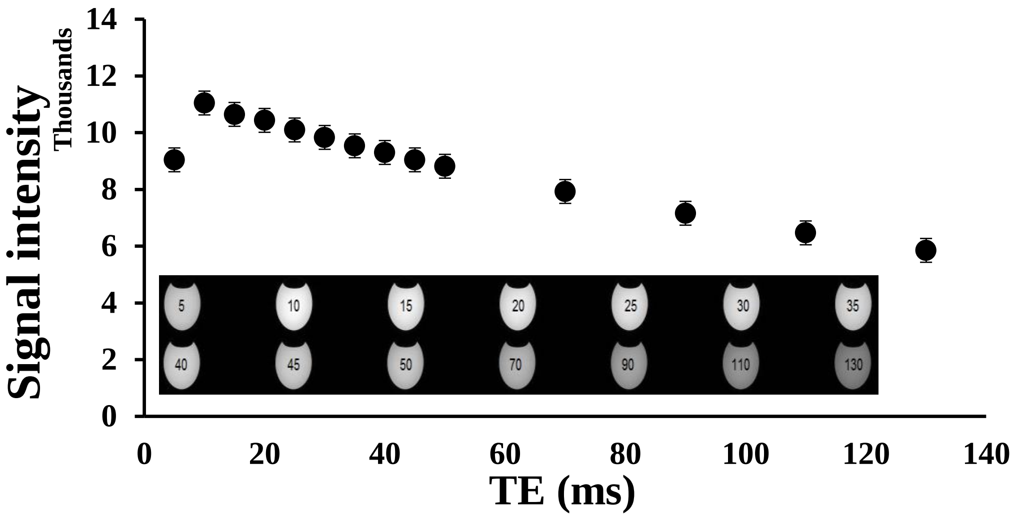

Figure 3-6: A graph of MR signal decays for the water phantom (axial slices) which shows lower signal in the first echo time (5 ms) compared to the next TE (10 ms) which is not consistent with mono- or bi-exponential decay.

Table 3-2. T_2 parameters for phantom and animal

Sequence	**TR (ms)**	**TE (ms)**	**NEX**	**Matrix**	**Slice thickness**	**FOV (cm)**	**Other specific parameters**
T_2 MSME	3300	5,10,15,20,25,30,35, 40,45,50,70,90,110, and 130	1	196×196	1.5	8×8	Flip angle 90^0-180^0

3.2.4 T_2 Optimization discussion

An important component of this study was to move beyond estimating the average T_2 relaxation of the liver tissue determined using a T_2 mono-exponential fit. A bi-exponential model to characterize the two major T_2 components T_2 of the rat liver *in vivo*.

Accurate T_2 mapping relies on acquisition of a series of echoes during a series of refocusing pulses. The assumption is that the signal decay occurs only due to the T_2 decay. However, imperfection of RF refocusing pulses due to transmit field (B_1) inhomogeneity, nonrectangular slice profiles, static (B_0), and a B_1 calibration errors can contribute to signal intensity changes along with stimulated echo formation that constructively interferes with all echoes except the first echo. This systematic error is accounted for by removing the first echo, 5ms in this case. [173]. Removing the first echo (TE=5 ms) improved the fit of the mono- and bi-exponential signal decay functions.

The accuracy of a measured T_2 value is related to the number and range of the echo times acquired [174]. Increasing the number of data points and ensuring the long TE images approach the noise level, increases the accuracy of the curve fit. This is shown in the case for the liver with diffuse fat infiltration, as the T_2 relaxation times were longer than the T_2 times for the normal liver parenchyma. This resulted in the signal intensity at TE = 50 not approaching the noise level and an underestimation of the T_2 values. This contributed to the average of T_2 values not being significantly different for the control and CDAA rats in the first two scan times when only 9 TEs ranging from 5-50 ms were used. Therefore, we extended the number of echo times up to 130 ms (total 13 TEs) to cover the complete T_2 range in rat liver and to yield more accurate T_2 measurement.

3.3 Diffusion weighted imaging

Diffusion weighted imaging, including echo planer-spin echo (SE) imaging (EPI-SE) and SE-DWI sequences, was tested at 9.4T to investigate diffusion image quality with respiratory gating in the liver. The SE-DWI sequence generally leads to increase the signal intensity and decreased image distortion, while the EPI-SE allows reduced total scan time. However, the physiological constrains such as respiratory and cardiac motion in a living animal degraded the quality images of both sequences. These sources of motion resulted in localisation artefacts due to phase errors in k-space, which were particularly evident at tissue boundaries. Furthermore, EPI-SE suffered from severe blurring and distortion images in high *b* values. These susceptibility artefacts (distortion image) were very severe at air–tissue boundaries such as liver-stomach interfaces. One way of reducing the distortion artefact in EPI images is to decrease the echo train length by increasing the number of segments or blocks in which the k-space data is acquired. Therefore, repeating the acquisitions with 2 and 4 segments was tested. Increasing the segments leads to an increase the total scan time, from approx. 1 hour to approx. 2 and 3.45 hours for 2 and 4 segments respectively, because each segment requires separate excitation pulses. The multiple blocks of data introduce new and severe motion artefact to the images. Saturation bands were applied to null signal surrounding the liver, to potentially reduce the motion artefacts and image ghosting. The saturation bands did not eliminate the artefacts. SE-DWI sequence took 35 minutes to acquire only 2 slices. Artefacts and image inhomogeneity were still not reduced to an acceptable level. Figure 3-7 presents an example from our work, showing DWI images acquired as follows: 1) SE-DWI sequence; 2) EPI-SE sequence 3) changing phase encoding direction, 2) increasing number of segments, 3) different *b*-values; and 4) adding saturation band pulse on unwanted area to avoid motion artefact.

In conclusion, all DWI images produced by different methods and parameters displayed low image quality due to susceptibility effects, chemical shift and motion artefacts. This resulted in unreliable determination of diffusion parameters in the liver. Therefore, DWI was cancelled in our study.

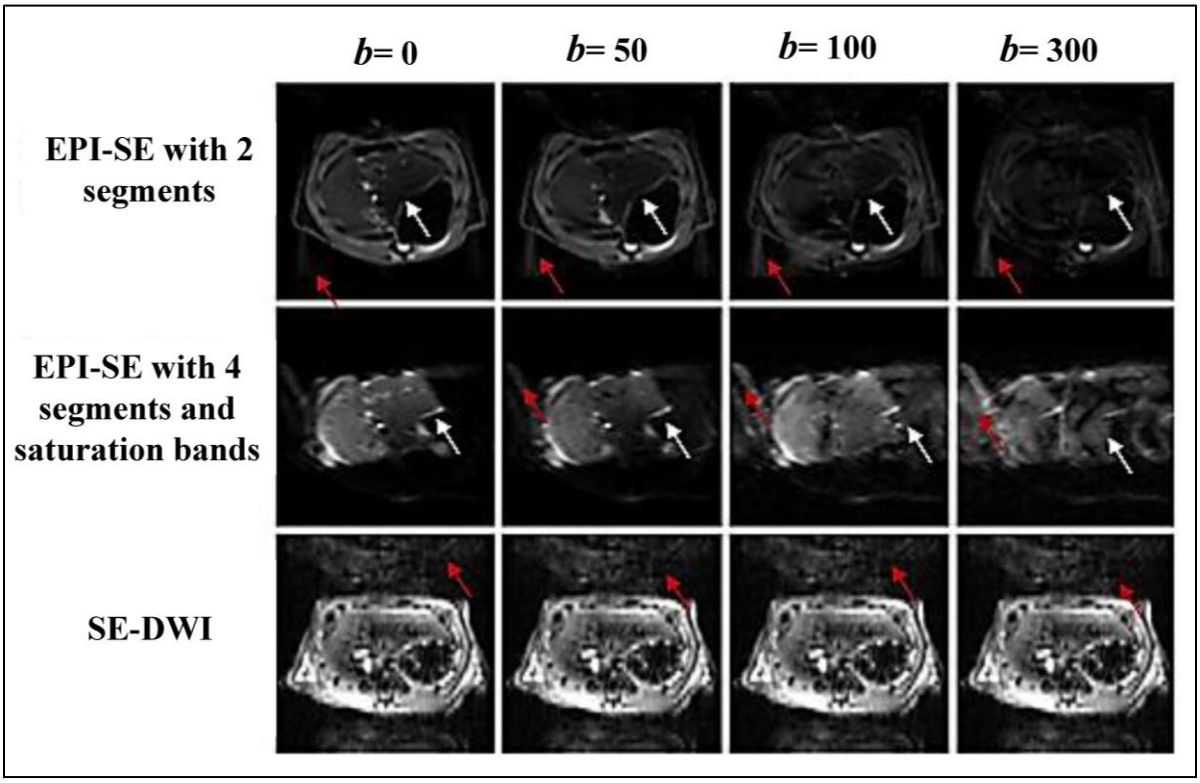

Figure 3-7: An *in vivo* DW images acquired with EPI-SE and SE-DWI sequences (with b-value = 0, 50, 100, and 300 s/mm^2) showing the effect of motion artefacts on images (red arrows). Motion artefact are more evident when the phase encoding direction is oriented left to right (middle images) compared to anterior to posterior direction (top images). Note that the motion artefact gets worse with higher b values in EPI-SE sequences. Marked distortion artefact on EPI images at liver-stomach margin are detectable in EPI-SE sequence (white arrows).

Chapter 4 : Image analysis

4.1 Qualitative evaluation and lesion detection

The qualitative evaluation (visual assessment) of images required obvious contrast differences between different tissue types and normal and pathological tissue. Differences in liver image intensity was evident between control and CDAA livers in T_2 and IP/OP images. For fatty liver disease, there were marked differences in signal intensity of the fatty lesion on IP and OP images, due to the signal cancellation in the OP phase images compared to the high signal on IP images, suggesting the presence of fat. Focal lesions were detected, defined (size and shape), and located due to the difference of their signals in T_2 and IP/OP compared to the surrounding liver tissue in the CDAA group. While visual qualitative assessment can detect difference from normal tissue, it performs poorly when changes are required to be tracked with time or comparisons between different groups or animals are necessary. This requires quantitative analysis of MRI parameters that allow tracking with time and statistical assessment of changes.

4.2 Quantitative *in vivo* analysis

4.2.1 Method for liver segmentation

The first task for quantitative assessment of images is to define how and where the measurements will be taken in the images. The simplest case would be to record the intensity of a selected number of pixels in the organ or region of interest. This has the potential to introduce variability. An alternative method would be to place a larger regular shaped region of interest in the organ. This samples a larger proportion of the organ. However, the greatest reproducibility can be achieved by segmenting out the whole organ or pathology. Segmentation of liver and pathological regions has an important role in the detection, classification and quantitation of focal lesions [175]. However, accurate MR segmentation of liver is difficult due to its complex shape and because the MR signal intensity distribution of surrounding tissue can be of similar image intensity resulting in poor segmentation. For example, the boundaries between liver and adjacent organs such as kidneys generally have similar MR intensity, which often leads to over segmentation of the liver [176]. In addition, MR liver imaging may be affected by artifacts such as abdominal motion which leads to blurring of tissue boundaries making accurate liver segmentation difficult.

Different methods can be used to segment medical images. Not all methods are suitable for MR liver images due to MR signal inhomogeneity, weak delineation of boundary, and noise [177]; also, the liver shape changes during respiratory movements in a complex way [178]. All these obstacles lead the segmentation of MR liver to be a complex and challenging task [177]. The methods of segmentation discussed in this chapter compared Medical Image Processing, Analysis and Visualization (MIPAV) and ITK-SNAP software. All Bruker format (2dseq) images were first converted to NIfTI format images in MIPAV before further analysis in MIPAV or analysis in ITK-SNAP.

4.2.1.1 MIPAV segmentation

The MIPAV application allows quantitative analysis and visualization of medical images. For liver segmentation purposes, we performed a thresholding on T_2, OP, and IP images to generate colour maps for better liver visualization and boundary delineation. Then, we manually outlined liver boundaries by freehand in a slice by slice manner using the polygon ROI tool. This method of manual liver segmentation used image contrast together with anatomical knowledge of liver and its surrounding tissues in OP, IP and T_2 images at each slice. The manual segmentation consisted of placing polygon points around the boundary of the liver. However, the outlines of the liver are not always clearly defined in our animals, which may lead to a degree of imprecision and error in the manual delineation of the boundary. Some areas of the liver boundary were drawn by the operator using areas of the liver boundary that were obvious as markers. This step requires significant time and required greater knowledge of the liver anatomy, software and operator training to achieve consistent results. An example of manually outlined liver segmentation is shown in figure 4-1.

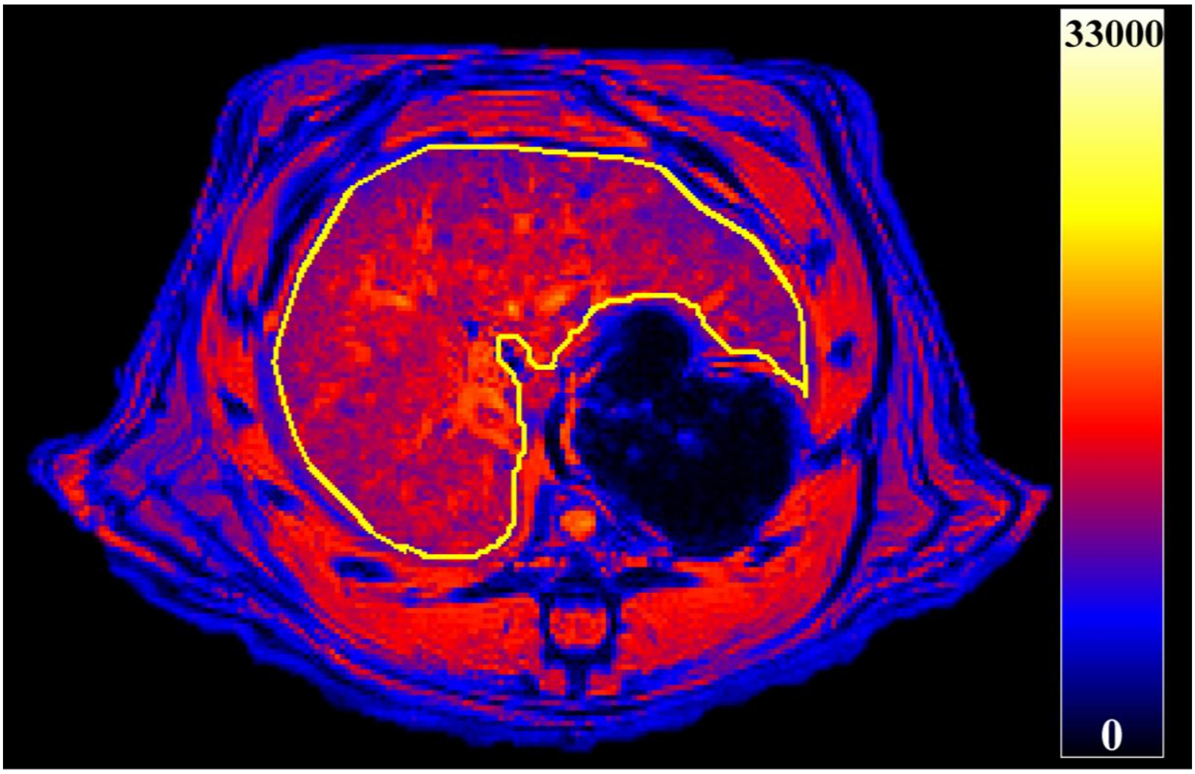

Figure 4-1: A rat liver with using a free hand segmentation (yellow outline) in one slice around the border of the coloured liver.

4.2.1.2 ITK-SNAP software

Semi-automatic segmentation using ITK-SNAP software was then tested for liver segmentation. The method is grey level-based controlled growth from seed points. This method started by adjusting the image contrast and image blur to maximise contrast of the liver. The seed points (bubbles) are placed in the target (liver). The bubbles were drawn randomly throughout the liver (figure 4-2).

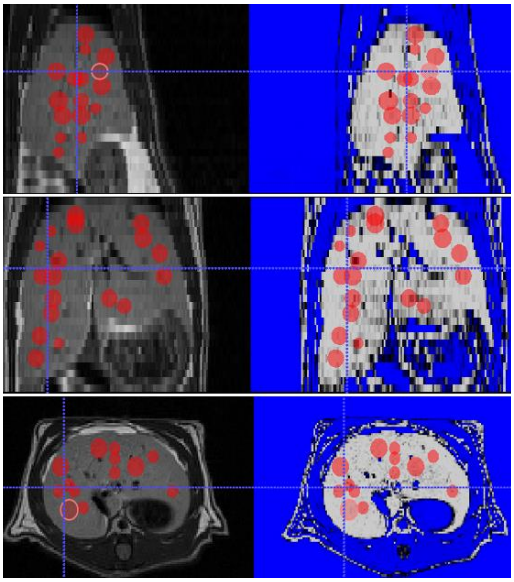

Figure 4-2: MR sagittal (left top), coronal (left middle), and axial (left lower) of a rat liver. The ITK-snap segmentation begins with adjusting the settings of the intensity region filter to the liver tissues (right images) and then create volumes with "bubbles" that expand to fill the entire liver.

Then we ran the region growing method automatically so the bubbles expanded and propagated to the neighbourhood pixels, which had a defined range of grey level intensities to all liver slices to obtain the mask. The ITK-SNAP intensity growth method did not prove to be an accurate method for liver segmentation in our work for two main reasons. Firstly, the image intensity within the liver was not homogeneous and the contrast difference between the liver and surrounding tissue was variable. This resulted in an area of liver tissue not being selected, and the ROI extending outside the liver to adjoining tissue, such as kidney (figure 4-3).

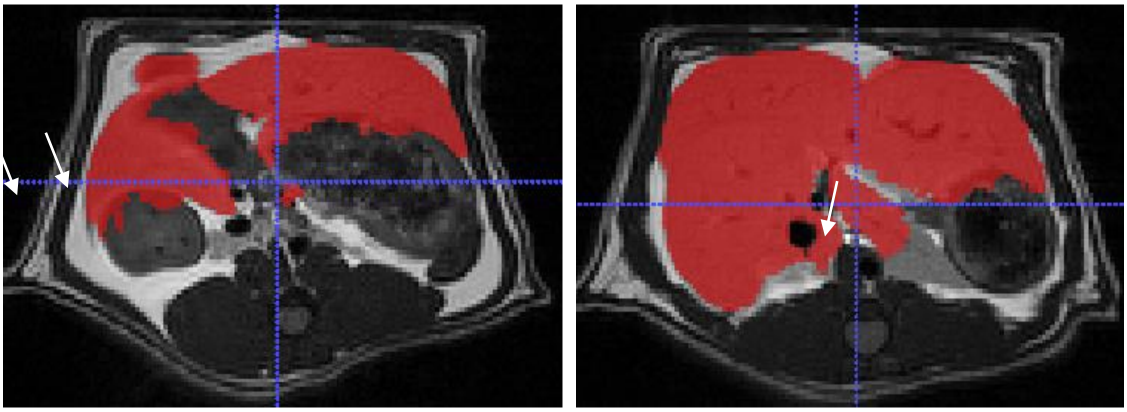

Figure 4-3: Two different slices with ITK-SNAP segmentation (red colour) after the bubbles

spread out. Segmentation was not appropriate since it covers part of the kidney (left image; 2 arrows), and did not cover part of the liver (right image; an arrow).

Segmentation summary, full manual segmentation using MIPAV software was used to segment the liver. This required greater input by the operator to include all the liver tissue and avoid neighbouring organs with similar grey scale intensity. It requires a trained operator and required significant time for each animal (~ 20 min), but gave superior segmentation of the liver.

4.2.1.3 Liver parenchyma

After the boundary of the liver was segmented manually, further segmentation was required to ensure only liver parenchymal tissue was selected. This required segmentation and subtraction of regions containing vascular tissue in the liver. This is done by using a histogram of the liver and visually selecting high intensity pixels that represent vascular regions. These vascular regions were then subtracted from the whole liver ROI to liver parenchyma, as illustrated in figure 4-4.

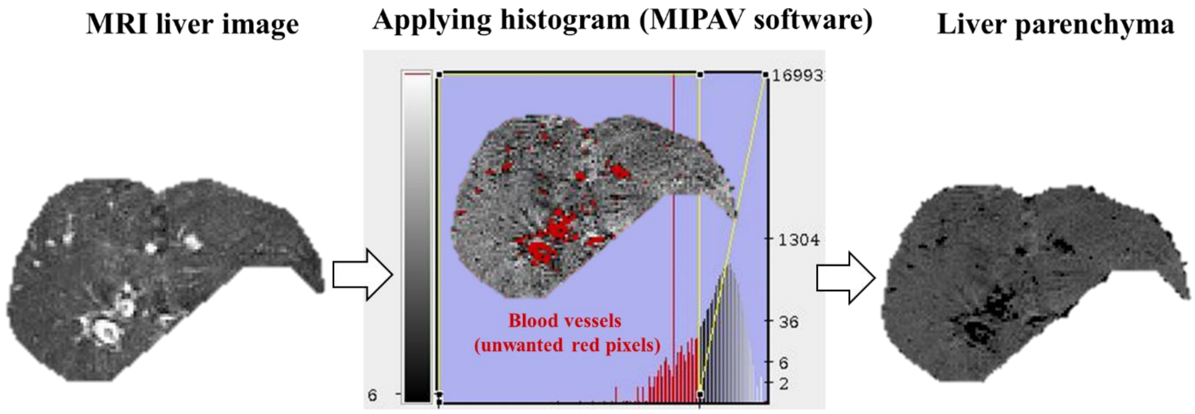

Figure 4-4: Axial MR image of a rat liver (left). The histogram is applied to exclude the intensity of the major blood vessels (red pixels on the middle image) and then liver parenchyma is defined (right image).

4.2.2 T_2 mapping

Mono- and bi-exponential T_2 fitting of the data was investigated in this study. For mono-exponential fitting the following equation was used:

$$S(TE) = S_0 e^{-\mathrm{TE}/T_{2\mathrm{M}}} + C, \tag{4}$$

where S is the observed signal, TE is the echo time, S_0 is the signal intensity at TE = 0 ms, T_{2M} is the mono-exponential decay constant and C is a constant baseline term.

For bi-exponential analysis of the data, the following equation was used:

$$S(TE) = S_0\,(f.\,e^{-\mathrm{TE}/T_{2S}} + (1-f)e^{-\mathrm{TE}/T_{2L}}) + C. \quad (5)$$

Where T_{2L} is the long component of the spin-spin relaxation time corresponding to the slowly decaying compartment of the dual component pool (i.e. fat), T_{2S} is that of the fast decaying component, f is the fractional contribution of the fast decaying component contributing to S_0, and 1- f is the long decaying compartment contributing to S_0. The f and (1-f) are symbolised in this paper as ρ_S and ρ_L, respectively [8].

Curve fitting of the data to equations 4 and 5 were performed with MatLab software (version – R2013A, MathWorks, Natick, MA) on a Dell Precision T7910 Workstation running Ubuntu 14.04.5 LTS 64-bit operating system. These workstations are equipped with Dual Intel Xeon processors (14C HT, 35MB Cache, 2.3Ghz Turbo), 192 GB of RAM, and NVIDIA Quadro K4200 4GB graphics cards. All curve fitting was applied using the "fit" function from Matlab's curvefit toolbox, using the Trust-Region optimisation algorithm. The script written for the T_2 mapping is addressed in the appendix.

Three statistical measures were used to determine the appropriateness of the model. These were, the fit correlation coefficient r^2, F test, and Akaike's Information Criteria (AIC). The coefficient of determination (r^2; equation. 6) is used to evaluate the goodness of fit from least squares regression, with values close to one indicating strong correlation between the fitted curve and experimental data.

$$r^2 = 1 - \frac{SSr}{SSt} \quad (6)$$

In equation 6, SSr is the sum of squares due to error from best-fit curve and SSt the total sum of squares.

The second criteria for estimation of the goodness of fit was F test statistics where

$$\text{F test} = \frac{(SSr_{mono} - SSr_{bi})/(df_{mono} - df_{bi})}{(SSr_{bi}/df_{bi})} \quad (7)$$

and SSr_{mono} and SSr_{bi} are the residual sum of squares for mono- and bi-exponential models, respectively - each having df_{mono} and df_{bi} degrees-of-freedom. The degrees of freedom for each model is equal to the number of data points (i.e. number of TEs) minus the number of parameters (i.e. 2 for mono and 4 for the bi-exponential model). If the associated P value is less than 0.05 then the bi-exponential model fits the data significantly better than the mono-exponential model.

The final criteria used to assess the relative performance of mono- and bi-exponential models was the AIC. The AIC is a measure which balances the goodness of fit of a model, with the model complexity. Models with more parameters will always fit the data better, hence r^2 approaches unity, than a nested model with fewer parameters. To penalise model complexity, AIC increases with the number of free parameters in the model. Thus AIC is lower for models with smaller residuals, and models with lower AIC are considered to have greater model parsimony, and are thus preferred. The AIC is defined as,

$$\mathrm{AIC} = -4\, n\log\left(\frac{\mathrm{RSS}}{n}\right) k \tag{8}$$

where n = number of echo images, RSS = residual sum of squares, and k is the number of free model parameters. There are three free parameters in the mono-exponential model (S_0, $T_{2\mathrm{M}}$, and C) and five in the bi-exponential model (S_0, ρ_S, $T_{2\mathrm{L}}$, $T_{2\mathrm{S}}$, and C).

After the T_2 liver images were segmented, a mask (binary map) was created using MIPAV software for T_2 mono- and bi-exponential fitting procedure using equation 4 and 5 in Matlab. The T_2 mappings were then calculated on the NIfTI format images in MIPAV software. Nine maps were generated including: mono-exponential ($T_{2\mathrm{M}}$) maps, the long component of the bi-exponential ($T_{2\mathrm{L}}$) maps, the short component of the bi-exponential ($T_{2\mathrm{S}}$) maps, signal fraction contribution from $T_{2\mathrm{S}}$ (ρ_S), signal fraction contribution from $T_{2\mathrm{L}}$ (ρ_L), two coefficient of determination (r^2, fit precision) maps for the mono- and bi-exponential procedures, and the estimated bulk signal intensity from mono- and bi-exponential procedures (figure 4-5)

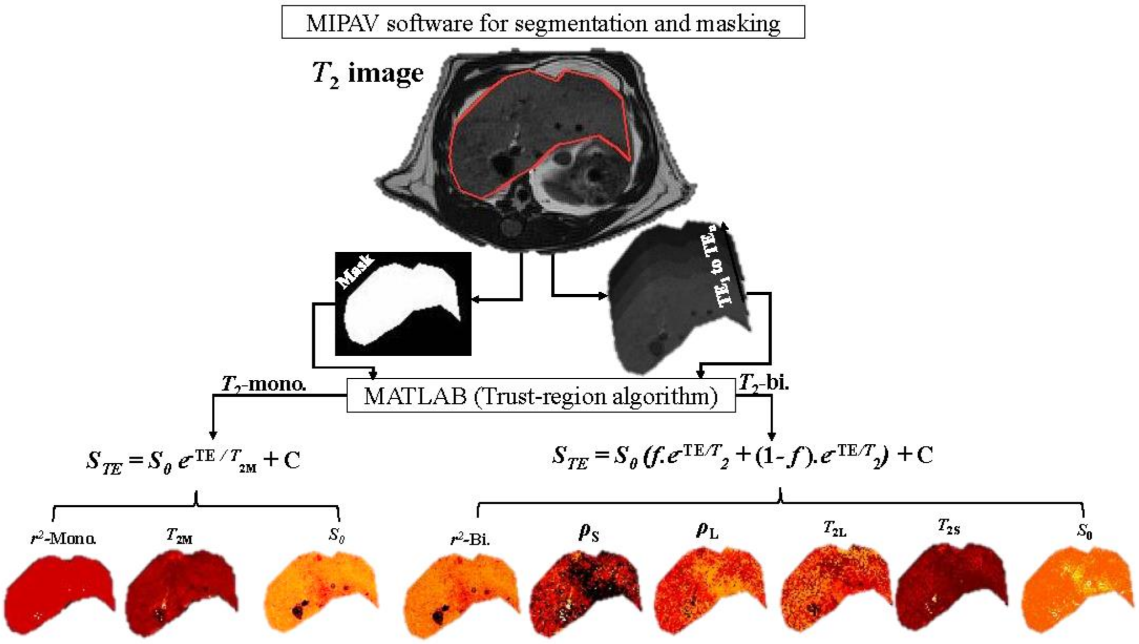

Figure 4-5: Example of mono- and bi-component T_2 analysis of a rat liver. The mask is created first from the T_2 images for T_2 mono- and bi-exponential mapping and then apply equations 4 and 5 to generate three maps for mono- and six maps for bi-exponential. The bi-exponential T_2 analysis includes r^2-Bi map for bi-exponential T_2 calculation; the long component of the bi-exponential (T_{2L}) maps, the short component of the bi-exponential (T_{2S}) maps, signal fraction contribution from T_{2S} (ρ_S), signal fraction contribution from T_{2L} (ρ_L), and the maximum signal intensity at TE=0, from bi-exponential procedures. For mono-exponential T_2 analysis: r^2-Mono map for mono-exponential T_2 calculation; mono-exponential (T_{2M}) map, and the maximum signal intensity at TE=0 from mono -exponential procedures.

4.2.3 FF estimation using the Dixon method

The fat fraction can be determined using the Dixon method using the following equation.

$$100 * \frac{(SI_{IP} - SI_{OP})}{2 * SI_{IP}} \qquad (9)$$

where SI_{IP} is the signal intensity measured in the SI_{IP} image and SI_{OP} is the signal intensity derived from OP image. The mean signal intensity of FF (in arbitrary units) was calculated from the whole liver.

Using the two point Dixon method is only valid up to fat fraction values of less than

50%. When the fat intensity becomes greater than 50% it becomes the dominant signal, and the calculated value begins to decrease to zero. We assumed the calculated T_2 long value represented liver fat component, the T_{2L} fraction did not exceed 40%, so we assume the livers did not exceed a fat load of > 50%.

This equation was applied pixel-by-pixel on the image using MIPAV software to generate a FF map and thus estimates the fat fraction intensity with dynamic range of 0–50%. Figure 4-6 shows an example of FF map obtained from IP and OP images using equation 9.

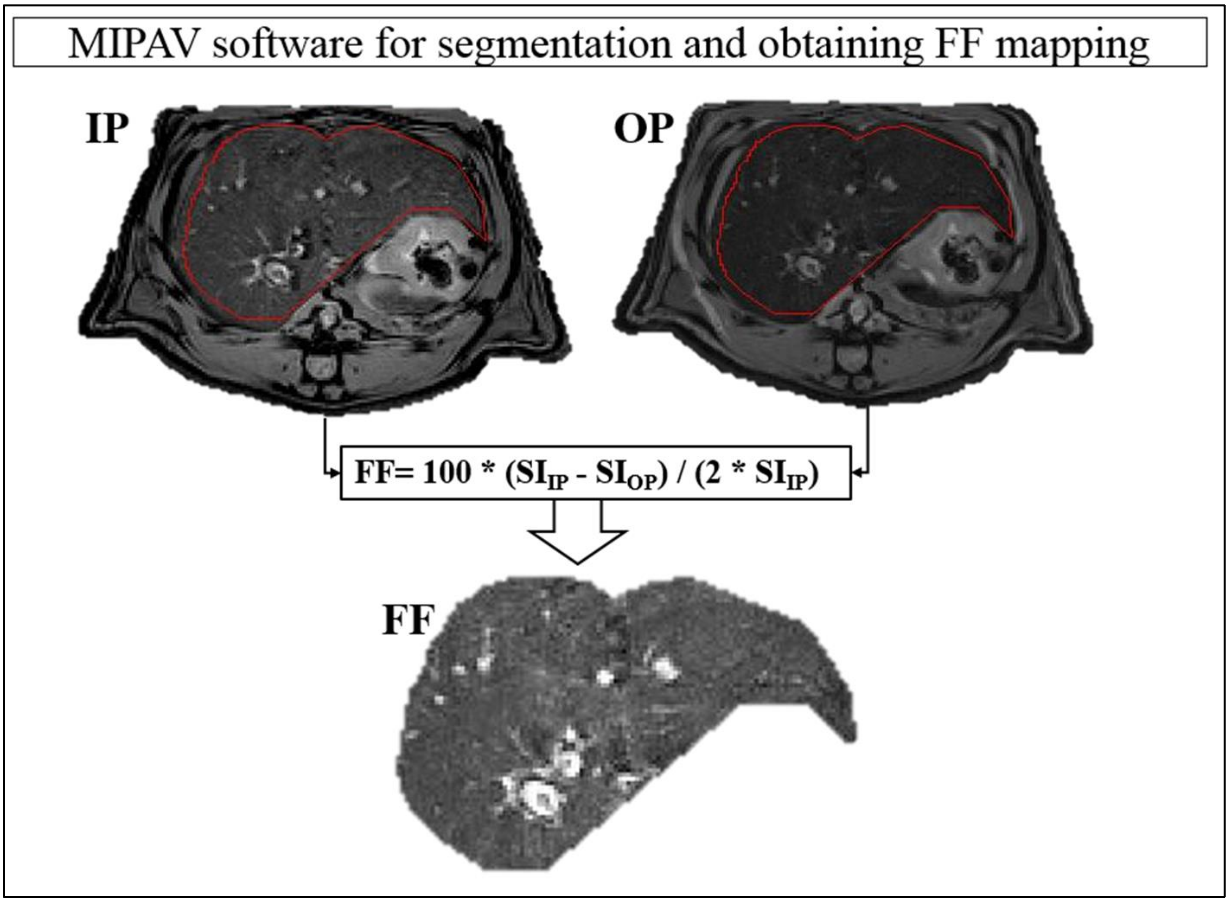

Figure 4-6: Diffuse fatty lesion in the whole CDAA liver rat in IP and OP imaging. Fat fraction (FF) map is calculated on a pixel-by-pixel basis using dual Dixon method (IP/OP imaging) using equation 9.

4.2.4 FF and T_2 quantitative analysis of whole liver and nodules

The pixel-wise method was used to generate FF and T_2 images for the segmented parenchyma regions. These parameter images were used to calculate mean FF and T_2 values for the whole liver.

When nodules were detected, they were segmented using the IP, OP and T_2 images to guide manual selection of the nodule using the free-hand drawing tool in MIPAV, as illustrated in figure 4-7. The ROI was then transferred into the FF and T_2 parameter images to determine the FF and T_2 parameters for the nodule. The nodules were not always clearly defined in the FF and T_2 parameter images. This allowed the FF and T_2 parameters to be determined for the nodules.

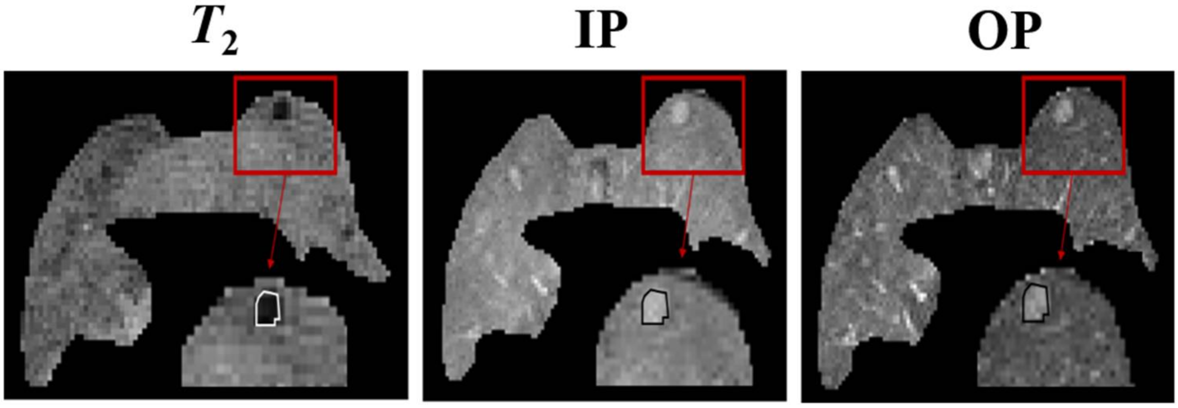

Figure 4-7: A CDAA animal at week 24 time point. Axial images of T_2, IP, and OP images show a small nodular lesion (red rectangular). ROI (black and white lines in magnified images) was outlined to cover only a homogenous intensity using a free hand drawing.

4.3 Statistical analysis

All statistical calculations were performed for *in vivo* data using SigmaPlot software (version 11, Systat Software Inc., CA, USA).

4.3.1 Mono- Vs bi-exponential goodness-of-fit statistic

To determine if a mono- or bi-exponential fit best represents the livers in control and CDAA animals, the goodness of fit was tested using r^2 (equation 6), F test (equation 7) and AIC (equation 8) on a pixel by pixel basis. For each pixel, the best fit was determined and assigned to that model, e.g., bi-exponential. Then the percentage of pixels assigned to mono- or bi-exponential was determined. The model with the highest percentage of pixels was assumed to be the preferable model for that liver. This was applied to each group at each time point and used as summary statistics to assess which model is the best fit for the T_2 signal of the whole liver and nodules.

4.3.2 Between groups and nodules versus surrounding tissue

Statistical analyses were performed using SigmaPlot software. MR parameters were averaged over all liver pixels to give a summary statistic for each subject. The mean and standard deviations of these summary statistics were calculated for each group. All liver-averaged MR parameters were tested for normality using Shapiro–Wilk tests. Independent Student's *t* test was used to compare liver-averaged MR parameters between groups (control versus CDAA groups) as well as nodules versus surrounding liver tissue in CDAA group. A *P* value less than 0.05 was considered to indicate a statistically significant difference.

4.3.3 MR parameter changes over time

The changes of each MR parameters over time (e.g. increased or decreased during diet period) in the CDAA group were examined using repeated measures ANOVA followed by a two-tailed multiple comparison procedure (student's *t* test method); a P value < 0.05 was considered statistically significant. For repeated measures analysis, the dependent variables were MR parameters at scan time points: week 12, 24, 32, 40, 48, 52, and 57

4.3.4 Correlation

Correlation between the mean MR parameters was evaluated using the Pearson correlation coefficient (*r*) on the basis of time point of MR scan. Correlations were considered statistically significant with $P < 0.05$. The mean T_2 parameters were correlated and plotted against FF to investigate whether FF has influence on these parameters.

Chapter 5 : Mono- Vs Bi- exponential T_2 relaxometry.

Introduction

Most quantitative analysis methods in MRI, particularly in clinical application, including relaxometry or diffusion apply a single fit to the data. This results in an average value for the region, region-of-interest or pixel being analysed. This may mask changes of anatomy or chemical composition of the region being analysis. If there are changes in the values of different components in addition to changes in the rations of the different components, this may be also mask by an averaged value. In this chapter we explore the application of mono- and bi exponential T_2 analysis to rat steatotic livers. The liver fat fraction will be measured using Dixon imaging. Multiple TE experiments will be acquired and analysed with mono- and bi-exponential analysis. The separate components will be correlated with the fat fractions to investigate which is the best T_2 model to analyse livers with different grades of steatosis.

Published as "Sami Alghamdi, Benjamin Sinclair, Gary Cowin, Ian Brereton and Yasvir Tesiram. *Magnetic resonance spin-spin relaxation time estimation in a rat model of fatty liver disease*. Journal of Magnetic Resonance Imaging, revised submission March 2017.

* The paper has been replicated here. The contents have been altered only slightly to reflect formatting changes.

Magnetic resonance spin-spin relaxation time estimation in a rat model of fatty liver disease

Author Names:
Sami Alghamdi[1, 2], MSc;
Benjamin Sinclair[1], PhD;
Gary Cowin[1], PhD;
Ian Brereton[1], PhD;
Yasvir Tesiram[1], PhD.

Author Affiliations:
1: The University of Queensland, Centre for Advanced Imaging, Brisbane, Queensland, Australia
2: College of Applied Medical Science, King Saud University, Riyadh, Saudi Arabia

Corresponding Author Info: Dr. Yasvir Tesiram; Building 57, Research Road, The University of Queensland St Lucia QLD 4072; telephone, + 61 7 334 60324; fax number, +61 7 334 60346; yas.tesiram@cai.uq.edu.au

Acknowledgments: We are grateful to Dr. Mark Wellard for suggestions and proof-reading.
Grant Support: RIBG (IB), NSSRF (YT)
Running Title: T_2 relaxometry of fatty liver disease

ABSTRACT

Purpose: Compare mono- and bi-exponential relaxation model equations in order to discriminate between normal and fatty liver disease.

Materials and Methods: Six rats on a choline deficient amino acid modified (CDAA) diet and six rats on normal chow were included in the study. Pixel – wise T_2 maps were generated using mono-exponential decay function to calculate T_{2M}, and a bi-exponential to calculate, short T_2 component (T_{2S}), long T_2 component (T_{2L}), and fraction of the short and long decaying compartment signal (ρ_S, ρ_L), respectively. Statistical F tests and Akaike's Information Criterion

(AIC) values were used to assess the relative performance of mono- and bi-exponential models.

Results: The F test and AIC showed that, in the CDAA group, the T_2 bi-exponential model describes the signal of T_2 weighted imaging in the liver better than the mono-exponential model. In contrast, the control was best described by the mono-exponential model. Mean values for T_{2M}, T_{2L}, T_{2S}, ρ_S, ρ_L were 31.2 ± 0.7ms, 72.8 ± 3.3ms, 8.2 ± 0.6ms,71.2 ± 2.1%, 30.4 ± 1.3% respectively in CDAA rats, compared to 18.8 ± 0.5ms, 32.3 ± 0.7ms, 9.2 ± 1.8ms, 79 ± 2%, 21.0 ± 1.1% in controls. All MR parameters were significantly different ($P < 0.01$), compared to controls; except T_{2S} ($P > 0.05$).

Conclusion: In the fatty liver of CDAA rats it was found that 84.8 ± 4.6% (AIC) and 61.74% ±5.11(F test) of pixels in T_2 weighted images fit the bi-exponential model ($r^2 > 0.99$) better than mono-exponential decays. In control rats, <45% (AIC) and <20% (F test) of pixels fit the bi-exponential model better with $r^2 > 0.98$.

KEYWORDS

MRI, fatty liver disease, T_2, mono- & bi-exponential

Introduction

The normal healthy liver has less than 5% fat [95] and fatty liver disease is defined as an abnormal accumulation of fat (mainly triglyceride) in hepatocytes exceeding 5% of liver weight [179]. Elevated liver fat is relatively benign, but can contribute to further complications such as inflammation, fibrosis [180-182] and cirrhosis, which is a predisposing risk factor for hepatocellular carcinoma (HCC) [182-185]. Accurate determination of liver fat and characterisation of clinical markers as a risk factor for HCC would be extremely valuable. The current standard of fat quantitation by magnetic resonance imaging (MRI) is by in / out-phase (IPOP) Dixon imaging, multiple-point Dixon, or localized spectroscopy [186, 187]. Clinically, the IPOP technique is often used for fat fraction determination due to it being widely available and relatively rapid acquisition times. When T_2^* decay is significant, the three echo Dixon method can be used to estimate hepatic fat fraction with the added advantage of yielding a rough estimate of T_2^* and thus iron load but may be affected by T_1 longitudinal relaxation [188, 189]. MR spectroscopy can provide accurate quantitative measurements of liver fat, but it is limited to single or coarse multiple voxels and in the liver can be of low sensitivity and spectral resolution [190-192].

Magnetic resonance imaging (MRI) can yield useful parameters, such as longitudinal

T_1 and transverse spin-spin T_2 relaxation times. These quantitative biomarkers have been used in preclinical and clinical research for quantifying liver iron and fat [128, 193, 194]. T_2 image contrast is dependent on the sequence echo time TE and depends on the chemical environment of the tissue at a given location [195]. These can be estimated using spin echo pulse sequences where images are collected with a series of TE times neglecting any contributions from T_1 relaxing mechanisms (i.e. TR > $5T_1$).

Extraction of T_2 values requires data fitting. Typically, tissue relaxation is modelled by a mono-exponential decay function [196] though tissue is heterogeneous and may have contributions from multiple T_2 components – at least eight resonances in fatty tissue. Analysis of T_2 decay curves could thus benefit from multi-exponential data fitting of signal intensity decay [197].

In patients with fatty liver disease, T_2 weighted images appear bright compared to normal liver, owing to the higher concentration of slowly relaxing lipid resonances present in liver parenchyma [164]. The liver tissue T_2 characteristics would vary with the percentage of fat and the ultra-structural alterations in fatty liver disease due to the long T_2 relaxation time of the fat in fatty liver disease than that in healthy liver tissue. In order to investigate the changes and diversity of spin-spin relaxation times in fatty liver, mono- and bi-exponential fitting of T_2 relaxation data was investigated in control and fatty liver rats, hypothesising that when lipids become a major component of the liver (i.e. > 5%) MR detectable signal, a single exponential T_2 fit is a poor representation of the tissue characteristics and thus fatty liver disease can be described by at least a bi-exponential model.

Materials and Methods

Animal model

All experiments were approved by the Institutional Animal Care and Use Committee. Six, 8-week old male Fisher 344 rats were placed on a choline deficient L-amino acid modified diet (CDAA) diet (manufacturer withheld for double blinded review purpose) for 12 weeks and compared control rats placed on normal diet (choline sufficient L-amino acid, CSAA). Animals were housed in cages in a room with control of humidity, light and temperature (~21 °C); and kept on a 12/12-hour light/dark cycle. The compositions of CDAA and CSAA diets have been described previously [57]. The amount of choline in CDAA and CSAA diets was 6.5 mg/kg and 14.48 g/kg, respectively. The CDAA diet induces non-alcoholic fatty liver disease in rodent models and has been used to generate fatty liver disease within the first 12 weeks of CDAA administration [57].

In vivo MR imaging acquisition

MRI experiments were performed on CDAA and control groups 12 weeks after the start of diet administration. During MRI examinations, animals were anaesthetized with up to 3% isoflurane in a flow of 1.5 L/min oxygen. All MRI experiments were carried out on a Bruker Biospec 9.4T MRI spectrometer with BGA12 gradient set (~14G/cm), in an 86mm quadrature radio-frequency (RF) coil tuned and matched for protons (400MHz).

Slice selected 2-dimensional coronal T_2 multi-spin-echo weighted images were acquired with multiple echo times spaced uniformly every 5ms from 5 to 50ms, and then every 20ms from 50 to 130ms. The first echo time at TE = 5ms was not used in T_2 fitting due to the formation of indirect echoes [173]. Other parameters were, repetition time TR = 3300ms, field of view 80×80 mm, resolution = 417×417 µm, slice thickness = 1.5 mm, and number of slices = 24. The total time for T_2 weighted imaging was ~11 minutes increasing to ~20 minutes with respiratory triggering. The various parameters returned from curve fitting as described below were compared with fat fractions determined by Dixon's two-point method and as summarized in reference [198].

At 9.4T with TE = 2.86ms, the resonance line from aliphatic methylene groups of lipids are in-phase with water proton resonances and with TE = 4.64ms opposed phase. Neglecting relaxation due to T_2^*, water only and fat only images can be determined according equations 10 & 11 [198].

$$W = 0.5 \cdot |S_{IP} + S_{OP}| \tag{10}$$

$$F = 0.5 \cdot |S_{IP} - S_{OP}| \tag{11}$$

The reader is referred to detailed discussions of methods of fat fraction determination in various recent articles [95, 191, 198]. In this study, fat fraction determination is limited to 50% and since we are only interested in liver fat fraction at an early stage, this limit is of little consequence in comparisons with spin-spin densities determined from T_2 maps.

Phantom Experiments

In order to validate experimental results, a series of oil/water emulsions similar to the method as presented in [199] were prepared. Briefly, commercially available olive oil was dried over sodium sulfate and 0 to 100% v/v mixtures (in 10% increments) of oil and water were combined to a total volume of 5mL in 10mL conical centrifuge tubes. To this, ~0.02g of sodium dodecyl sulfate (SDS) was added, briefly mixed by shaking and sonicated using an ultrasonic processor (SONICS, Vibra-Cell 500W) equipped with a tapered micro-tip. This mixture was pulsed for 5/10 second on/off cycle for a total duration of 180 seconds with the tube immersed in ice to minimise oxidation of the oil. The resulting emulsions were packed into 2mL Eppendorf vials and imaged at 9.4T with imaging protocols as described above, but with 128 echoes from 6ms in 6ms increments. Dixon images were collected with the same echo times as above.

Image analysis and statistical analysis

Two model candidates were chosen for comparison, mono- and bi-exponential decay functions where the mono-exponential decay function assumes that within a pixel, there is only a single spin type contributing to relaxation (e.g. water). In other words, within a pixel there is only a dominant spin of liver water and thus one T_2 value. In fatty tissue, this is not true and the presence of another spin type leads to a dual exponential decay. For example, Dixon's two-point MRI technique assumes that a fatty lesion has two main components contributing to the total MR signal. These two components are derived from two signal sources, water and fat spins [46] (specifically methylene groups of aliphatic lipid species with chemical shift at 1.3ppm) and give rise to a natural signal cancellation when the two resonances are anti-phase. Collecting an additional image with signals in-phase allows determination of fat fraction.

Unlike Dixon imaging, T_2 weighted images are collected with a balanced spin-echo sequence where the delay either side of the refocusing pulse is equal. With these sequences, comparison of fat suppressed images with non-suppressed images can yield similar information on fat fraction. Neglecting any chemical shift artefacts, the relaxation decay profile of non-suppressed T_2 images will be modulated by decay characteristics arising from fat and water resonances. Thus a bi-exponential decay function would be a relevant model yielding two T_2 decay constants representative of the two molecular species. Generally, lipids have longer T_2 decay constants than liver water [164]. Thus it is assumed that short and long decay constants are representative of liver water and fat components respectively. The contribution to the signal decay from the other resonances of lipid moieties (e.g. allyl, vinyl, carbonyl and methyl groups) have been neglected, considering that their magnitudes are generally much smaller than aliphatic methylene groups [163] and their T_2 relaxation times are also significantly less [200].

T_2 data were fitted to the mono-exponential decay function,

$$S(TE) = S_0 e^{-\mathrm{TE}/T_{2\mathrm{M}}} + C, \tag{4}$$

where S is the observed signal, TE is the echo time, S_0 is the bulk signal intensity (i.e. when TE = 0), $T_{2\mathrm{M}}$ is the mono-exponential decay constant and C is a constant baseline term. The bi-exponential function is given in equation 4 comprising 5 parameters, S_0, f, $T_{2\mathrm{S}}$, $T_{2\mathrm{L}}$, and C. Here $T_{2\mathrm{L}}$ is the long component of the spin-spin relaxation time corresponding to the slowly decaying compartment of the dual component pool (i.e. fat), $T_{2\mathrm{S}}$ is that of the fast decaying component, f is the fractional contribution of the fast decaying component to S_0, and 1-f is the long decaying compartment to S_0. The f and $(1$-$f)$ are symbolised in this paper as ρ_S and ρ_L, respectively.

$$S(TE) = S_0\,(f.e^{-\mathrm{TE}/T_{2\mathrm{S}}} + (1-f)e^{-\mathrm{TE}/T_{2\mathrm{L}}}) + C. \tag{5}$$

Curve fitting of the data to equations 4 & 5 were performed with MATLAB software (version – R2013A, MathWorks, Natick, MA), using the built-in Trust-Region method installed on a Dell Precision T7910 Workstation operated with Ubuntu (version 14.04.5) 64-bit operating system. These workstations are equipped with Dual Intel Xeon processors (14C HT, 35MB Cache, 2.3Ghz Turbo), 192 GB of RAM, and NVIDIA Quadro K4200 4GB graphics cards.

Mono- and bi-exponential models were fitted to randomly selected regions of interest (ROI) in different lobes of the liver (~150 pixels), first without constraints on parameter values and second with constraints. In a first pass estimate, parameter values were determined without constraints and showed that the bi-exponential model fitted the data very well in some ROI's, but in others (~35% of the total pixels) curve fitting did not converge and showed nonsense values (e.g. negative or very large values) . Constraints were thus introduced in a second pass, utilizing first pass values from pixels which fit the data well. In this way nonsense values were excluded. Preliminary mono- and bi-exponential fitting showed fatty livers contained values ranging between, $25 < T_{2\mathrm{M}} < 100$ms, $4 < T_{2\mathrm{S}} < 50$ms, and $30 < T_{2\mathrm{L}} < 210$ms. Based on these, upper bounds were set to 50ms for $T_{2\mathrm{S}}$, and 210ms for $T_{2\mathrm{M}}$ and $T_{2\mathrm{L}}$. The lower bound on all parameters were set to 0ms, as relaxation times must be positive. The offset parameter C in equations 4, and 5 accounted for baseline drift, where the T_2 decay tends towards zero but accounts for Rician noise. Upper bounds of infinity and 100 were set for S_0 and C, respectively, and were chosen based on the observed distribution of these parameters in preliminary mono-exponential fitting. The lower and upper bounds on ρ_S for bi-exponential fitting were set to 0 and 1, respectively, as ρ_S represents a fraction of short T_2. This wide range of constraints could handle most physiologically possible values of T_2 in liver parenchyma. In clinical practice, these may need revision. The initial value of parameters T_2, S_0, and C for fits to equation 4 were 20ms, 4000ms and 0 respectively. For the bi-exponential fitting, a subject-specific and pixel-specific set of starting points was implemented, setting $S_0 = S_{(TE=10ms)}$ and $C = S_{(TE=130ms)}$. The starting points of T_{2S} and T_{2L} were estimated using the mono-exponential fit, with the starting point for T_{2S} set as T_{2M}, and the starting point for T_{2L} set as $2{*}T_{2M}$.

Three statistical measures were used to determine the appropriateness of the model. These were, the fit correlation coefficient r^2, F test, and Akaike's Information Criteria (AIC). The coefficient of determination (r^2; equation 6) is used to evaluate the goodness of fit from least squares regression, with values close to one indicating strong correlation between the fitted curve and experimental data.

$$r^2 = 1 - \frac{SSr}{SSt} \tag{6}$$

In equation 7, SSr is the sum of squares due to error from best-fit curve and SSt the total sum of squares. The second criteria for estimation of the goodness of fit was F statistics where

$$\mathrm{F} = \frac{(SSr_{mono} - SSr_{bi})/(df_{mono} - df_{bi})}{(SSr_{bi}/df_{bi})}, \tag{7}$$

and SSr_{mono} and SSr_{bi} are the residual sum of squares for mono- and bi-exponential models, respectively - each having df_{mono} and df_{bi} degrees-of-freedom. The degrees of freedom for each model is equal to the number of data points (i.e. number of TEs) minus the number of parameters (i.e. 2 for mono and 4 for the bi-exponential model). If the associated p value is less than 0.05 then the bi-exponential model fits the data significantly better than the mono-exponential model.

The final criteria used to assess the relative performance of mono- and bi-exponential models was AIC. The AIC is a measure which balances the goodness of fit of a model, with the model complexity. Models with more parameters will always fit the data better, hence r^2 approaches unity, than a nested model with fewer parameters. To penalise model complexity, AIC increases with the number of free parameters in the model. Thus AIC is lower for models with smaller residuals, and models with lower AIC are considered to have greater model parsimony, thus preferred. The AIC is defined as,

$$AIC = -4\, n\log\left(\frac{\mathrm{RSS}}{n}\right) k \tag{8}$$

where n = number of echo images, RSS = residual sum of squares, and k is the number of free model parameters. There are three free parameters in the mono-exponential model (S_0, T_{2M}, and C) and five in the bi-exponential model (S_0, ρ_S, T_{2L}, T_{2S}, and C).

In order to determine the spatial variation of mono-component and bi-component tissue, each of these three criteria was assessed at each pixel of the liver. A heuristic of overall liver composition was then calculated as the percentage of pixels in which the bi-exponential model was preferred. To achieve this, masks (binary maps) were generated by manually segmenting the whole liver from the T_2 weighted images using Medical Image Processing, Analysis and Visualization (MIPAV) software for each animal and each slice. The major vessel pixels were separated and subtracted from the liver parenchyma by applying a visually-determined intensity threshold. Mono-exponential and bi-exponential models were then fitted to all pixels within the subject-specific liver mask. Eight maps were generated. These were T_{2M}, T_{2L}, T_{2S}, ρ_S, ρ_L, r^2, F-statistic and AIC maps.

Statistical analyses and significance tests were performed using SigmaPlot software (version 11, Systat Software Inc., CA, USA). Model parameters were averaged over all liver pixels to give a summary statistic for each subject. The mean and standard deviations of these summary statistics were calculated for each group. All liver-averaged T_2 parameters were tested for normality using Shapiro–Wilk tests. Independent Student's *t* test was used to compare liver-averaged T_2 parameters between groups. A *P* value less than 0.05 was considered to indicate a statistically significant difference.

Results

Shown in Figure 5-1 are images of the oil/water emulsions using the 2-point Dixon method and T_2 decay curves of the corresponding vials also shown in Fig.1. For clarity, not all curves are shown, but as fat fraction increases the correlation coefficient, r^2 (as a measure of the goodness of fit) decreases. From this data, the mono-exponential fit shows poorer correlation when %FF > 20%. The bi-exponential fit, however yield excellent fits across the full range of fat fractions, but since a mono-exponential function also yields excellent results for %FF < 20%, we have investigated the utility of model testing to via additional statistics test to determine if these are of any additional diagnostic value.

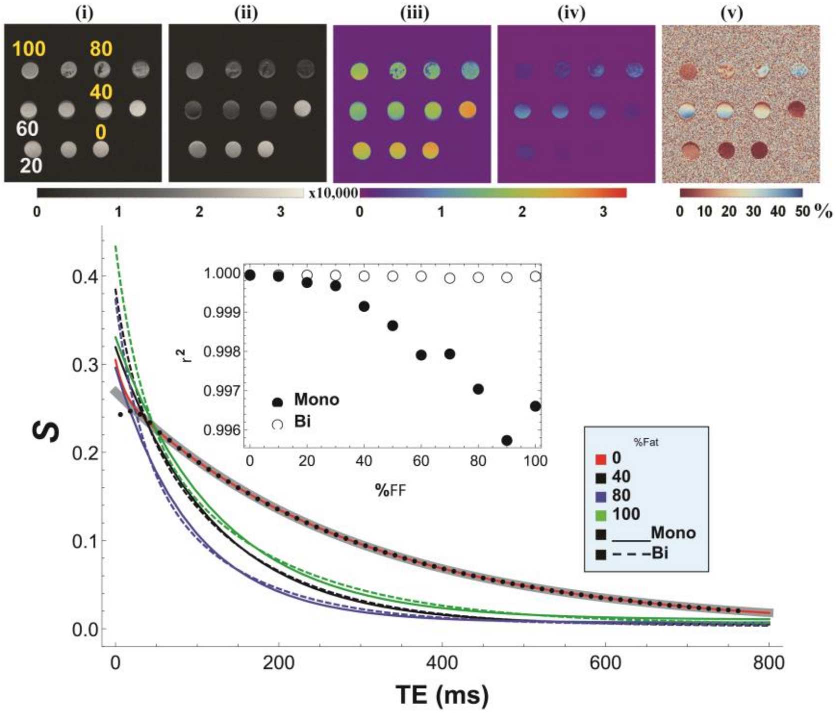

Figure 5-1: In-phase (i) and out-phase (ii) images of emulsion with varying ratios of oil and water. Using equations 10 & 11water only (iii) and fat only (iv) images can be retrieved, while fat fraction (v) can also be determined, the 2-point Dixon method using magnitude gradient echo images limits the fat fraction calculation to 50% fat, and >50% FF cannot be distinguished from water signals. Plotted are T_2 decay curves from mean pixel intensity from ROI's around the vials labelled in yellow. The white vials are labelled for convenience indicating the direction of %FF increase. Error bars from standard deviations of the mean from ROI's are not shown. The thick grey dashed line is the mono-exponential fit to the sample with 0% fat (i.e. water only) and is indistinguishable from the bi-exponential fit to equation 5. The black dots are the mean intensities from the ROI's of every second echo collected using a multi-spin echo sequence. Even echoes and points for the, 40, 80 and 100% curves are not shown for clarity. As fat fraction increases the goodness of fit decreases as shown in the plot of %FF versus r^2 and the subtle difference between mono and bi-exponential function fits.

Shown in figure 5-2 are calculated images from the Dixon method. Control animals had much lower fat accumulation (5.07 ± 1.42%, n = 6) at this early stage, but CDAA animals had accumulated fat to an average of 24.66 ± 1.1%, but heterogeneously distributed as shown in figure 5-1. As mentioned above, figure 5-3 shows the quality of data fitting based on regions of interest and pixel-wise fitting and figure 5-4 shows coronal T_2 weighted images of control and CDAA livers. Diffuse fatty liver is evident in the CDAA animal liver with higher intensity (figure 5-4a) compared to the control (figure 5-4b).

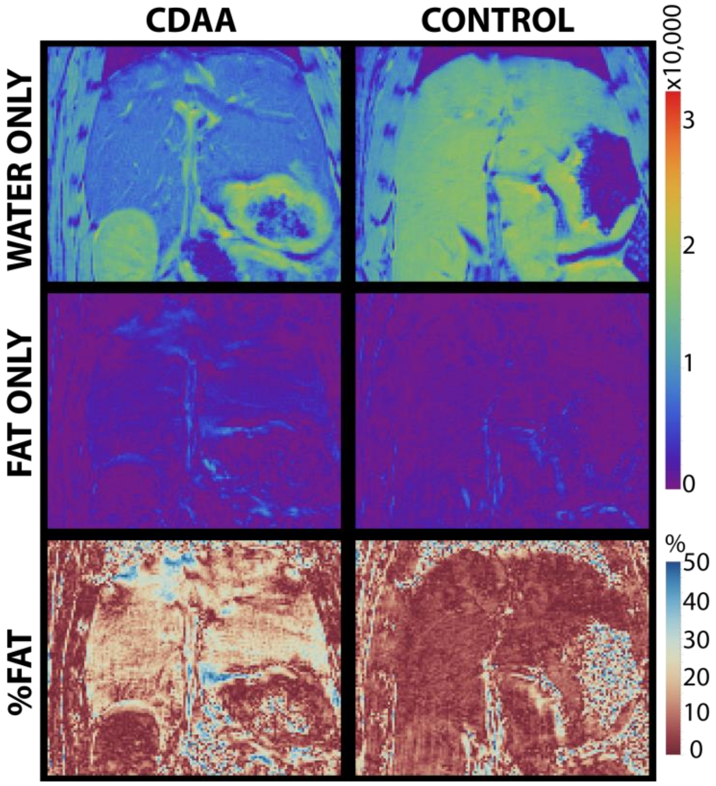

Figure 5-2: Water only, fat only, and fat fraction (%Fat) maps of CDAA and control rat livers 12 weeks after diet administration. These images are determined from to equations 10 & 11 and are presented in the integer scale (0 to 32,767). The bottom two panels of percent fat determined as 100 F / (W + F) is limited to 50%. Compared to the control, CDAA animals have a much higher fat content even at this early stage during diet administration and the difference can be easily determined. However, the heterogeneity of the distribution is not so evident and contributed to by various mechanisms in gradient echo images, including B_0 and T_2^* relaxation effects.

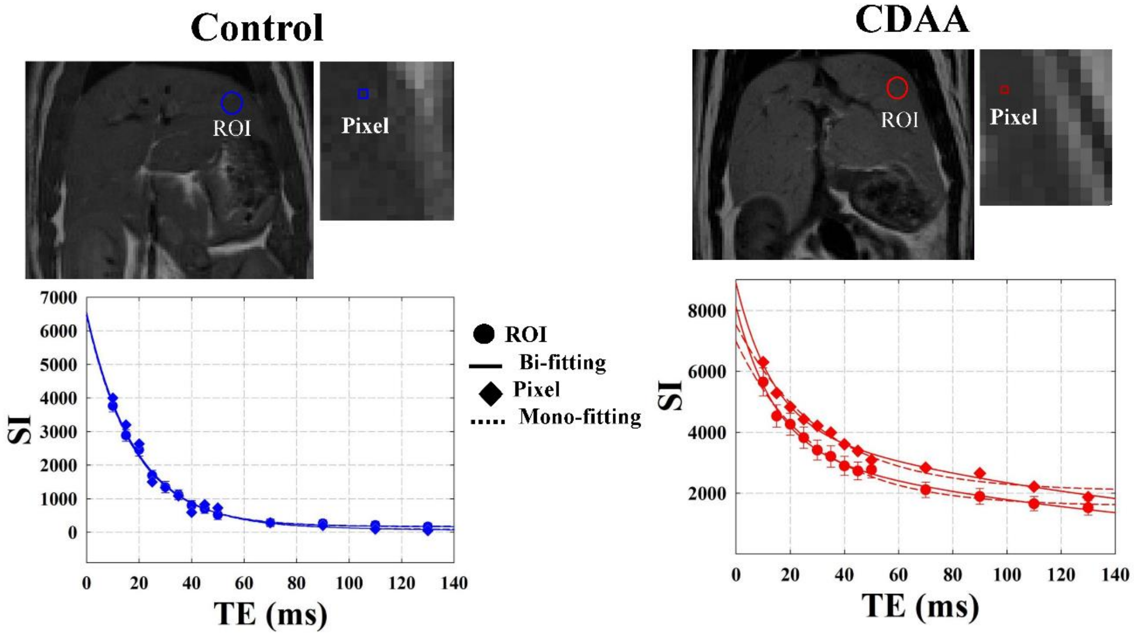

Figure 5-3: Mono- and bi-exponential T_2 fits from region of interests (ROI) and a single pixel within the ROI in a control and CDAA rat. The line fitting represents the bi-exponential fit of the data and the dashed lines represents the mono-exponential fit. (SI is the mean signal intensity and TE is the echo time).

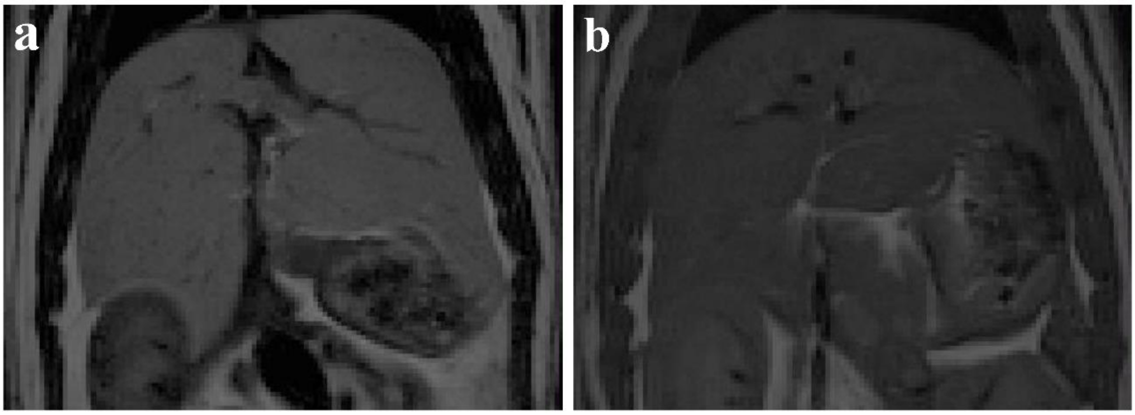

Figure 5-4: Comparison of coronal T_2 weighted images (TE/TR =50/3300 ms) between CDAA (a) and control liver (b) in Fisher 344 rats. Note the higher signal intensity in the rat with fatty disease, compared to lower signal intensity in the control rat.

Models' goodness-of-fit

Typical parametric images of the statistical parameters (r^2, F test, and AIC) resulting from the in vivo data are shown in figure 5-5.

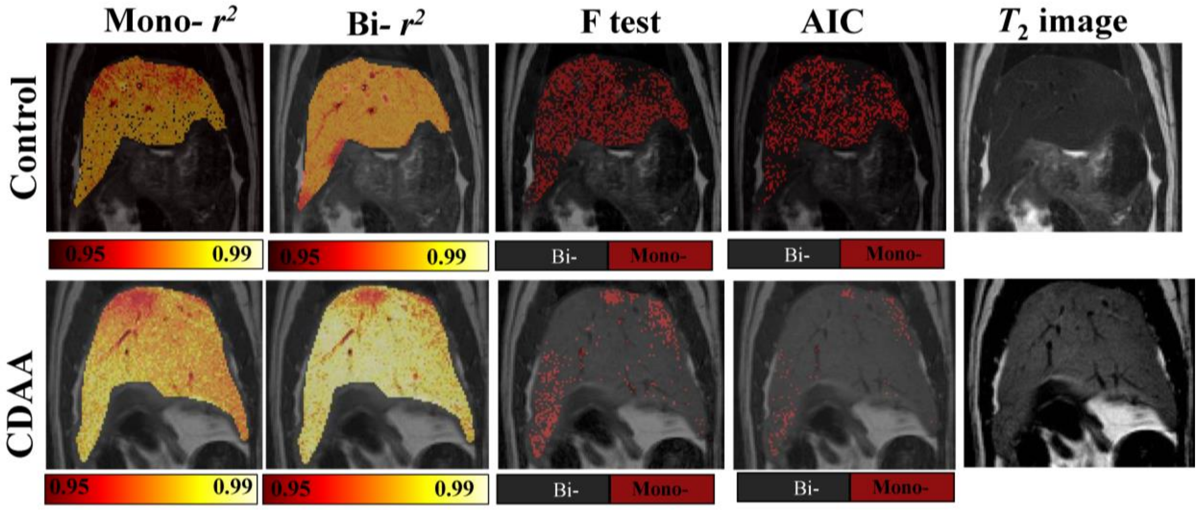

Figure 5-5: r^2 (mono- and bi-exponential) maps, F test, and AIC maps and coronal T_2 images of control and CDAA livers. The r^2 maps show that the mean overall pixels of bi-exponential fitting function in CDAA and control groups had higher precision than that with a mono-exponential fitting function. The F test and AIC maps suggest that the bi-exponential (grey pixels) fit was the preferred model rather than the mono-exponential (red pixels) for the majority of pixels across the entire liver in the CDAA animals. However, the mono-exponential model was a more appropriate model in control animals. All maps are overlaid on the T_2 image and pseudo-color-coded with the corresponding colour bar below each image.

Shapiro–Wilk test showed that the liver-averaged r^2, F test, and AIC statistical parameters were normally distributed across subjects in each group. The mean r^2 for the bi-exponential fitting function in CDAA and control groups was slightly higher ($r^2 = 0.990 \pm 0.001$ and 0.984 ± 0.001, respectively) than with a mono-exponential fitting function ($r^2 = 0.980 \pm 0.002$ and 0.979 ± 0.002, respectively). For the bi-exponential fits to the CDAA group, 63% ± 7.9 of the pixels had r^2 values greater than or equal to 0.99 while for mono-exponential fits it was 11.90% ± 2.41. In controls, 29.66% ±15.2 of the pixels were greater or equal to 0.99; and 14.7 % ± 8 for mono-exponential fits. The result of F test and AIC are summarized in figure 5-6. The F test for CDAA group showed 61.74% ± 5.11 of the pixels to be of bi-exponential behaviour, whilst for controls the proportion was 15.63 % ± 1.44. Similarly, the AIC indicated that bi-exponential model was preferred in 84.79 % ± 4.58 of the pixels in CDAA group, while in controls, more pixels (59.03 % ± 6.17) were best described by the mono-exponential model. While tissue samples were not collected in this longitudinal study until the end at 57 week's post-diet administration, previous studies have shown the accumulation of fat in hepatocytes as well as the formation of lipid droplets among other pathologies at similar time points [201].

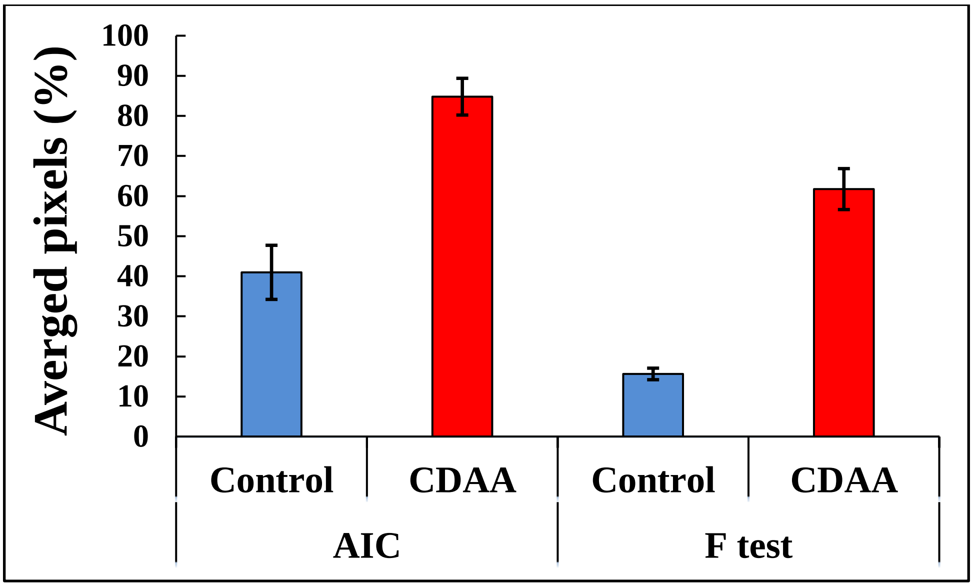

Figure 5-6: The liver-averaged AIC and F test measures showing the percentage of pixels were bi-exponential function is preferred and better from control and CDAA groups. The bi-exponential model was preferred in most of the pixels in CDAA group, while in controls, more pixels were best described by the mono-exponential model.

Between-Group Differences in T_2

Examples of T_2 maps for a control and a CDAA fatty liver are depicted in figure 5-7. The results from descriptive statistics for all T_2 parameters are summarized in Table 5-1. Using Shapiro–Wilk tests, all average T_2 parameters were normally distributed across subjects in each group. The mean T_{2M} and T_{2L} were significantly higher for CDAA compared to controls. The mean CDAA whole liver ρ_S and ρ_L were significantly lower and higher, respectively, for CDAA than controls. The significant difference between groups indicates that fatty disease affects the measurement of T_{2M}, T_{2L}, ρ_S, and ρ_L. Conversely, no significant difference was seen in T_{2S} between groups.

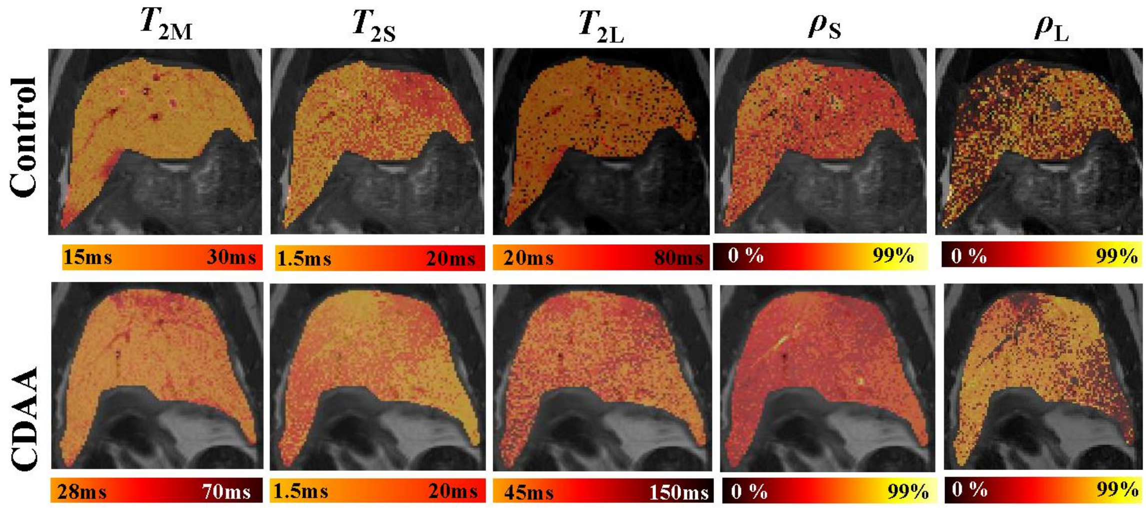

Figure 5-7: Example of mono- and bi-component T_2 analysis of a control and CDAA livers. The maps are of T_2 (T_{2M}) from mono-exponential fitting; short component (T_{2S}), long component (T_{2L}), and T_2 short and long fractions (ρ_S, ρ_L) from bi-exponential fitting. All maps are overlaid on the T_2 image and pseudo-color-coded with the corresponding colour bar below each image.

Table 5-1: Summary of MR parameters in control (n=6) and CDAA (n=6) group, and statistical significance of the mean difference between groups (P value).

ID and T_2 parameters		**Mean**	**SD**	***P* value**
T_{2M} (ms)	Control	18.81	0.5	< 0.01
	CDAA	31.18	0.69	
T_{2L} (ms)	Control	32.29	1.33	< 0.01
	CDAA	72.82	3.28	
T_{2S} (ms)	Control	9.2	0.9	> 0.05
	CDAA	8.23	0.6	
ρ_S (%)	Control	79	2	< 0.01
	CDAA	71.2	2.14	
ρ_L (%)	Control	21	1.1	< 0.01
	CDAA	30.39	1.28	
FF (%)	Control	5.07	1.42	< 0.01
	CDAA	24.66	1.1	

CDAA, choline deficient L-amino acid; T_{2M}, T_2 mono-exponential; T_{2L}, long T_2 component; T_{2S}, short T_2 component; ρ_S, fraction of the short compartment signal; ρ_L, fraction of the long compartment signal; FF, fat fraction obtained from Dixon method; SD, standard deviation.

Discussion

Although mono-exponential T_2 relaxation adequately describes many tissues *in vivo*, there have also been reports on non mono-exponential T_2 models in many biological tissues, particularly the bi-exponential model [202-204]. In liver, T_2 mono-exponential decay has shown promise for assessing liver disease [129, 205, 206]. A literature review showed that, there are no published studies comparing mono- and bi-exponential T_2 models for evaluating fatty liver disease. Therefore, we sought to employ a bi-exponential model to evaluate T_2 weighted images in a rat model of fatty liver disease. This includes determining whether in vivo T_2 decay curve of liver tissue is best described by a mono- or bi-exponential model from a statistical point of view using r^2, F test, and AIC statistics. The primary result of this study was that two fractions are separable in fatty liver disease and thus T_2 bi-exponential fitting is feasible for in vivo fatty liver disease and yields more accurate maps compared to mono-exponential fitting.

Parameter constraints were determined which improved the quality and computation speed for generation of pixel wise parametric maps. The method was applied to create pixel-wise T_2 maps for control and CDAA animals at week 12 after diet commencement. For bi-exponential fitting, we used equation 5 to calculate three T_2 parameters (T_{2S}, T_{2L} and ρ_S). The mean T_{2M} value estimated in control rats in this study (~18± 0.5ms) is comparable to the T_2 value in normal liver of control rats using a 7T spectrometer (22.3±2.1ms) [129].

Previous T_2 modelling studies have described living tissues as bi- or multi-exponential components, with the components interpreted as intra- and extracellular water [207-209]. In this case, T_2 short and long components determined from bi-exponential decay curves are attributed to liver water and fat components, i.e. two different chemical species. In the healthy liver, there is a little or no fat content, resulting in the dominant water signal being characterised by a single T_2 value. As the proportion of signal from fat increases, and becomes relatively less or equivalent to the water signal, we would expect that bi-exponential decay would be an appropriate model for steatotic livers.

The r^2 analysis illustrates the goodness of fit but is not a statistically informative criterion for assessing the accuracy of the model. It can be used as guide to whether the selected model fits the underlying experimental data. We saw that the bi-exponential model explained a large amount of variance in the CDAA rats, and less in the control rats. This was more formally quantified with the AIC test showing that the bi-exponential approach is the globally preferred model (in ~84% of pixels) in the CDAA group, while fewer than ~45% of pixels in control livers showed bi-exponential characteristics. Similarly, the F test showed that over 62 % of the pixels exhibit bi-exponential T_2 characteristics in CDAA group compared to 16% in the control group. These statistical model comparisons indicate the presence of a large fat component in the CDAA group, but not in normal liver tissue. The F test and AIC tests in the control group preferred mono-exponential T_2 signal decay. This may be interpreted by the absence of or low fat droplet content.

The statistical comparison between control and CDAA groups, presented in Table 1, showed that the T_2 metrics: T_{2M}, T_{2L}, ρ_S, and ρ_L were able to differentiate fatty liver disease in the CDAA group from normal liver in the control group. T_{2M}, T_{2L}, and ρ_L were significantly higher in CDAA compared to control liver, while ρ_S was lower; indicating that these four parameters are influenced by the high fat component and were thus relevant MR biomarkers to measure the underlying fatty distribution in the whole liver of the CDAA-rat model. The T_{2S} values in CDAA group and control animals were equivalent (Table 5-1). This is consistent with the assumption that T_{2S} is related to the liver water component which is present in both groups, and of similar origin and thus the short T_2 relaxation data will stay constant between groups. Collectively, these data indicate that the global increase of T_{2L} in the bi-exponential model in CDAA model is largely due to the expansion of the fat component.

The F test and AIC showed greater fit for bi-exponential analysis of the CDAA group, consistent with increased signal from the fat with a unique long T_2 value. The F test and AIC indicated that the mono-exponential model is more appropriate for more pixels in controls, consistent with the dominant single water T_2 value. The biological source of the T_{2L} in the control animal is not obvious, but may represent different water components in the tissue e.g., intracellular and extracellular water, as previously suggested, or due to fat accumulation in these strain of rat with age.

The analyses described here will be useful for studies of liver diseases, in particular, fatty liver infiltration. In this study the bi-exponential analysis better described steatotic liver, consistent with unique T_2 values for tissue water and fat. Beyond fat and water assessment, living tissue may contain multiple T_2 components for fat and water requiring multi-exponential relaxation analysis [197]. This may allow new insights into the microarchitecture of a tissue at the sub-voxel level and may improve the accuracy of in vivo measurements, thereby increasing the clinical potential of tissue characterization by MR imaging [197, 210]. For example, the non-alcoholic fatty liver disease (NAFLD) consists of a pathological spectrum including hepatic steatosis (the earliest manifestation), non-alcoholic steatohepatitis (NASH), liver fibrosis, liver cirrhosis, and finally HCC. The microarchitecture at the sub-voxel scale in the liver at each stage is likely to be altered (particularly the fat fraction), resulting in changes in bi-T_2 characteristics during the progression. We are not aware of studies investigating the influence of these stages on multi component T_2 relaxation in the liver. In this study, the presence of a T_2 long component in fatty liver indicates a different underlying chemical environment than T_2 short component. Therefore, a bi-exponential model is important to accurately determine these multiple tissue components for liver characterization in a longitudinal study, particularly, if the aim is to track drug efficacy or characterizing disease progression fatty liver disease in early stages leading to HCC in late stage.

This data is consistent with the pathological changes accompanying fatty liver being responsible for the bi-exponential T_2 relaxation. It is proposed that future work is needed to study the quantitative relationship and correlation between bi-T_2 values with liver fat fraction (% FF) to determine at what time points the bi-exponential model is preferred using F test and AIC criteria. A fat suppressed T_2 weighted sequence may yield a single decay curve that represents only the water component, leading the mono-exponential function to be the model of preference and assure that fat component is the responsible for the second decay curve. A limitation of this study was that the number of short echo times used may not provide sufficient data to support estimation of the short component of a bi-exponential model. The number of lower echo times was limited by the stimulated echo effect due to imperfections caused by the refocusing RF pulse in the MSME sequence. This resulted in decreased image intensity at very short TE times, independent of reduced T_2 signal dephasing.

In conclusion, use of parameter constraints improved the quality and computation speed for generation of pixel wise T_2 liver parametric maps in vivo. The bi-exponential model showed improved fit and better description of the data in livers containing high fat. This finding offers additional liver information which may provide potential biomarkers and scope for further investigation of liver abnormalities in vivo.

Chapter 6 : Characterization of fat fraction and T_2 relaxation in the liver of a choline and methionine deficient rat model of hepatocarcinogenesis

6.1 Introduction

The previous chapter demonstrated that the T_2 relaxation in steatotic liver is best represented by two T_2 values determined by bi-exponential analysis. This is now extended to investigate the changing pathology during the development of liver disease and the formation of liver nodules. In particular, we are interested in changing T_2 relaxation and fractions of the different components with varying fat fraction in liver tissue and during the formation of precancerous nodules. This may lead to the development of T_2 based markers that identify tissue at risk of progression to HCC.

6.2 Background

Liver cancer is the second most common cause of death globally with an overall mortality to incidence ratio of 0.95 [211]. The most important risk factors for hepatocellular carcinoma remain hepatitis viral infection (B and C), or aflatoxin exposure [5] and recently metabolic syndrome has been used to explain discrepancies observed in spontaneous or unexplained occurrence of primary HCC [212]. Non-alcoholic fatty liver disease (NAFLD) is now thought to contribute to increased rates of HCC incidence [1] and is associated with insulin resistance (or diabetes) and obesity [34]. Detecting and monitoring these pathologies is challenging and whilst histology is considered the reference standard for the assessment of liver pathology, the techniques are invasive, and prone to error [213] since lesions can be small and easily missed during biopsies [42]. Target pathologies of the liver are generally heterogeneously distributed and biopsy samples may misrepresent the extent of disease [43, 44] because of under or oversampling. It is also difficult to monitor disease longitudinally with repeat biopsies [214]. Other non-invasive techniques are available, such as ultrasound (US), computed tomography (CT) and dual energy X-ray absorption (DEXA). The latter two are limited for longitudinal examinations due to repeated radiation dose. Magnetic resonance imaging (MRI) has the potential to become a routine modality for following liver disease [215], but to harness the full potential of MRI for liver disease stratification, the MR signal has to be better characterized.

It is important to note that not all animal models of liver disease reflect the human condition accurately, and should be used within context when designing diagnostic methods for longitudinal monitoring. Lau *et al.* [216] have recently reviewed animal models of non-alcoholic fatty liver disease identifying 12 different models. These cover the spectrum of pathologies found in the clinic, ranging from obesity to hepatocellular carcinoma. A well-established model for hepatocarcinogenesis is the choline deficient L-amino acid modified (CDAA) diet. The advantage of the CDAA model is that animals develop histopathological features such as diffuse steatosis through to focal nodular lesions sequentially, closely resembling the human condition [217]. In general, diffuse fatty infiltration is expected to precede HCC development and may be indicative of malignant tumour [213] but there are few reliable biomarkers accurately predicting progression of fatty liver to HCC.

A previous study by Griffitts *et al.* [213] showed that alterations in lipid metabolism associated with hepatocarcinogenesis could be followed by chemical shift imaging (CSI) and the formation of nodules or tumors could be predicted by determining the degree of unsaturation. The present study uses the CDAA rat model to determine whether other MRI methods could be used as biomarkers of heptaocarcinogenesis. While measurement of degree of unsaturation is a biomarker of beta-oxidation, the method is relatively insensitive because it relies on the measurement of two relatively small signals, the vinyl and bis-allyl resonances of lipids. Much more sensitive are the aliphatic methylene protons and the Dixon method is a spectroscopic imaging technique commonly used for quantitation and evaluation of this resonance as a proxy for fat quantitation. This method has become the MRI reference standard for quantifying fat fraction (FF), when compared with other non-invasive methods [47] but is not without limitations [218].

Recent advancements in quantitative MRI shows that incorporation of multiple MR parameters such as relaxation times can be used to infer chemical pathology since changes in the local chemical environment should be reflected in changes of MR spin properties. Indeed measurement of longitudinal, T_1, and spin-spin, T_2, relaxation times have been proposed for detecting and staging liver fibrosis [205]. Reeder and Sirlin reviewed various MRI methods used for liver fat quantification [219] concluding that technical challenges and validation are still required. Yet more recent developments utilizing multi-parametric MRI such as a combination of diffusion weighted imaging, morphological imaging and dynamic contrast enhanced MRI have proven useful in staging cancers such as breast and prostate, the stratification of complicated risk factors and pre-cancer of the liver remains a challenge. An avenue towards addressing these challenges is the utilization of relaxometry in combination with spectroscopic imaging with validation by liver pathology.

Relaxometry experiments result in maps of T_2 and T_1 relaxation times. These parameters can provide unique information on tissue composition and structure, which vary with pathological and physiological processes allowing pathophysiological conditions to be characterized [220]. T_2 values can be extracted from the usual mono-exponential decay function, which assumes that a single spin type contributes to the signal from within that compartment. In MRI these are generally considered to be protons from water molecules. Inclusion of a second spin type within that compartment such as aliphatic methylene groups from lipids, confounds the decay characteristics of the signal but can be modelled by a two - component exponential decay function [163].

In order to investigate the characteristics of the MR signal in the presence of NAFLD we have used MRI to correlate T_2 relaxation times with FF over time in the CDAA rat model. We have analysed whether a mono- or bi-exponential model is more accurate for *in vivo* T_2 of the liver using three statistical approaches r^2, F test [221] and Akaike information criterion (AIC) [222]. MR results were verified histologically. With a better understanding of these correlations, mono-/bi-component T_2 and FF may give more accurate information about the structure and disease progression during hepatocarcinogenesis.

6.3 Materials and Methods

6.3.1 Animal model

These experiments were approved by the Biological Resources Animal Ethics committee. Eight week old Fisher 344 rats (n = 6) were placed on a choline deficient L-amino acid modified diet (CDAA) diet and compared with control rats placed on a choline sufficient diet (CSAA). The composition of CDAA and CSAA diets has been described previously [57]. The CDAA diet formulation used here is slightly lower in polyunsaturated fatty acid load, compared to similar diets used by others and thus prolongs the steatohepatitis stage, allowing ample time for imaging studies to be conducted without stress to animals. Animals were housed in pairs in a controlled environment.

6.3.2 *In vivo MR imaging*

During MRI examinations, animals were anaesthetized with up to 3% isoflurane in a flow of 1.5 L/min medical grade oxygen. MRI experiments were conducted with a Bruker Biospec 9.4T/30cm MRI spectrometer. The gradient set used could produce fields up to 14G/cm. A 86mm quadrature radio-frequency (RF) resonator tuned and matched for proton was used for all studies. Imaging workflow and protocols were standard: briefly, a scout image in axial, sagittal and coronal planes was collected within a 120mm field of view. Two-point Dixon in/out-phase (IP/OP) images [46] were collected in the axial plane using a spoiled gradient echo sequence, and all images were collected with respiratory triggering. The echo times, TE, were 2.86 and 4.64 ms for in/out phase images respectively. The in-plane resolution was 313 x 313 μm, repetition time TR = 250 ms, number of excitations NEX = 2, and flip angle FA = 45^0. For determination of T_2 maps, multi-spin-echo images were collected with TE spaced uniformly every 5 ms from 5 to 50 ms, and then every 20 ms from 50 to 130 ms, with TR=3300 ms. The first echo time at TE = 5 ms was not used in T_2 fitting due to the formation of indirect echoes [173]. Other parameters for both T_2 and IP/OP images were FOV = 80×80 mm, slice thickness = 1.5 mm, and number of slices = 24.

6.3.3 *Data Analysis*

Pixel-wise mono- and bi-exponential fitting of multi-spin-echo data was accomplished with MATLAB software (MathWorks, Natick, MA, USA). Fits to the mono-exponential decay function were compared to bi-exponential decay function fits,

$$S = S_0\,(f.e^{-TE/T\,2_S} + (1-f).e^{-TE/T\,2_L}) + C \tag{5}$$

Here S is the observed signal, TE is the echo time, S_0 is the bulk signal intensity, and T_{2S} and T_{2L} are the spin-spin relaxation times from fast and slow decaying components of the spin pool. Their proportions can be estimated from f, which is the fractional contribution of T_{2S} to S_0 and referred to as ρ_S. Accordingly, $1-f$ is the fractional contribution from long decaying spins and denoted ρ_L. T_2 obtained from fits to the mono-exponential function is referred to as T_{2M}. Pixel-wise percent fat fraction maps, FF, were generated from Dixon images neglecting phase errors [46, 198].

In CDAA fed animals, where nodular lesions were apparent, mean FF and T_2 times were extracted from within that region of interest (ROI). Suspicious lesions were assumed when there was a correspondence between hyper-intense IP/OP and hypo-intense T_2 images. Care was taken to choose ROI's from similar locations across different time points and this was done manually and retrospectively. The nodular boundary (~1-2 pixels) was excluded to avoid contamination from the surrounding liver tissue signal. Focal lesions were only considered for statistical analysis if their volumes were greater than 0.60 mm^3 and were observed in both IP/OP and T_2 images. Focal lesions less than 0.60 mm^3 were not always clearly defined in the FF and T_2 parameter images as well as in all time points. Whole liver characteristics and changes with time were also investigated. The liver was manually segmented from each slice, blood vessels removed using an automatic threshold algorithm as implemented in MIPAV software and statistics determined from these images. To analyze whether mono- or bi-exponential model were more appropriate the correlation coefficient r^2, F test [221] and Akaike information criterion (AIC) [222] were used to inform on model appropriateness.

Statistical calculations were performed using SigmaPlot software (version 11, Systat Software Inc., CA, USA). Estimates of parameters extracted from ROI's are reported as mean +/− standard deviation at each time point. The independent student's *t* test was used to compare FF and T_2 between control and CDAA groups at each time point. Analysis of Variance (ANOVA) was used to evaluate changes in FF and T_2 over time with $p < 0.05$ considered statistically significant. Correlation between mean FF and T_2 parameters was evaluated using Pearson's correlation coefficient and considered to be statistically significant when $p < 0.05$.

6.3.4 Histology

Animals were sacrificed after the final MRI session at 57 weeks. The liver was removed, separated into the seven lobes, drop fixed in RCL2 solution (3:5 v/v RCL2/Ethanol) [168] and stored at 4°C until prepared for histology. The tissues were embedded in paraffin wax. Sections (5 μm) were stained with haematoxylin and eosin (H&E) and examined by a veterinary pathologist. Histological lesions were classified according to Thoolen *et al.* [169].

Numerous patholgies were found with two common to all tissue analysed; microvesicular fatty change if hepatocytes were filled with numerous small lipid vacuoles and macrovesicular fatty change with hepatocytes containing a large single vacuole. These photomicrographs were further compared with the corresponding MR images.

6.4 Results

The CDAA model used in our studies is based on the knowledge that combined deficiencies of choline and methionine ultimately lead to HCC, but does so via the onset of steatosis. Body weights and liver volumes for CDAA and control animals are presented in figure 6-1. A previous study of the CDAA animal model [223] to 12 weeks reported similar weight trends as ours (316 ±13 g compared to 294.12 ±17 g in our study). Compared to controls, CDAA animals had a significantly higher body weight (500 ±15 g) by the end of the study (Figure. 6-1a). In addition, the liver volume of the CDAA group was significantly larger ($P < 0.05$) compared to controls and this was observed early, continuing through the course of the study (figure. 6-1b). This was not unexpected and consistent with previous studies.

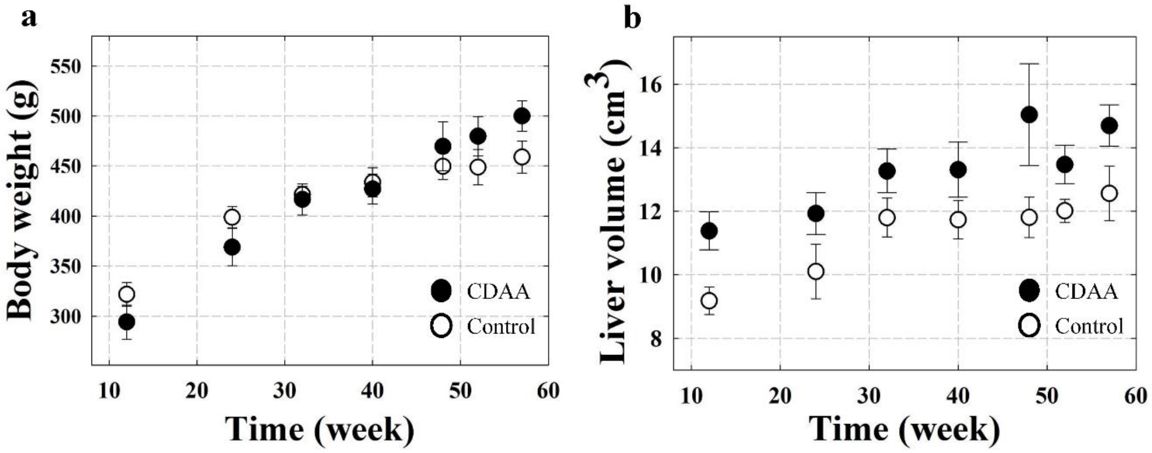

Figure 6-1*:* The average body weight (a) and liver volume size (b) in control group versus CDAA group at each time point from week 12 to week 57. n=6 animals per group, error bars are standard deviation.

There are several qualitative features immediately apparent from the Dixon MR images. In control animals, IP and OP images are visually similar since lipid content is low. OP liver images from CDAA animals appear darker without any further image processing. T_2–

weighted images without fat suppression show a higher signal intensity in CDAA liver compared to controls. The increased T_2 signal and signal cancelation in OP images are indicative of diffuse fat distribution. In this study, these characteristics were observed from the first imaging time point at 12 weeks. Histological examination (H&E) at the end of the MR study revealed diffuse micro- and macro-vesicular fatty character among other pathologies in the CDAA group, while only multifocal and occasional aggregated hepatocytes with intracytoplasmic lipid droplets were observed in controls as shown in the bottom panel of figure. 6-2.

Also in figure 6-2*,* IP, OP, water only, fat only, and T_2 weighted (at TE = 20 ms) images of control and CDAA rat livers at the week 57 time-point are shown. Water and fat images can be retrieved from IP/OP imaging where "Water Only" = (IP+OP)/2 and "Fat only" = (IP-OP)/2, respectively [218]. From figure 6-2, it is noted that the maximum integer value of the calculated image (7000) is less than the water only value (22000). Thus percent fat fractions of our cohort are less than 50%. We do not expect liver fat content to be any greater in the clinical case but there does not exist a standard correlating clinical measurements with MRI-determined FF.

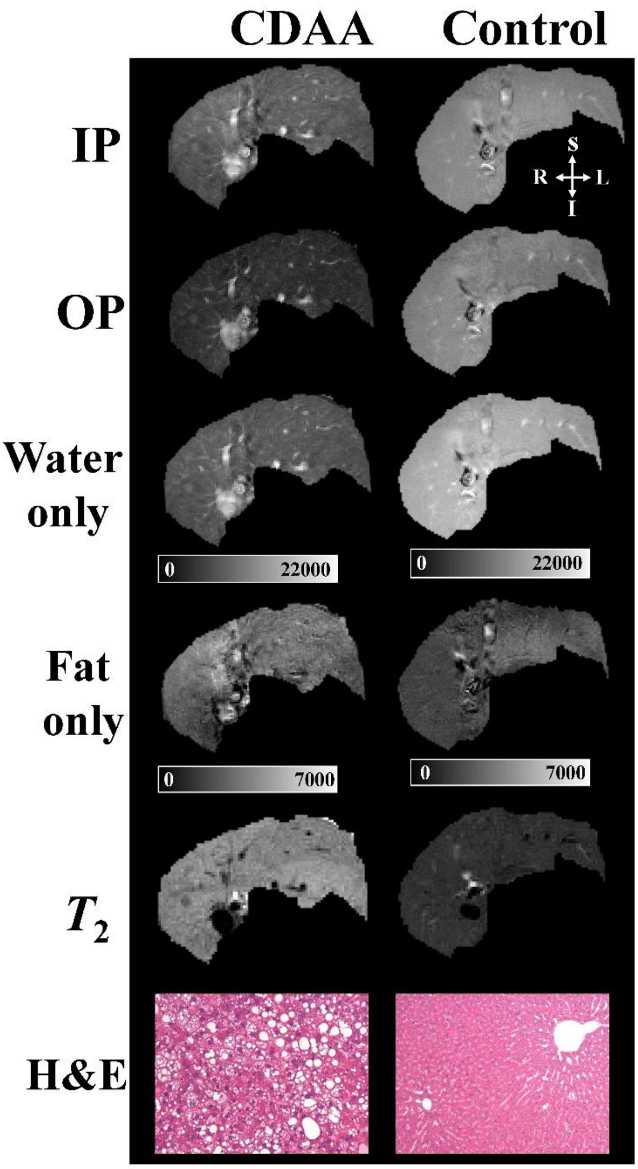

Figure 6-2: IP, OP, water only, fat only, T_2 and H&E histology images of control and CDAA rat liver at week 57. CDAA liver shows lower signal intensity in the OP image compared to IP image, while almost equal signal intensity as the control indicating that fat content is very low. The T_2 images show a higher signal intensity in CDAA liver compared to control. The grey scales indicate the signal intensity estimations of water and fat in the two animals. Histologic H&E staining of control and CDAA liver section shows that CDAA liver (200x) were characterised by a prominent accumulation of lipid droplets (microvesicular and macrovesicular fatty change) compared to control (100x). S(superior) ≡ dorsal; I(inferior) ≡ ventral; R, right; L, left.

Histological examination of CDAA livers at the end of the MR study revealed two types of nodular lesions corresponding to the nodules detected by MRI: regenerative hyperplastic nodules and hepatocellular adenoma. Regenerative hyperplasia was characterised by focal or multifocal accumulation of elevated number of hepatocytes with a normal lobular architecture, compression of the surrounding liver parenchyma and occasional mild fibrosis. Hepatocellular adenoma (HCA) was observed as a single nodule consisting of increased number of hepatocytes with loss of the normal lobular architecture and sharp demarcation from the surrounding parenchyma.

Eleven nodules from the six CDAA animals were selected from week 57 MR images and were retrospectively examined from week 24 to 57. These were histologically confirmed to be regenerative hyperplastic nodules.

The 11 regenerative nodules were characterised by hyper-intense IP/OP signal and hypo-intense signal in T_2 weighted images from week 24 as shown in figure 6-3.

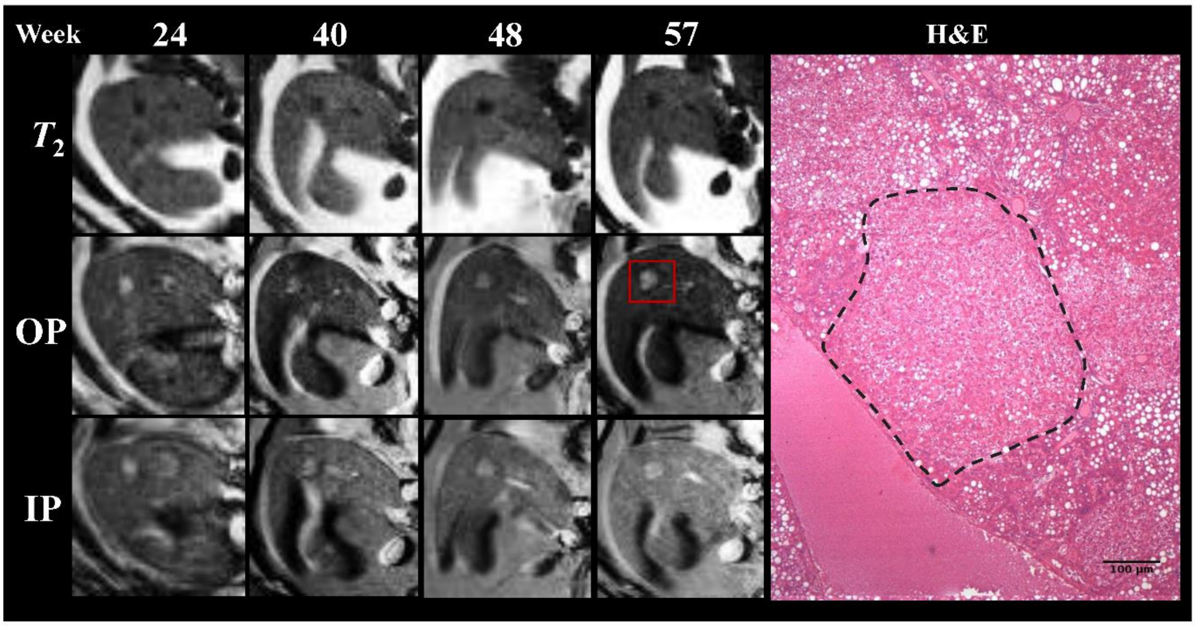

Figure 6-3: MRI images and histology of a regenerative hyperplastic nodule in CDAA rat liver. The MR axial section shows the presence of a hyperplastic nodular lesion in the liver lobe (red square in OP image) with hypo-intense signal in T_2 image (TE=20 ms) and hyper-intense signal in IP/OP images. In the histological H&E stain shown on the right, taken from the red square, the nodule is indicated by the dotted black ROI.

Mono and bi-exponential functions provided excellent fits to T_2 data with average $r^2 >$

0.95 irrespective of tissue type (i.e. fatty, nodular lesion or normal liver parenchyma). AIC analysis indicated, however, that the bi-exponential function is the preferred model at all-time points for CDAA group animals irrespective of pathology. The F test confirmed the AIC analysis at week 12, but indicated that mono-exponential fitting was better from week 24 to 57 in both whole liver and nodular lesions in the CDAA group. Figure 6-4 shows the percentage of pixels where bi-exponential fitting is preferred by both AIC and F tests. Note that for both AIC and F test analyses of the CDAA group there is a significant reduction in the number of pixels best fit to a bi-exponential function over time, possibly because of the onset of mild fibrosis. Control animals also show a similar trend (solid blue circles in figure 6-4), the percent of pixels fit is much lower and there is no significant difference between the last time-point at 57 weeks compared with 12 weeks.

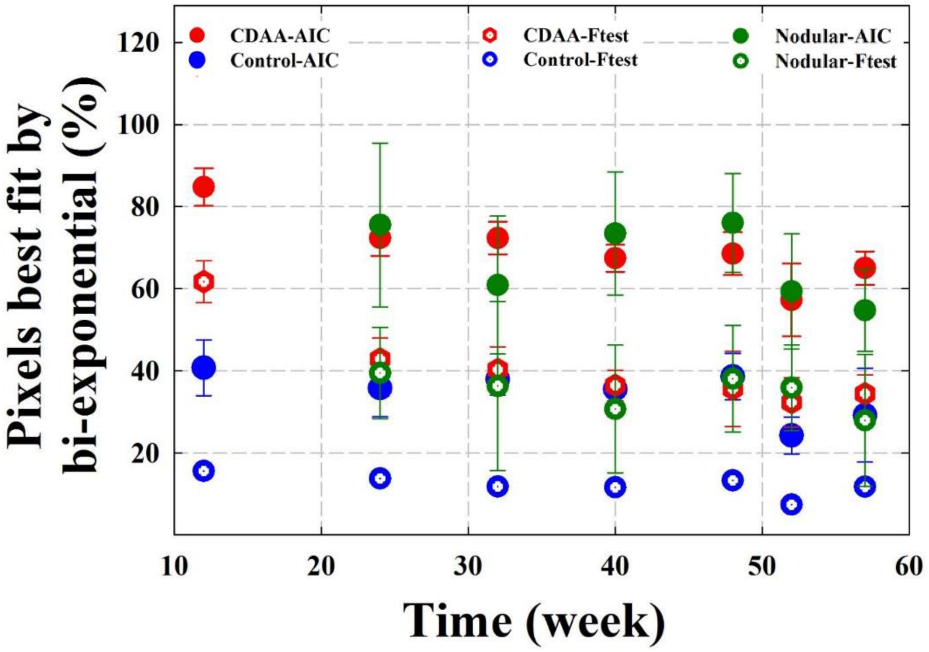

Figure 6-4: The average percentage of pixels for which the bi-exponential function is preferred using AIC and F test in whole liver measurement of control and CDAA animals, and nodular lesions over all time-points.

Maps of mono/bi-exponential T_2 components compared with FF from whole liver are shown in figure 6-5 for a control and CDAA animals at the 24 week time point.

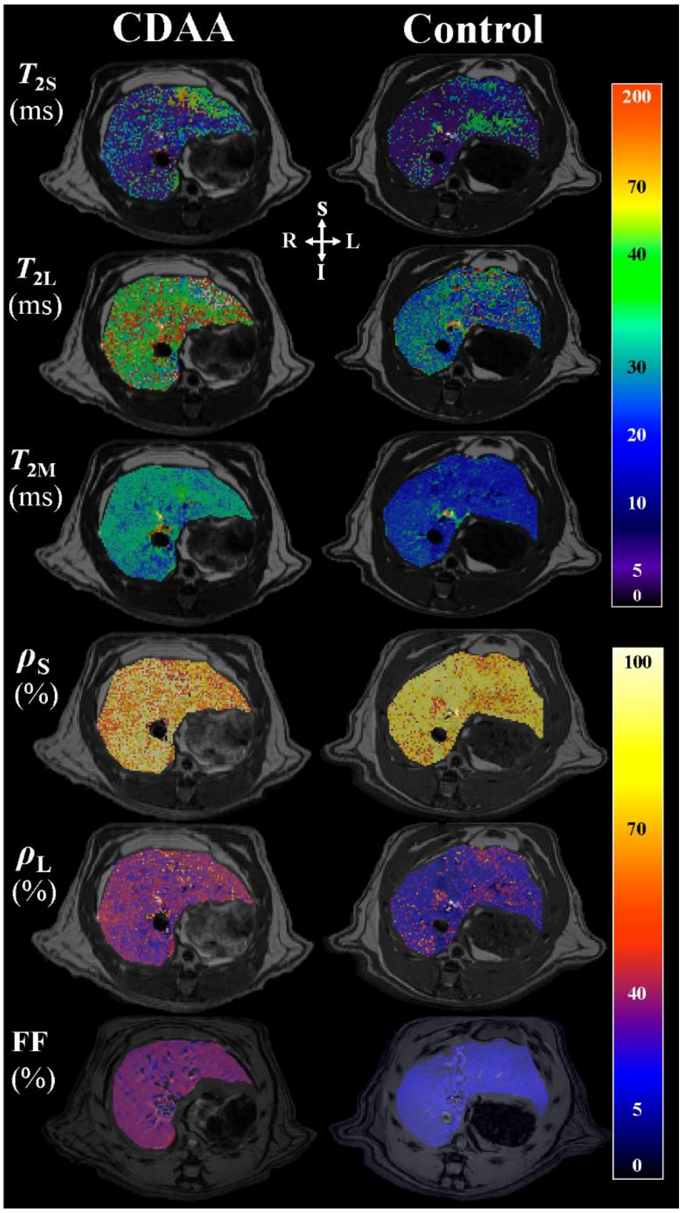

Figure 6-5: Mono and bi-exponential components of T_2 and FF analysis of representative control and CDAA animals at week 24 after diet administration. T_{2S}: short component, ρ_S: signal contribution from T_{2S}, T_{2L} long component of T_2 map; ρ_L signal contribution from T_{2L}, T_{2M} is mono-exponentially calculated T_2, FF is fat fraction measured using the Dixon technique. Individual T_2 maps are overlaid on T_2 images and FF on OP images. T_{2S}, T_{2L}, and T_{2M} are measured in milliseconds (ms); ρ_L, ρ_S and FF are expressed as percentages (%). S (superior), dorsal; I (inferior), ventral; R, right; L, left

Statistically, with time, whole liver FF and T_2 values show that the mean FF, T_{2M} and T_{2L} were significantly higher ($P < 0.001$) in CDAA animals compared to controls at each measurement point (figure 6-6a). ρ_S was significantly lower, and ρ_L higher, ($P < 0.05$) up to week 48 in the CDAA group compared to controls (figure 6-6b).

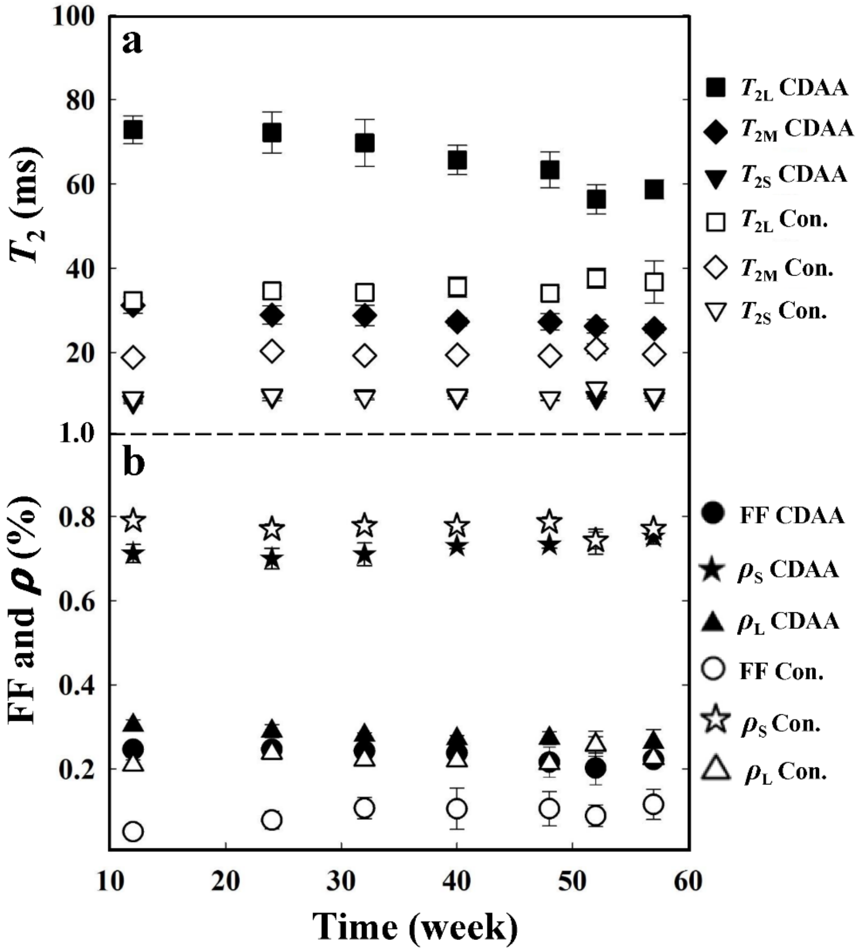

Figure 6-6: Box plot for the mean whole liver values of T_{2M}, T_{2L}, and T_{2S} (a); and for percentages of ρ_S, ρ_L , and FF (b) in CDAA and control groups from week 12 to week 57.

In CDAA animals, FF, T_{2L}, and T_{2M} declined significantly ($P<0.001$, $P<0.001$, $P<0.05$; respectively) over the diet period, The T_{2S} remained mostly constant over time. The fractional density, ρ_L, decreased with time, whereas ρ_S increased. The rates of change of FF and ρ_L per week were comparable in CDAA group: -0.0893% per week and -0.0922% per week, with correlation coefficient (r) = 0.83 and 0.96, respectively. This suggests that in diffuse fatty liver, ~ 0.1% decrease in both FF and ρ_L occurs per week. For controls, the rates of change for FF and ρ_L were not comparable (FF change rate =0.1%, r=0.79, $P < 0.05$ versus ρ_L=0.03%, r=0.34, $P < 0.05$). The change of mean FF and ρ_L values over time in CDAA and control groups is summarized in figure 6-7.

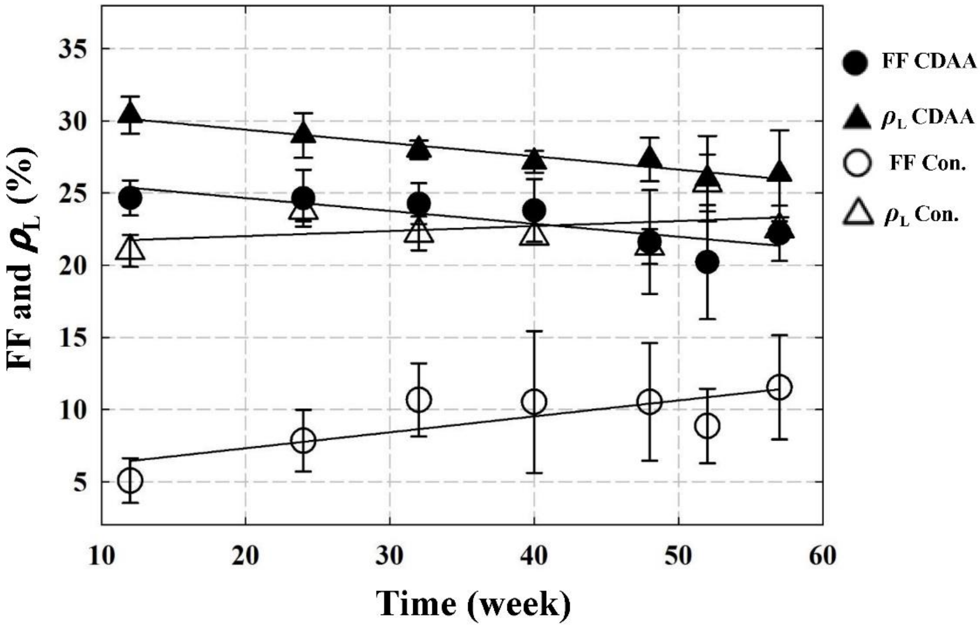

Figure 6-7: Changes in the mean whole liver FF and ρ_L in CDAA and control groups from week 12 to week 57. In CDAA animals, the FF and ρ_L declined significantly and the rate of change per week for both were comparable during the diet period (-0.0893 % and -0.0922 %, respectively) during the diet period. For controls, the rate of change for FF and ρ_L were not comparable (0.1% versus 0.03%, respectively).

To determine the correlation between FF and T_2 parameters, the average T_{2L}, T_{2M}, ρ_L, and ρ_S values of the whole liver were plotted against the respective FF in the CDAA group over time (figure 6-8). The mean FF was positively correlated with T_{2L} ($P < 0.01$; $r = 0.931$), ρ_L ($P < 0.05$; $r = 0.806$), and T_{2M} ($P < 0.05$; $r = 0.77$) over time. A negative correlation was observed between FF with ρ_S ($P < 0.05$; $r = -0.79$) and no correlation was seen between FF and T_{2S}. No correlation found between FF and T_2 parameters in the control group.

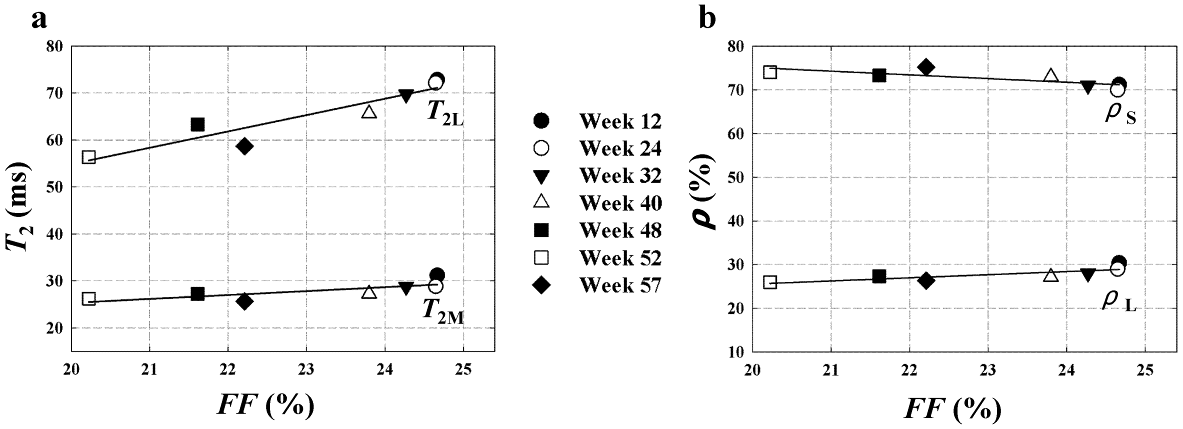

Figure 6-8*:* Scatterplots between the whole mean ρ_L and T_{2M} with FF (a); and ρ_L and ρ_S with FF (b) in CDAA group over time reveals a strong correlation.

A positive correlation was also found between FF and AIC ($P < 0.02$; $r = 0.81$). This strong correlation and the decreased preference for bi-exponential T_2 signal over time in whole diffuse fatty liver indicates a decrease in the level of fat droplets during hepatocarcinogenesis. It is possible that the fibrosis found in the histology in CDAA animals is the pathological factor resulting in reduced FF during the diet period.

Nodular quantitative MR (nodule versus surrounding fatty liver tissue in CDAA group)

Figure 6-9 shows an example of the T_2 and FF parametric colour maps of nodular lesions versus diffuse fatty liver background in the CDAA group. At week 24, the mean area size of the 11 nodules was 1.6 mm^3 (range 0.68 – 3.2 mm^3). Over the MRI study period, these nodules had significantly increased ($P < 0.01$) with growth rate of 0.05 mm^3 per week, reaching the maximum size at week 57 with an average of 3.2 mm^3 (range 1.83 - 4.98 mm^3).

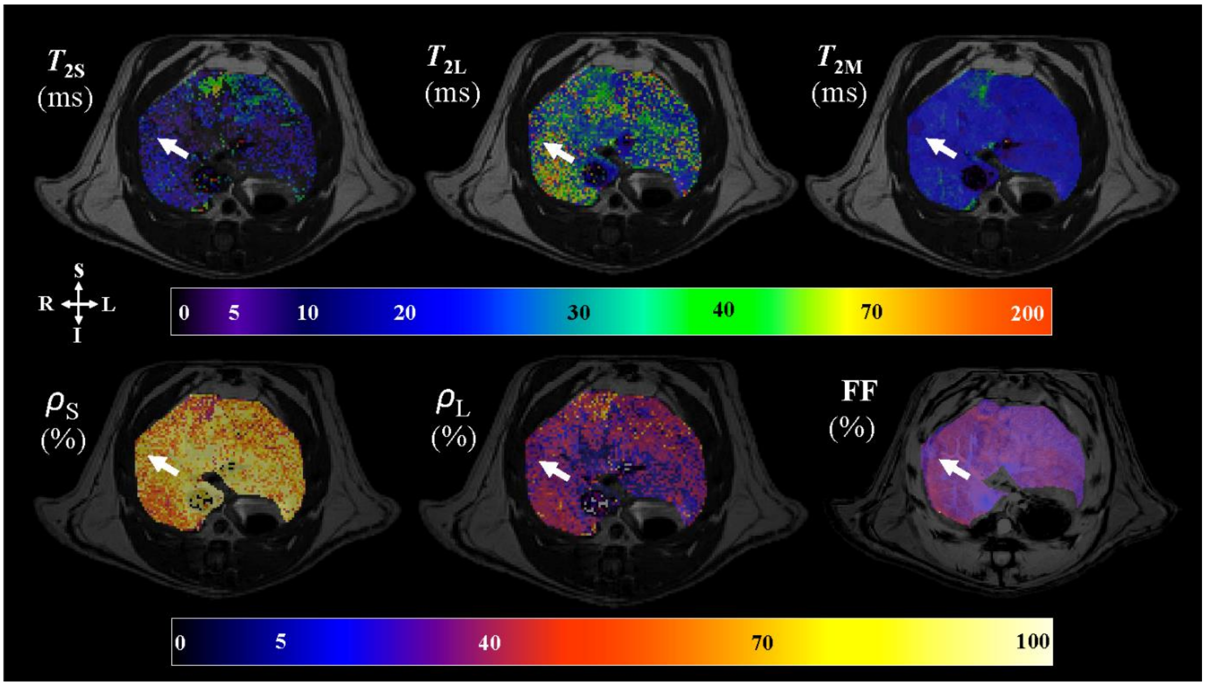

Figure 6-9: An example of the axial T_2 maps (overlaid on T_2 images) and FF (overlaid on OP images) at week 24 showing a focal nodular lesion (white arrows) on a diffuse fatty liver background in CDAA liver. T_{2S}, T_{2L}, and T_{2M} are measured in millisecond (ms); ρ_L, ρ_S, and FF measured in percentage (%). Compared to the surrounding liver tissue, the nodular FF and T_{2M} maps show decreased fat fraction and T_2 value, respectively. The T_{2L}, T_{2S}, ρ_S and ρ_L maps show slightly lower values with surrounding tissue. S (superior), dorsal; I (inferior), ventral; R, right; L, left

The results from descriptive statistics for the nodular lesion versus surrounding diffuse fatty (descriptive statistics presented in Table 6-1) show that the mean FF and T_{2M} of nodules were significantly lower at all time-points (except week 40 for FF). Nodular T_{2L}, ρ_S and ρ_L were significantly lower at certain time-points. No significant difference was seen in T_{2S}. Note that the standard deviation given in table 6-1 shows a broad distribution of MR parameters among nodules compared to a tighter distribution across whole liver in CDAA animals, indicating that these lesions are heterogeneous. Repeated ANOVA measures showed no significant changes in FF and T_2 values ($P > 0.05$) over time, indicating that these values remained relatively constant in nodules during the diet period. No correlation was found between FF and T_2 parameters, suggesting that FF does not have a strong influence on T_2 parameters in nodules.

Table 6-1. Descriptive statistics for nodular lesions versus surrounding diffuse fatty liver.

Week	Group	FF (%)	±SD	*P* value	T_{2M} (ms)	±SD	*P* value	T_{2L} (ms)	±SD	*P* value	T_{2S} (ms)	±SD	*P* value	ρ_L (%)	±SD	*P* value	ρ_S (%)	±SD	*P* value
24	***Nodule***	14.74	6.09	<0.001	23.57	5.00	0.03	62.05	14.76	0.10	9.10	3.49	>0.05	31.18	8.41	>0.05	68.81	8.41	>0.05
	S.tissue	24.65	1.96		28.87	2.17		72.17	4.85		9.50	0.97		29.00	1.55		70.00	2.45	
32	***Nodule***	17.77	2.78	<0.001	22.25	4.66	0.01	48.37	12.85	0.00	9.85	4.76	>0.05	27.64	10.62	>0.05	72.36	10.62	>0.05
	S.tissue	24.27	1.42		28.77	2.40		69.71	5.56		9.62	0.56		28.00	0.63		71.00	2.68	
40	***Nodule***	18.72	7.08	0.30	19.51	3.45	<0.001	43.56	16.97	0.01	9.04	3.63	>0.05	23.09	6.56	<0.05	76.90	6.56	<0.05
	S.tissue	23.80	2.18		27.26	0.98		65.63	3.46		9.30	0.39		27.17	0.75		73.00	0.63	
48	***Nodule***	16.39	4.18	0.02	20.28	2.55	<0.001	46.97	13.78	0.01	7.58	3.07	>0.05	19.45	6.07	<0.05	80.54	6.07	<0.05
	S.tissue	21.61	3.59		27.24	1.94		63.30	4.27		9.20	0.50		27.33	1.51		73.30	0.82	
52	***Nodule***	14.36	4.11	0.01	17.04	2.06	<0.001	52.64	31.50	0.70	7.60	3.26	>0.05	17.00	6.65	<0.05	83.00	6.64	<0.05
	S.tissue	20.22	3.96		26.22	1.61		56.32	3.48		9.24	0.21		26.00	2.97		74.00	2.97	
57	***Control***	18.12	3.79	0.03	19.93	1.96	<0.001	56.07	24.80	0.80	8.77	2.35	>0.05	20.36	7.15	<0.05	79.63	7.14	<0.05
	S.tissue	22.21	1.91		25.66	1.02		58.68	2.26		9.02	0.63		26.33	3.01		75.20	1.72	

CDAA, choline deficient L-amino acid; $T_{2M,}$ T_2 mono-exponential; T_{2L}, long T_2 component; T_{2S}, short T_2 component; ρ_S, fraction of the short compartment signal; ρ_L fraction of the long compartment signal; SD, standard deviation.

Gross appearance

The photographs in figure 6-10a&b demonstrates the CDAA liver as diffusely pale and enlarged compared to control.

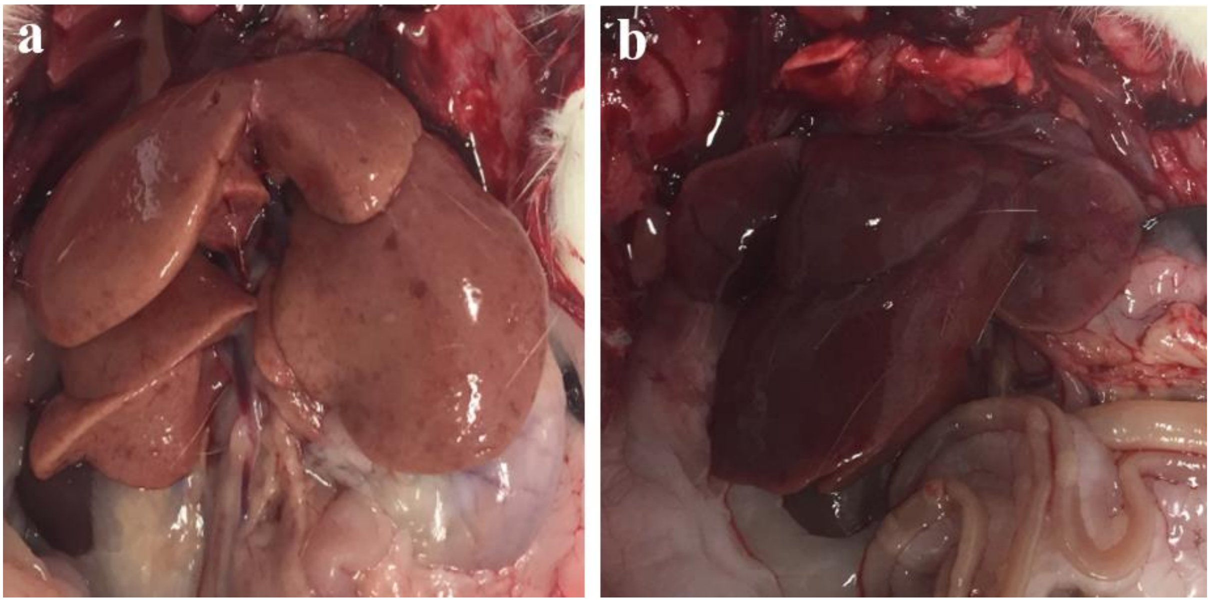

Figure 6-10: Gross appearance of a CDAA rat (A) and control rat (B). The CDAA liver is slightly enlarged and has a diffusely pale appearance.

Other histological findings

Histological assessment of the livers from CDAA animals revealed a number of features that could not be detected by MRI measures, mainly due to the difference in spatial scales available in each technique, and are depicted in Figure 6-11. According to Thoolen *et al*. [169] classification, these lesions are:

- Focal fibrosis: the presence of connective tissue and act as a reaction to acute or prolonged hepatotoxicity,
- Bile duct hyperplasia: a spontaneous change in portal areas and defined as increased number of small bile ducts arising in portal region,
- Eosinophilic foci (EOS): is polygonal enlarged hepatocytes with increased acidophilic staining compared with the surrounding normal liver,
- Oval cell hyperplasia: arises from terminal ductule epithelial cells and can be observed following severe hepatotoxic injury and treatment with hepatocarcinogens,

- Clear cell foci: consist of normal or enlarged groups of cells with prominent cell membranes and distinct cytoplasmic clear spaces surrounding a densely stained centrally located nucleus.

These focal lesions in rat experiment models occur in association with a high incidence of hepatocellular carcinoma and thus considered as an indicative of progression towards HCC [169, 224].

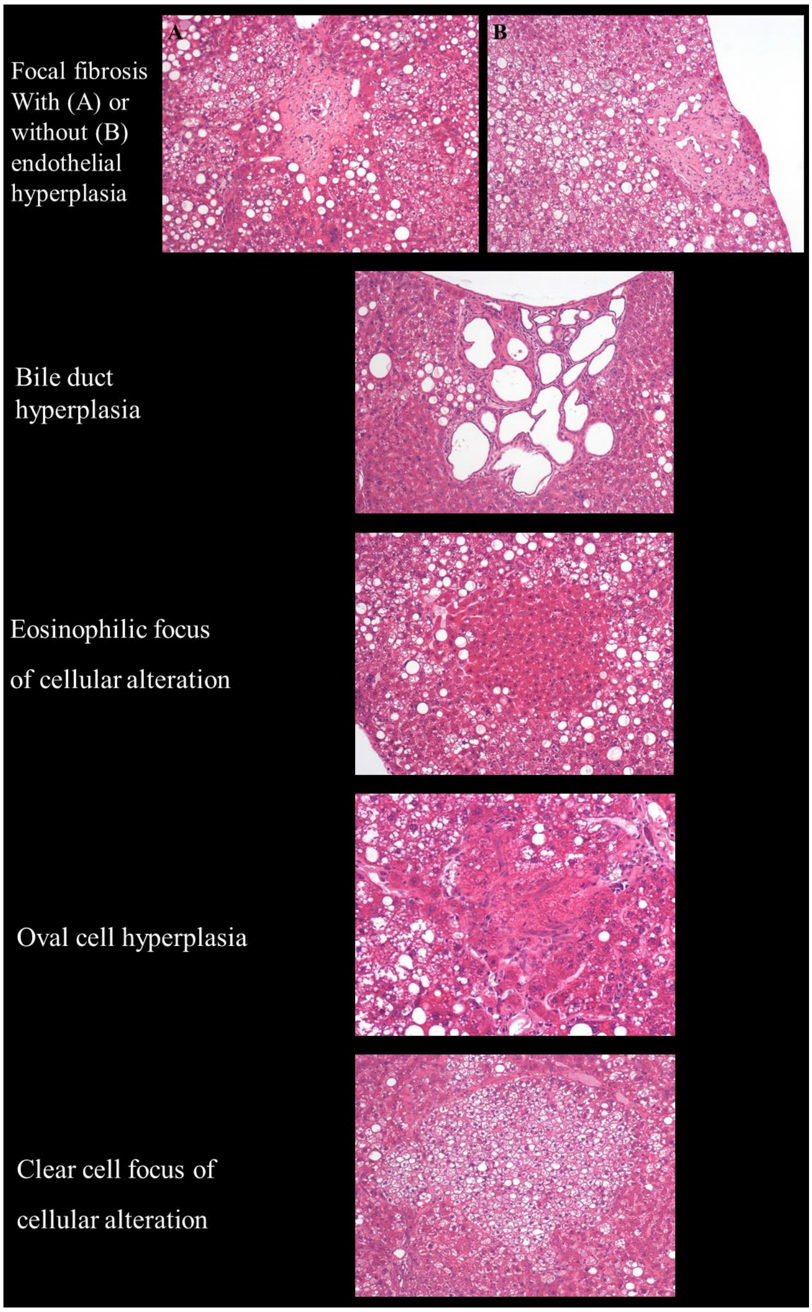

Figure 6-11: The histological lesions in livers of CDAA animals not detected by MRI.

Comparison of in-vivo and ex-vivo imaging with histology

Figure 6-12 presents MRI *in-vivo* and *ex-vivo* images in a CDAA liver of three regenerative nodules in two different liver lobes with accompanying H&E tissue stains obtained from liver approximately in the same position as the MR image slices.

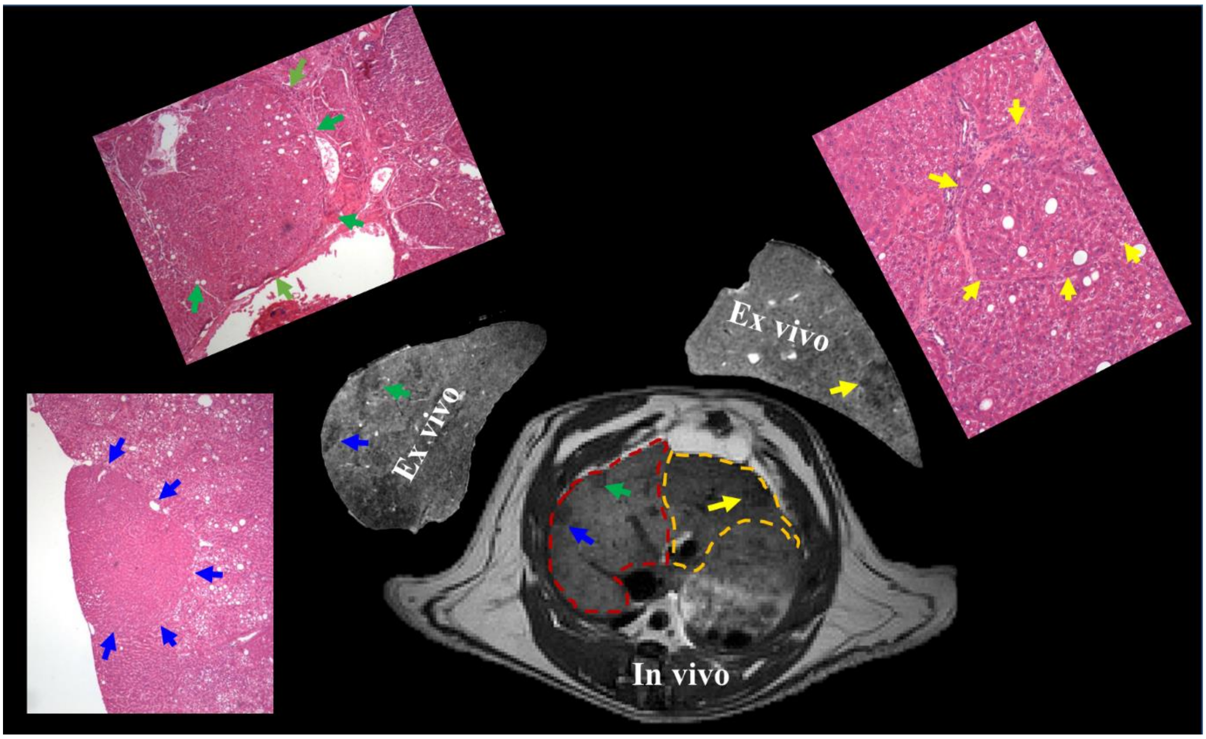

Figure 6-12*:* MRI in-/ex- vivo and histology (H&E stain) representative of three regenerative hyperplastic nodules in a CDAA rat. Red and yellow dashed lines in the *in vivo* MR image indicate two separate liver lobes. These three nodules (blue, green and yellow arrows) were identified on *in-/ex- vivo* images and histology.

Liver lobe appearance

The CDAA livers were markedly enlarged, non-smooth, and with irregularities compared to the control animals at all-time points. Qualitatively, these changes became more severe with time. Figure 6-13 shows T_2 weighted images of control and CDAA liver lobes at the week 48 time point. The four lobes (right lateral, left lateral, median, and caudate lobes) were enlarged in CDAA liver compared to the control, most obviously in the caudate lobe (CL).

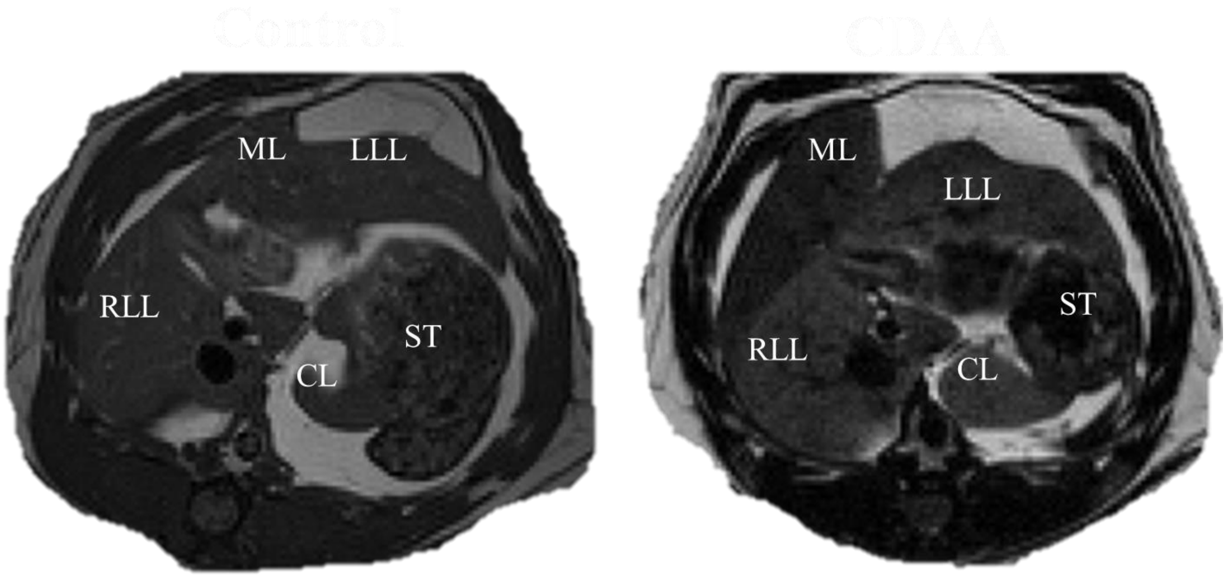

Figure 6-13: Axial T_2 images obtained from a control (left) and CDAA (right) rat livers at week 48 time point. (ML: median lobe; LLL: left lateral lobe; RLL; right lateral lobe; CL: caudate lobe; ST: stomach).

6.5 Discussion

Here we used quantitative *in vivo* MRI at 9.4T to study fatty infiltration and nodular formation in the liver of CDAA-induced rat HCC model over time. We utilized the two-point Dixon method and T_2 mono/bi-exponential decay to measure FF and T_2 parameters, respectively, of both the whole liver and nodules in CDAA animals compared to controls. The correlations between FF with T_2 parameters were evaluated. Such data may be of importance for potential future use in a clinical setting to distinguish nodular lesions from fatty liver background and to allow a risk assessment in patients with fatty liver disease. The present results clearly showed that T_2 parameters including T_{2M}, T_{2L}, ρ_L and ρ_S are affected by FF in the whole fatty liver but not in nodules.

The evaluation of diffuse fat lesions using two-point Dixon imaging showed a signal drop in OP images and homogenous signal in IP images in the whole CDAA liver, compared to controls. T_2 weighted imaging showed the fat lesions as a diffuse hyper-signal in CDAA liver, compared to controls. The increased signal in the CDAA group is due to the longer T_2 relaxation time of fat compared to water [186, 225, 226]. Nodular lesions were easily distinguishable from the surrounding liver tissue at 24 weeks, appearing as hypo-intense signal on T_2 images and hyper-intense signal on both IP and OP images.

Pixel-wise T_2 mapping using mono- and bi-exponential models substantially showed a high precision (high r^2) for the fit, suggesting that both mono- and bi-component analyses are valid. In this study, we statistically compared the mono- and bi-exponential model***s*** of T_2 signal decay in both whole diffuse fatty liver and nodular lesions. AIC showed that diffuse fatty liver and nodules at all-time points were better characterized by a bi-exponential function, while less than 45 percent of pixels were better defined by a bi-exponential model in control livers. We observed that when the FF is higher than 14%, the preference for bi-exponential fit in more than half the pixels in diffuse fatty liver is strongly affected by the presence of fat droplets. In contrast, results using the F test were only consistent with the AIC in week 12, and from week 24 preferred the mono-exponential function. A possible explanation is that the F test tends to choose the simpler model in comparison to AIC even when the complex model is correct [227]. These results demonstrate that AIC is more effective in characterising fatty liver and focal lesions compared to the F test for the existence of two components.

The dependence of T_2 may be attributed to histological changes such as in nuclear to cytoplasm ratio, cell enlargement, and alteration in the cellular microenvironment by the intracellular fat droplets [228]. As the CDAA diet model in the rat is known to induce diffuse fatty liver disease before development of pathological nodules, we hypothesized that FF has a predictable relationship with liver T_2 relaxation time during hepatocarcinogensis. With decreasing FF in the CDAA group during the diet period, the signal fractional contribution of the long T_2 component (ρ_L) decreased, with a concomitant increase in the contribution (ρ_S) of the short T_2 component. The rate of change for FF and ρ_L per week was similar (~ 0.1%). In addition to the decrease in ρ_L, the T_2 long (T_{2L}) values tended to decrease with decreasing FF. Given that the decrease of ρ_L and T_{2L} values with decreased FF, it may be intuitive to propose that the T_{2L} component reflects the fat compartment and T_{2S} reflects liver water in CDAA group. This is consistent with a previous spectroscopy study that found T_{2L}, but not T_{2S}, was significantly correlated with the percentage of fat within cirrhotic liver biopsy specimens [229]. However, the fractional contributions of the ρ_L and ρ_S in the control livers do not support such an interpretation in CDAA livers as there was a poor correlation between FF with T_{2L}, ρ_L and ρ_S. Therefore, we suggest that the two components observed in the control animals could correspond to intra- and extracellular water compartments rather than to fat and liver water components, as is typically described for T_2 measurements *in vivo*.

The presence of fibrosis in CDAA livers, may explain the decrease in ρ_L during the progression of the disease. T_2 has previously been used to characterize liver fibrosis and increased T_2 values were observed [205] consistent with our observations for T_{2L}. The T_{2M} value derived with the mono-exponential model showed significantly higher values in CDAA compared to controls at each time point. However, the T_{2M} was decreased over time and showed a significant correlation with FF. Given that FF was strongly correlated with T_{2L} component and poorly with T_{2S} component, our results indicate that the decrease in T_{2M} values with decreased FF over time is dominated by the decrease in the ρ_L, with a lesser contribution from ρ_S.

For nodular evaluation, our study showed that a lesion of less than 1 mm^3 was easily distinguishable from the fatty liver background by *in vivo* MRI, even without contrast media, due to their different T_2 and characteristic shape. The increase in mean nodular size over time in the CDAA group is an indicator for nodular development in cancer and potentially an important tool for monitoring lesion response to therapy [230].

The accumulation of fat on human tumor xenografts and animal nodular tumor models has been reported in spectroscopic studies, indicating the potential to use MR parameters as diagnostic markers to evaluate nodules [29, 231-233]. We showed that fat droplets can be quantified within nodules even when not detected visually on conventional *in vivo* MR images. Nodular signal T_2 was accurately characterised by both mono and bi-exponential decay in all 11 lesions detected in CDAA animals *in vivo.* The main MR quantitative findings of nodules were that (i) FF and T_{2M} were significantly lower compared to the surrounding fatty liver tissue at all-time points (except week 40 for FF), and (ii) no correlation was shown between FF and T_2 parameters, and (iii) T_{2L}, ρ_L, and ρ_S were significant only at certain time points. There was no correlation between FF and T_2 parameters in nodules over time, suggesting that nodular T_2 values may be affected by other molecular changes such as inflammation, perfusion changes, and edema [234]. Additional studies are needed to determine the physiological origin of T_2 parameters in these liver nodules.

NAFLD ranges from simple liver steatosis to steatohepatitis (NASH). NASH is a serious condition that can lead to fibrosis and cirrhotic stages, general risk factors for HCC [35]. There is insufficient MRI data to describe longitudinally the presence of HCC-associated NAFLD during hepatpocarcinogensis with histological confirmation at each stage. For example, we expect that fibrosis during hepatpocarcinogensis would translate to a continuous reduction in FF and reflected in decreasing T_2 values. In this study however, we only performed histology following the last time-point. We propose that using multiple T_2 components and FF together with histological analysis at each time point would provide a more detailed characterisation of the pathological microenvironmental changes within lesions as well as providing cutoff points to allow stages to be identified and classified.

In conclusion, this study demonstrated that it is possible to create statistical maps of pathological liver that combine FF and T_2 parametric data, indicating that combination of multi-parametric MR is more powerful than any one technique alone. Our results demonstrate that T_{2M} in the whole CDAA liver is significantly correlated with FF during hepatocarcinogenesis. In addition, both the T_2 long value and its fraction significantly correlated and decreased with decreasing FF measured by Dixon method. Supporting the relationship between the T_{2L} and fat fraction in the liver. The poor correlation between FF with T_2 parameters found in nodules over time; suggests that nodular T_2 values in longitudinal studies were less influenced by FF, and may more be likely affected by other molecular alterations.

Chapter 7 : Overall discussion and conclusion

7.1 Introduction

The ability to track the changes in liver pathology prior to the formation of HCC has potential to significantly inform improvement of clinical management and treatment of progressing liver disease. We used an experimental CDAA-induced hepatocarcinogenesis rat model to apply quantitative fat fraction and mono- and bi-exponential T_2 analysis to progressive liver disease, including hepatic nodular lesion formation. To our knowledge, this is the first quantitative FF and T_2 analysis in *in vivo* animal model studies at 9.4 T for characterizing developing hepatocarcinogenesis. The principle advantage of using high field MRI is to increase signal-to-noise ratio (SNR) and, thus, improve spatial resolution [235].

The evaluation of developing hepatocarcinogensis induced by the CDAA diet in a rat model is an important first step in the development of clinical methods for the measurement of MR detectable biomarkers for accurate HCC staging. Nakae, D., *et al*. reported that the CDAA diet is frequently used for long term studies and histologically presents fatty liver in early stages and fat associated with precancerous lesions after week 12 from continuous CDAA feeding. HCC develops from about 52 weeks on the CDAA diet [57]. Our rats on the CDAA diet displayed fatty infiltration in the whole liver at the first time point (12 weeks). At week 24, the pathological nodules were generated and diagnosed histologically as benign lesions. These benign lesions were associated with a reducing fatty liver and were diagnosed as hyperplastic nodules. HCC nodules were not evident in our study as confirmed by histopathology and *ex vivo* high resolution MR imaging (16.4T). Hyperplastic nodules are known to precede the occurrence of HCC. Thus our study examined the development of fatty liver and hyperplastic nodules leading to fibrosis as a prelude to HCC on the carcinogenesis pathway. The longitudinal T_2 relaxation and FF analysis of developing liver disease may play an important role in enhancing a multi-parametric imaging approach to liver cancer diagnosis, staging and evaluation.

7.2 Qualitative evaluation

Our protocol examined the diffuse fatty infiltration of the liver in rats fed a CDAA diet. Evaluation of liver fat using Dixon imaging showed signal reduction in OP images and homogenous signal in IP images of the CDAA liver compared to controls. T_2 weighted imaging indicated fat accumulation as diffuse hyperintense signal in the CDAA group due to the longer T_2 relaxation times of liver fat relative to water in normal tissue [186, 225, 226]. Liver fat deposition was confirmed histologically with hematoxylin-eosin staining. Nodular lesions developed at around 24 weeks and were easily distinguishable from the surrounding liver tissue appearing as hypo-intense regions in T_2 weighted images and hyper-intense in both IP and OP images. Nodules of size less than 1 mm^2 were easily distinguishable from the fatty liver background by MR, due to the intrinsic image contrast and characteristic nodular shape, without the need for contrast media. The increase in mean nodular size could be tracked over time (from 1.6 mm^2 at week 12 to 3.2 mm^2 at week 57) providing information about the rate of nodular lesion progression. This ability to track nodular development makes it possible to investigate nodular lesion response to therapy [230].

Changes in the liver signal intensity and total liver volume were visually evident and quantified at each time point. MRI provides detailed images of soft tissues in abdominal imaging. However, its application is challenging in delineating liver lobe boundaries due to structural complexity[236] and similar contrast to neighbouring organs. Moreover, high magnetic field MRI of rodents is challenging because of high heart and respiration rates, motion artefacts, and increased magnetic susceptibility effects which reduce image quality. Previous MR studies of rodent liver have indeed shown suboptimal images with no mention of changes in liver lobes that may occur during progression of liver disease [20, 205], particularly liver tumours. Neither of these studies measured the whole liver volume longitudinally. Our MR protocol using respiratory gating in the CDAA-liver rat model provided a good visualization of liver lobular structure changes which may be indicative of sequential changes during hepatocarcinogenesis.

7.3 Quantitative analysis

This study has provided new quantitative parametric data for assessing progressive liver pathology. This includes generating quantitative T_2 and FF maps of the liver. Figure 7-1 is a scatterplot graph showing a visual summary of the outcomes with regard to T_2 and FF of whole liver in controls, CDAA liver tissue, and nodular lesions over time. Overall, the largest change was evident in the decrease in the long T_2 component of the bi-exponential analysis with the decreasing fat fraction with time.

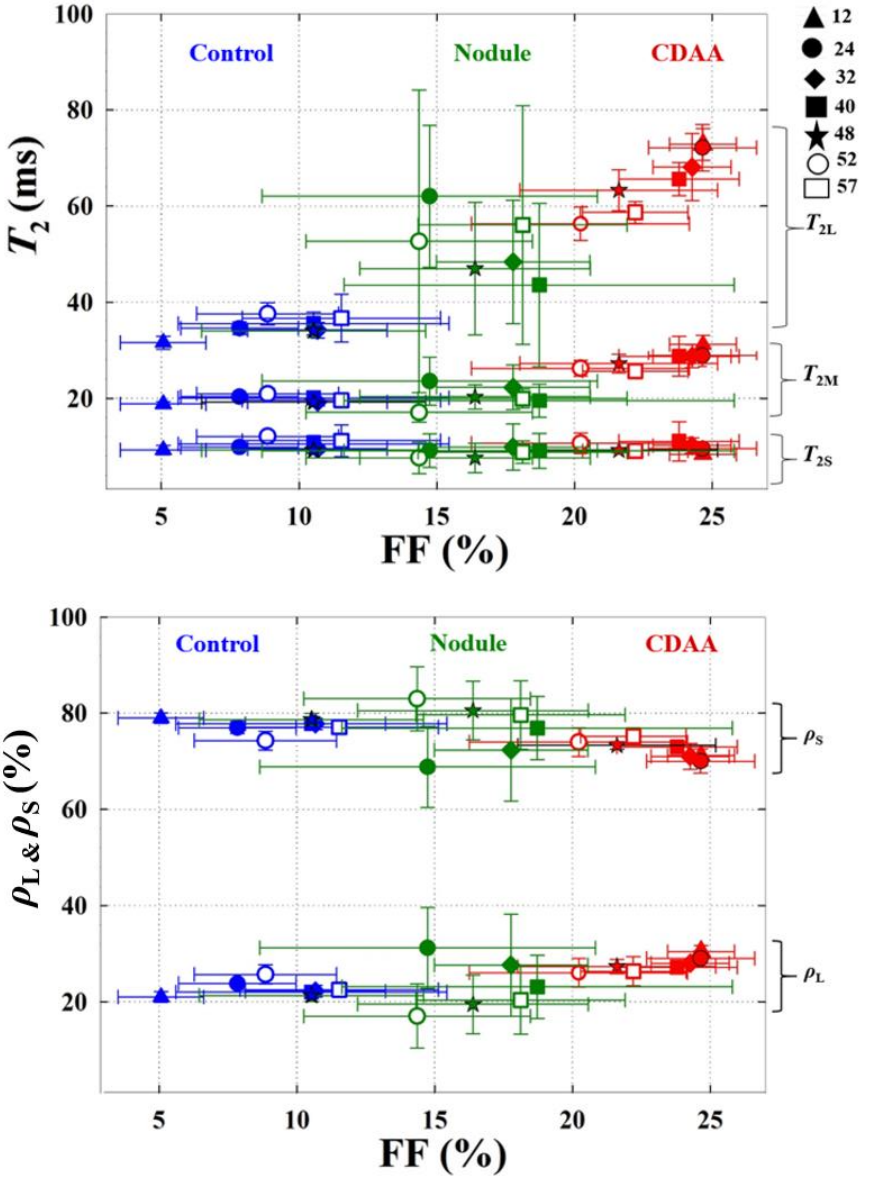

Figure 7-1: Scatterplot graph showing correlation and changes over time of FF with T_2 values (a) and fractional contribution of T_{2S} to S_0 (ρ_S) and fractional contribution from long decaying spins and denoted ρ_L (b) in whole liver control and CDAA, as well as in nodular lesions. Symbols in the upper right refer to weeks after CDAA diet administration

7.3.1 Mono- versus bi-exponential models

Previous T_2 studies describing living tissues containing bi- or multi-exponential components, generally interpreted the separate components as unique water compartments [207-209] usually ascribed to intra- and extracellular water. The T_2 values of fat is longer than that of liver water and will contribute significantly to the tissue T_2 due to the high fat content. For this reason, liver water and fat compartments are the most logical source of short and long T_2 components of the bi-exponential decay curves in fatty liver. This is consistent with the strong positive correlation between T_{2L} and FF (figure 6-8). In contrast to the fatty livers in the CDAA rats, there is little or no fat content in controls in which the liver water is the primary T_2 component.

To statistically assess which model (mono- or bi-exponential) better fit the T_2 data in whole control and CDAA liver, two statistical measures: AIC and F test were utilized in this analysis. The AIC statistic has been used in MRI studies to compare a range of compartment models such as in diffusion data [237, 238] and T_2^* data [239]. To assess the benefit of using a bi-exponential as compared to a mono-exponential model to describe our *in vivo* data, the AIC was taken as an indication of whether the bi-exponential parameters reflect the bio-physical data, i.e. two spin components (fat and water spins). The lower the AIC value the better the model describes the data.

The T_2 analysis using the AIC test showed that the bi-exponential approach is the globally preferred analysis model in both diffuse fatty liver and nodules. In control animal livers, fewer than 45% of pixels were best modelled using a bi-exponential fit. These findings indicate that the bi-exponential model is best at quantifying fatty liver disease. We also calculated F test results for comparison. The F test results were consistent with AIC only for week 12 data in diffuse fatty liver but not for later time points. The r^2 analysis shows the goodness of fit. It can be used as guidance as to whether the selected model fits the underlying experimental data. Our result showed that >95% of the pixels exhibited higher r^2 for control, diffuse fatty liver, and nodules if a bi-exponential model was applied.

The use of AIC analysis showed that the bi-exponential fit is the preferred model for the CDAA group and is consistent with the increased signal in T_2 image in CDAA group, compared to controls, resulting from the addition of the long T_2 signal fraction introduced in the diffuse fatty liver. Both the T_2 long value and its fraction correlated significantly with decreasing FF measured by the Dixon method.

To the best of our knowledge, our study is the first to use a quantitative bi-exponential model of T_2 decay in *in vivo* fatty liver. The analysis described here may be carried out in future studies in liver diseases, in particular with fatty liver infiltration. It is reasonable that living tissue exhibits several T_2 components, the result being a bi- or multi-exponential relaxation process [197]. Consequently, applying bi- or multi-exponential fits for T_2 calculations allows for the investigation of the microarchitecture of a tissue at the sub-voxel level, thereby increasing the clinical potential of tissue characterization by MR imaging [197, 210].

Non-alcoholic fatty liver disease (NAFLD) consists of a spectrum of pathologies including hepatic steatosis (the earliest manifestation and hallmark), non-alcoholic steatohepatitis (NASH), liver fibrosis, liver cirrhosis, and finally HCC. The microarchitecture at the sub-voxel scale in the liver at each stage is likely to be altered (particularly the fat fraction), resulting in changes in bi-T_2 characteristics during the progression. The chemical composition of the lipids during the changing pathological states may change with different characteristic T_2 values. Using a mono-exponential analysis would therefore mask small changes in the T_{2L} or fat T_2 value. Separating out the T_{2S} and T_{2L} component allows more accurate modelling of T_{2L} increasing the potential to detect smaller changes with changing pathology. There are no studies determining the influence of these stages on bi-T_2 relaxation times in liver. Therefore, applying a bi-exponential model is important to accurately determine the two T_2 components for liver evaluation in a longitudinal study. Changes in the fat component may allow tracking of drug efficacy or characterizing progression of fatty liver disease before development of full HCC.

7.3.2 Whole liver T_2 and FF analysis

The positive correlation of whole diffuse fatty liver with T_{2L}, and T_{2M} with FF, and the negative correlation of ρ_S with *FF* indicate that T_{2L}, ρ_L, and T_{2M} increase with FF while ρ_S decreases. For the animals investigated in this study, the maximum FF and T_{2L} fraction was evident at 12 weeks and then progressively decreased during the study. Previous studies have reported that FF measured by MR decreases as fibrosis increases [240].This was proposed to be a consequence of fibrotic tissue replacing hepatocytes. Future studies performing a more detailed investigation of changes in T_{2S} and T_{2L} in association with histological investigation of fibrosis may provide additional non-invasive biomarkers for tracking progressive liver disease.

The Pearson correlation coefficient model determined that T_{2S} was correlated weakly with FF. This indicates that fat has a weak effect on T_{2S} throughout the liver. This behaviour of the T_{2S} component was consistent with our assumption for the fat fraction in which the T_{2S} component reflects water signal and is not affected by the fat fraction. Moreover, the similarity and relatively constant value of T_{2S} over time in both CDAA and control groups indicates that the underlying T_{2S} is dominated by one tissue constituent that is not changing significantly during this period consistent with liver water in both groups. Any interpretation of T_{2S} remains speculative, and more studies are needed to confirm these conclusions.

7.3.3 Nodular T_2 and FF parameters

Eleven focal lesions were identified and monitored during the time course of this study and verified by histology after the last MR *in vivo* time point. The main MR quantitative findings of these nodules were that (i) FF and T_{2M} were significantly lower compared to the surrounding fatty liver tissue at all-time points, and no correlation was shown between FF and T_2 parameters. Interestingly, when comparing the T_{2M} with bi-exponential T_2 parameters, the difference in T_{2M} was statistically significant in all time points between nodules and surrounding liver tissues, while the difference in T_{2L}, ρ_L and ρ_S were significant only in certain time points.

The decreased level of fat in the lesions quantified by the MR methods was consistent with histological findings of decreased fat droplets within nodules. This was the case even when lesions were not obvious in conventional *in vivo* MR images. This strengthens the case for applying quantitative FF and T_2 pixel-wise analysis of livers with suspected pathology. In addition to the difference in mono-exponential decay for nodular evaluation, relative to surrounding tissue in our study, nodular signal exhibited two T_2 components bi-exponentially in all eleven lesions detected in the CDAA animals *in vivo.*

According to the histology findings, the nodules detected in this MRI study were hyperplastic nodules (benign). The qualitative and statistical descriptive range of regenerative nodules using our quantitative MRI is presented in table 7-1

Table 7-1. Statistical descriptive of regenerative nodules using quantitative MRI

Lesion size (mm)	**T_2 image**	**IP/OP images**	**FF (%)**	**T_{2M} (ms)**	**T_{2L} (ms)**	**T_{2S} (ms)**	**ρ_S (%)**	**ρ_L (%)**
0.68-3.2	hypo-intensity	hyper-intensity	14-20	19-23	43-60	7.5-9	68-83	17-31

The poor correlation between FF with T_2 parameters found in nodules over time suggests that nodular T_2 values in longitudinal studies were less influenced by FF, and may more be likely affected by other physiological alterations. T_2 can be influenced by inflammation, perfusion changes, edema, or steatosis [234]. Therefore, it is reasonable to assume that the T_2 parameters in nodules may represent other pathological factors, not just steatosis as indicated by the steatotic liver tissue investigated in this study. The nodular T_2

values were lower relative to the surrounding liver tissue at each time point, consistent with the lower FF in the tumours.

Other mechanisms have been proposed for a decrease in the T_2 value in liver nodules. The presence of angiogenesis within the tumours which may result in accumulation of paramagnetic deoxyhemoglobin [241], that may play a role in the decreased T_2 value. Another explanation is that iron deposits within the nodules may also lead to hypo-intensity of nodules on T_2 images and lower T_2 values when compared with surrounding fatty liver tissue. Iron is in the form Fe^{3+}, which is paramagnetic and thus may generate low signal intensity on conventional T_2 images [242].

In non-cirrhotic livers, focal benign fatty change is known to occur in chronic liver disease, and needs to be differentiated from other focal tumors. In the cirrhotic liver, fatty change within a precancerous lesion has been recognized as an expression of malignant transformation to HCC during hepatocarcinogenesis [243, 244]. This indicates that the presence of fat within focal lesions raises concern for HCC lesion development but not in other types of malignant liver tumors [245]. Therefore, the detection of fat-containing lesions may help to exclude other malignancy such as cholangiocarcinoma [246].

The underlying nodular physiological origin of the multi-T_2 parameters in our study is unknown, and so additional studies are needed to understand our observations. One proposed investigation would be to use *in vivo* MR T_2 multi-exponential analysis and histopathology at each time point to evaluate the underlying physiological changes of nodules and make correlation of these measures. Measurement of multiple T_2 component and FF as well as histological analysis show potential for characterizing the pathological microenvironmental changes within the lesion.

To our knowledge, no previous study has correlated the FF with mono- and bi-compartment T_2 values to detect and evaluate early changes during development of hepatocellular carcinoma. Fatty infiltration should be considered when using quantitative T_2 mapping for characterizing HCC since T_2 relaxation times are modified by the degree of fat present.

A limitation of the current study that could be addressed in future studies includes the number and range of TE values used to $T2$ mono- and bi-exponential analysis. The maximum TE time was 130 ms. Figure 3-5 illustrates that the signal intensity appeared to be constant and reached the noise level by 130 ms. However, in the CDAA rats with steatotic livers, the image signal intensity was still decreasing at 130 ms. This has the potential to affect curve fitting, particularly the T_{2L} component. Additional studies with severely steatotic livers should be investigated to determine the maximum TE required for the image intensity to reach the noise level. An expanded study would also benefit from adding histological assessment at each time point. The animals in our study developed benign hyperplastic lesions. Extending the final time point to allow development of HCC would also benefit assessment of quantitative FF and T2 changes to understand the complete HCC formation process.

7.4 Conclusion

A bi-exponential T_2 model and Dixon imaging has been applied to produce parametric information from liver tissue during steatosis and development of hyperplastic nodules in a CDAA rat model. A correlation between T_2 values (T_{2M} and T_{2L}, ρ_L, and ρ_S) and FF were observed in diffuse fatty liver, suggesting that these parameters are good predictors of the functional status of animals with diffuse fatty liver and reflect changes in liver steatosis. In contrast, liver nodules detected did not demonstrate the same correlation between T_2 components and FF. This opens new paths to investigate differences in the T_2 components in diffuse liver steatosis and nodule formation. This may lead to new methods to detect and assess nodule formation and progressive liver disease.

7.5 Future Perspective

The results of our study suggest that quantitative MRI biomarkers can be correlated with the grading pathological liver tissue during hepatocarcinogenesis. However, the long *in vivo* MR follow-up periods designed for this study (57 weeks after diet administration) did not reach the stage where there is significant development of HCC occurs. Future studies should focus on extending the study to include development of HCC to characterise T_2 parameters as a function of disease progression, with FF and T_2 to potentially play a role in differentiating cancer from benign lesions.

Extension of the work presented in this study could benefit from the following:

- MR spectroscopy (MRS): to monitor alterations in lipid metabolism in animal model of hepatocarcinogenesis at different stages of nodule and tumour development. To the best of our knowledge, no MRS study has been completed to assess potential risk factors for progression of diffuse fatty liver or benign lesions to development of HCC. Therefore, we propose the use of spectroscopic imaging to examine liver tissue for early biochemical changes from fatty liver disease to the development of benign and malignant tumour for comparison to our results.
- Contrast-enhanced (CE) MRI: Contrast-enhanced (CE) MRI is an accepted clinical diagnostic imaging method to assist characterization of hepatic nodules during carcinogenesis based on intra-nodular blood supply. Future studies integrating CE measurements into the multi-parametric analysis may improve the accuracy of HCC characterization during hepatocarcinogenesis.

  - Histology: Histological grading at all-time MRI points would be helpful in understanding the physiological basis of the measured T_2 parameters. This would allow for a confident characterization of most liver lesions and potentially may help to establish MR cut-off values to predict lesions at risk for progression to liver tumors.

- Pre-clinical application of DWI in *in vivo* liver is limited, mainly owing to inherent drawbacks, including motion artifacts, chemical shift artefacts, and susceptibility artefacts. These reasons had affected our result and showed the difficulty in obtaining DWI images with sufficient quality for reliable quantitative analysis. The limitation studies and our result underline the importance for further studies that are needed to optimize and standardize liver DWI. Approaches involving hardware improvements and upgrade could be beneficial in tackling these challenges. Developing post-processing techniques to increase image quality and reduce artifacts is needed. However, there are some solutions that can be used to minimize these artifacts. For motion artifact, intramuscular administration of buscopan can be used to decrease intestinal peristalsis. Using lower magnetic field contributes to lower susceptibility and chemical shift artifacts.

References

1. Baffy, G., E.M. Brunt, and S.H. Caldwell, *Hepatocellular carcinoma in non-alcoholic fatty liver disease: An emerging menace.* Journal of Hepatology, 2012. **56**(6): p. 1384-1391.
2. Alison, M.R. and M.J. Lovell, *Liver cancer: the role of stem cells.* Cell Proliferation, 2005. **38**(6): p. 407-421.
3. Altekruse, S.F., K.A. McGlynn, and M.E. Reichman, *Hepatocellular carcinoma incidence, mortality, and survival trends in the United States from 1975 to 2005.* Journal of Clinical Oncology, 2009. **27**(9): p. 1485-1491.
4. MacLachlan, J.H. and B.C. Cowie, *Liver cancer is the fastest increasing cause of cancer death in Australians.* Medical Journal of Australia, 2012. **197**(9): p. 492.
5. Hoshida, Y., B.C. Fuchs, and K.K. Tanabe, *Prevention of hepatocellular carcinoma: potential targets, experimental models, and clinical challenges.* Current cancer drug targets, 2012. **12**(9): p. 1129.
6. Takayama, T., et al., *Early Hepatocellular Carcinoma: Pathology, Imaging, and Therapy.* Annals of Surgical Oncology, 2008. **15**(4): p. 972-978.
7. Padhya, K.T., J.A. Marrero, and A.G. Singal, *Recent advances in the treatment of hepatocellular carcinoma.* Current opinion in gastroenterology, 2013. **29**(3): p. 285-292.

8. Singal, A.G., A. Pillai, and J. Tiro, *Early detection, curative treatment, and survival rates for hepatocellular carcinoma surveillance in patients with cirrhosis: a meta-analysis.* PLoS Med, 2014. **11**(4): p. e1001624.
9. Taouli, B., et al., *Magnetic resonance imaging of hepatocellular carcinoma.* Gastroenterology, 2004. **127**(5): p. S144-S152.
10. Hanna, R.F., et al., *Cirrhosis-associated hepatocellular nodules: correlation of histopathologic and MR imaging features.* Radiographics, 2008. **28**(3): p. 747-69.
11. Silva, A.C., et al., *MR imaging of hypervascular liver masses: a review of current techniques.* Radiographics, 2009. **29**(2): p. 385-402.
12. Kim, M.-J., et al., *Focal Hepatic Lesions: Detection and Characterization with Combination Gadolinium- and Superparamagnetic Iron Oxide–enhanced MR Imaging.* Radiology, 2003. **228**(3): p. 719-726.
13. Kele, P.G. and E.J. van der Jagt, *Diffusion weighted imaging in the liver.* World journal of gastroenterology: WJG, 2010. **16**(13): p. 1567.
14. Kumar, A., et al., *Role of in vivo proton MR spectroscopy in the evaluation of adult brain lesions: Our preliminary experience.* Neurology India, 2003. **51**(4): p. 474.
15. Jacobs, M.A., et al., *Proton magnetic resonance spectroscopic imaging of human breast cancer: a preliminary study.* Journal of Magnetic Resonance Imaging, 2004. **19**(1): p. 68-75.
16. HASUMI, M., et al., *MR spectroscopy as a reliable diagnostic tool for localization of prostate cancer.* Anticancer research, 2002. **22**(2B): p. 1205-1208.
17. van Werven, J.R., et al., *Hepatic lipid composition analysis using 3.0-T MR spectroscopy in a steatotic rat model.* Magnetic Resonance Imaging, 2012. **30**(1): p. 112-121.
18. Towner, R.A., L.M. Foley, and D.M. Painter, *Hepatocarcinogenesis tumor grading correlated with in vivo image-guided< sup> 1</sup> H-NMR spectroscopy in a rat model.* Toxicology and Applied Pharmacology, 2005. **207**(2): p. 237-244.
19. Zhao, W.-D., et al., *In vivo detection of metabolic changes by 1 H-MRS in the DEN-induced hepatocellular carcinoma in Wistar rat.* Journal of cancer research and clinical oncology, 2005. **131**(9): p. 597-602.
20. Gambarota, G., et al., *Measurements of T1 and T2 relaxation times of colon cancer metastases in rat liver at 7 T.* MAGMA, 2004. **17**(3-6): p. 281-7.
21. International Working, P., *Terminology of nodular lesions of the liver: recommendations of the World Congress of Gastroenterology Working Group.* Hepatology, 1995. **22**: p. 983-993.
22. Takayama, T., et al., *Malignant transformation of adenomatous hyperplasia to hepatocellular carcinoma.* The Lancet, 1990. **336**(8724): p. 1150-1153.
23. Kim, C.K., et al., *Neoangiogenesis and Sinusoidal Capillarization in Hepatocellular Carcinoma: Correlation between Dynamic CT and Density of Tumor Microvessels1.* Radiology, 2005. **237**(2): p. 529-534.
24. Taguchi, K.-I., et al., *Morphologic approach to hepatocellular carcinoma development in man: De novo or the so-called< dysplastic nodule-carcinoma> sequence?* Oncology reports, 2002. **9**(4): p. 737-743.
25. Paradis, V., *Histopathology of Hepatocellular Carcinoma*, in *Multidisciplinary Treatment of Hepatocellular Carcinoma*. 2013, Springer. p. 21-32.
26. Park, Y.N., *Update on Precursor and Early Lesions of Hepatocellular Carcinomas.* Archives of Pathology & Laboratory Medicine, 2011. **135**(6): p. 704-715.
27. Nakashima, T. and M. Kojiro. *Pathologic characteristics of hepatocellular carcinoma*. in *Seminars in liver disease*. 1986.

28. Kojiro, M., *Pathology of Hepatocellular Carcinoma*, in *Molecular Genetics of Liver Neoplasia*, X.W. Wang, J.W. Grisham, and S.S. Thorgeirsson, Editors. 2011, Springer New York. p. 37-48.
29. Kuesel, A.C., et al., *1H MRS of high grade astrocytomas: mobile lipid accumulation in necrotic tissue.* NMR in biomedicine, 1994. **7**(3): p. 149-155.
30. Digumarthy, S.R., D.V. Sahani, and S. Saini, *MRI in detection of hepatocellular carcinoma (HCC).* Cancer Imaging, 2005. **5**(1): p. 20.
31. Martin, J., et al., *Fatty metamorphosis of hepatocellular carcinoma: detection with chemical shift gradient-echo MR imaging.* Radiology, 1995. **195**(1): p. 125-30.
32. Kutami, R., et al., *Pathomorphologic study on the mechanism of fatty change in small hepatocellular carcinoma of humans.* Journal of hepatology, 2000. **33**(2): p. 282-289.
33. Angulo, P., *Nonalcoholic fatty liver disease.* N Engl J Med, 2002. **346**(16): p. 1221-31.
34. Takahashi, Y. and T. Fukusato, *Pediatric nonalcoholic fatty liver disease: overview with emphasis on histology.* World Journal Gastroenterol, 2010. **16**(42): p. 5280-5.
35. Zoller, H. and H. Tilg, *Nonalcoholic fatty liver disease and hepatocellular carcinoma.* Metabolism, 2016. **65**(8): p. 1151-1160.
36. Koteish, A. and A.M. Diehl, *Animal models of steatosis.* Semin Liver Dis, 2001. **21**(1): p. 89-104.
37. Bradbury, M.W. and P.D. Berk, *Lipid metabolism in hepatic steatosis.* Clin Liver Dis, 2004. **8**(3): p. 639-71, xi.
38. Vernon, G., A. Baranova, and Z. Younossi, *Systematic review: the epidemiology and natural history of non‐alcoholic fatty liver disease and non‐alcoholic steatohepatitis in adults.* Alimentary pharmacology & therapeutics, 2011. **34**(3): p. 274-285.
39. Leung, C., et al., *Characteristics of hepatocellular carcinoma in cirrhotic and non-cirrhotic non-alcoholic fatty liver disease.* World Journal of Gastroenterology: WJG, 2015. **21**(4): p. 1189.
40. Guzman, G., et al., *Does nonalcoholic fatty liver disease predispose patients to hepatocellular carcinoma in the absence of cirrhosis?* Archives of pathology & laboratory medicine, 2008. **132**(11): p. 1761-1766.
41. Ma, X., et al., *Imaging-based Quantification of Hepatic Fat: Methods and Clinical Applications 1.* Radiographics, 2009. **29**(5): p. 1253-1277.
42. Ligabue, G., et al., *MR quantitative biomarkers of non-alcoholic fatty liver disease: technical evolutions and future trends.* Quantitative imaging in medicine and surgery, 2013. **3**(4): p. 192.
43. Arun, J., et al., *Influence of liver biopsy heterogeneity and diagnosis of nonalcoholic steatohepatitis in subjects undergoing gastric bypass.* Obesity Surgery, 2007. **17**(2): p. 155-161.
44. Machann, J., et al., *Hepatic lipid accumulation in healthy subjects: A comparative study using spectral fat-selective MRI and volume-localized 1H-MR spectroscopy.* Magnetic Resonance in Medicine, 2006. **55**(4): p. 913-917.
45. Schwenzer, N.F., et al., *Non-invasive assessment and quantification of liver steatosis by ultrasound, computed tomography and magnetic resonance.* J Hepatol, 2009. **51**(3): p. 433-45.
46. Dixon, W.T., *Simple proton spectroscopic imaging.* Radiology, 1984. **153**(1): p. 189-194.

47. Raptis, D.A., et al., *MRI: the new reference standard in quantifying hepatic steatosis?* Gut, 2012. **61**(1): p. 117-127.
48. Pitot, H.C., et al., *Biochemical markers associated with the stages of promotion and progression during hepatocarcinogenesis in the rat.* Environmental Health Perspectives, 1991. **93**: p. 181-189.
49. Thoolen, B., et al., *Comparative histomorphological review of rat and human hepatocellular proliferative lesions.* Journal of toxicologic pathology, 2012. **25**(3): p. 189.
50. Bagi, C.M. and C.J. Andresen, *Models of hepatocellular carcinoma and biomarker strategy.* Cancers, 2010. **2**(3): p. 1441-1452.
51. Feo, F., et al., *Hepatocellular carcinoma as a complex polygenic disease. Interpretive analysis of recent developments on genetic predisposition.* Biochimica et Biophysica Acta (BBA)-Reviews on Cancer, 2006. **1765**(2): p. 126-147.
52. Feo, F., R.M. Pascale, and D.F. Calvisi, *Models for liver cancer.* The cancer handbook, 2007.
53. Borbath, I., et al., *Efficacy of lanreotide in preventing the occurrence of chemically induced hepatocellular carcinoma in rats.* Chemico-Biological Interactions, 2010. **183**(1): p. 238-248.
54. Stefaniuk, P., J. Cianciara, and A. Wiercinska-Drapalo, *Present and future possibilities for early diagnosis of hepatocellular carcinoma.* World journal of gastroenterology: WJG, 2010. **16**(4): p. 418.
55. Podda, M., et al., *Liver-cell dysplasia and hepatocellular carcinoma.* Ital J Gastroenterol, 1992. **24**(1): p. 39-42.
56. Heindryckx, F., I. Colle, and H. Van Vlierberghe, *Experimental mouse models for hepatocellular carcinoma research.* International journal of experimental pathology, 2009. **90**(4): p. 367-386.
57. Nakae, D., et al., *High incidence of hepatocellular carcinomas induced by a choline deficient L-amino acid defined diet in rats.* Cancer research, 1992. **52**(18): p. 5042-5045.
58. Freimuth, J., et al., *Application of magnetic resonance imaging in transgenic and chemical mouse models of hepatocellular carcinoma.* Mol Cancer, 2010. **9**: p. 94.
59. Park, D.-H., et al., *Diethylnitrosamine (DEN) induces irreversible hepatocellular carcinogenesis through overexpression of G1/S-phase regulatory proteins in rat.* Toxicology Letters, 2009. **191**(2–3): p. 321-326.
60. Vesselinovitch, S.D. and N. Mihailovich, *Kinetics of diethylnitrosamine hepatocarcinogenesis in the infant mouse.* Cancer Reseach, 1983. **43**(9): p. 4253-9.
61. El-Shahat, M., et al., *Potential chemoprevention of diethylnitrosamine-induced hepatocarcinogenesis in rats: myrrh (Commiphora molmol) vs. turmeric (Curcuma longa).* Acta Histochem, 2012. **114**(5): p. 421-8.
62. Verna, L., J. Whysner, and G.M. Williams, *N-nitrosodiethylamine mechanistic data and risk assessment: bioactivation, DNA-adduct formation, mutagenicity, and tumor initiation.* Pharmacology & therapeutics, 1996. **71**(1): p. 57-81.
63. Bartsch, H., *N-nitroso compounds and human cancer: where do we stand?* IARC scientific publications, 1990(105): p. 1-10.
64. Ni, Y., et al., *Magnetic resonance imaging, microangiography, and histology in a rat model of primary liver cancer.* Investigative Radiology, 1992. **27**(9): p. 689-697.
65. Lee, J.-S., et al., *Application of comparative functional genomics to identify best-fit mouse models to study human cancer.* Nature genetics, 2004. **36**(12): p. 1306-1311.

66. Kim, M.R., et al., *Cell cycle protein profile of the hepatic stellate cells (HSCs) in dimethylnitrosamine-induced rat hepatic fibrosis.* Experimental and Molecular Medicine, 2005. **37**(4): p. 335-342.
67. Verna, L., J. Whysner, and G.M. Williams, *N-Nitrosodiethylamine mechanistic data and risk assessment: Bioactivation, DNA-adduct formation, mutagenicity, and tumor initiation.* Pharmacology and Therapeutics, 1996. **71**(1-2): p. 57-81.
68. Lee, J. and S. Thorgeirsson, *Comparative and integrative functional genomics of HCC.* Oncogene, 2006. **25**(27): p. 3801-3809.
69. De Minicis, S., et al., *New insights in hepatocellular carcinoma: from bench to bedside.* Annals of Translational Medicine, 2013. **1**(2).
70. Lee, G.H., *Paradoxical effects of phenobarbital on mouse hepatocarcinogenesis.* Toxicol Pathol, 2000. **28**(2): p. 215-25.
71. Edmondson, H.A. and P.E. Steiner, *Primary carcinoma of the liver. A study of 100 cases among 48,900 necropsies.* Cancer, 1954. **7**(3): p. 462-503.
72. Zeisel, S., *Vitamin-like" molecules: Choline.* Modern Nutrition in Health and Disease, 1988: p. 440-452.
73. Michel, V., et al., *Choline transport for phospholipid synthesis.* Experimental biology and medicine, 2006. **231**(5): p. 490-504.
74. Reddy, B.S., *Dietary fat and colon cancer: animal models.* Preventive Medicine, 1987. **16**(4): p. 460-467.
75. Knight, B., et al., *Impaired preneoplastic changes and liver tumor formation in tumor necrosis factor receptor type 1 knockout mice.* The Journal of experimental medicine, 2000. **192**(12): p. 1809-1818.
76. Nakano, T., et al., *Impact of artificial sunlight therapy on the progress of non-alcoholic fatty liver disease in rats.* Journal of hepatology, 2011. **55**(2): p. 415-425.
77. Ghoshal, A.K., A.K. Ghoshal, and E. Farber, *The induction of liver cancer by dietary deficiency of choline and methionine without added carcinogens.* Carcinogenesis (New York), 1984. **5**(10): p. 1367-1370.
78. Tessitore, L., et al., *Sexually differentiated response to choline in choline deficiency and ethionine intoxication.* International journal of experimental pathology, 1995. **76**(2): p. 125.
79. Frese, K.K. and D.A. Tuveson, *Maximizing mouse cancer models.* Nature Review Cancer, 2007. **7**(9): p. 645-58.
80. Fausto, N. and J.S. Campbell. *Mouse models of hepatocellular carcinoma*. in *Seminars in liver disease*. 2010. © Thieme Medical Publishers.
81. DePinho, R.A., N. Schreiber-Agus, and F.W. Alt, *< i> myc</i> Family Oncogenes in the Development of Normal and Neoplastic Cells.* Advances in cancer research, 1991. **57**: p. 1-46.
82. Morgenbesser, S.D. and R.A. DePinho. *Use of transgenic mice to study myc family gene function in normal mammalian development and in cancer*. in *Seminars in cancer biology*. 1994.
83. Sandgren, E., et al., *Oncogene-induced liver neoplasia in transgenic mice.* Oncogene, 1989. **4**(6): p. 715-724.
84. Perraud, F., et al., *Characterization of trans-immortalized hepatic cell lines established from transgenic mice.* Experimental cell research, 1991. **195**(1): p. 59-65.
85. Sell, S., *Mouse models to study the interaction of risk factors for human liver cancer.* Cancer research, 2003. **63**(22): p. 7553-7562.
86. Kanematsu, M., et al., *Magnetic Resonance Imaging of Hepatocellular Carcinoma.* Oncology, 2008. **75**(1): p. 65-71.

87. Hussain, H.K., et al., *Hepatic Fat Fraction: MR Imaging for Quantitative Measurement and Display—Early Experience 1.* Radiology, 2005. **237**(3): p. 1048-1055.
88. Mitchell, D.G., et al., *Hepatocellular tumors with high signal on T1-weighted MR images: chemical shift MR imaging and histologic correlation.* Journal of computer assisted tomography, 1991. **15**(5): p. 762-769.
89. Amano, S., et al., *Assessment of cancer cell differentiation in small hepatocellular carcinoma by computed tomography and magnetic resonance imaging.* Journal of gastroenterology and hepatology, 2003. **18**(3): p. 273-279.
90. Ebara, M., et al., *Small hepatocellular carcinoma: relationship of signal intensity to histopathologic findings and metal content of the tumor and surrounding hepatic parenchyma.* Radiology, 1999. **210**(1): p. 81-88.
91. Kadoya, M., et al., *Hepatocellular carcinoma: correlation of MR imaging and histopathologic findings.* Radiology, 1992. **183**(3): p. 819-825.
92. Li, C.S., et al., *Magnetic resonance imaging appearance of well-differentiated hepatocellular carcinoma.* Journal of computer assisted tomography, 2006. **30**(4): p. 597-603.
93. Patel, A., et al., *MRI for Detection and Evaluation of Hepatocellular Carcinoma*, in *Hepatocellular Carcinoma*. 2016, Springer. p. 391-397.
94. Busuttil, R.W. and K. Tanaka, *The utility of marginal donors in liver transplantation.* Liver transplantation, 2003. **9**(7): p. 651-663.
95. Reeder, S.B., et al., *Quantitative Assessment of Liver Fat with Magnetic Resonance Imaging and Spectroscopy.* Journal of Magnetic Resonance Imaging, 2011. **34**(4): p. 729-749.
96. Matsui, O., et al., *Benign and malignant nodules in cirrhotic livers: distinction based on blood supply.* Radiology, 1991. **178**(2): p. 493-497.
97. Krinsky, G.A., *MRI reveals liver cancer in time to save lives.* DIAGNOSTIC IMAGING-SAN FRANCISCO-, 2001. **23**(1; SUPP): p. 14-16.
98. Earls, J.P., et al., *Dysplastic nodules and hepatocellular carcinoma: thin-section MR imaging of explanted cirrhotic livers with pathologic correlation.* Radiology, 1996. **201**(1): p. 207-214.
99. Ward, J. and P.J. Robinson, *How to detect hepatocellular carcinoma in cirrhosis.* European radiology, 2002. **12**(9): p. 2258-2272.
100. Krinsky, G.A., et al., *Hepatocellular Carcinoma and Dysplastic Nodules in Patients with Cirrhosis: Prospective Diagnosis with MR Imaging and Explantation Correlation1.* Radiology, 2001. **219**(2): p. 445-454.
101. Kim, T., R.L. Baron, and M.A. Nalesnik, *Infarcted regenerative nodules in cirrhosis CT and MR imaging findings with pathologic correlation.* American Journal of Roentgenology, 2000. **175**(4): p. 1121-1125.
102. Willatt, J.M., et al., *MR Imaging of Hepatocellular Carcinoma in the Cirrhotic Liver: Challenges and Controversies1.* Radiology, 2008. **247**(2): p. 311-330.
103. Deng, J., et al., *Quantitative multiparametric PROPELLER MRI of diethylnitrosamine-induced hepatocarcinogenesis in wister rat model.* J Magn Reson Imaging, 2010. **31**(5): p. 1242-51.
104. Bang, D.-H., et al., *Gd-EOB-DTPA Enhanced Micro-MR Imaging of Hepatic Tumors in H-ras 12V Transgenic Mice.* Academic Radiology, 2011. **18**(1): p. 13-19.
105. Schmid, A., et al., *Quantitative analysis of the growth kinetics of chemically induced mouse liver tumors by magnetic resonance imaging.* Toxicological Sciences, 2012. **126**(1): p. 52-59.

106. Bokacheva, L., et al., *High-field small animal magnetic resonance oncology studies.* Physics in medicine and biology, 2014. **59**(2): p. R65.
107. Matsui, O., *Imaging of multistep human hepatocarcinogenesis by CT during intra-arterial contrast injection.* Intervirology, 2004. **47**(3-5): p. 271-276.
108. Lee, J. and B. Choi, *Hepatocellular nodules in liver cirrhosis: MR evaluation.* Abdominal Imaging, 2011. **36**(3): p. 282-289.
109. Luna, A., et al., *Overview of Functional Imaging Techniques for Liver Malignancies in Current Clinical Practice or in a Very Near Future*, in *Functional Imaging in Oncology*. 2014, Springer. p. 951-985.
110. Shellock, F.G., et al., *Safety of gadobenate dimeglumine (MultiHance): Summary of findings from clinical studies and postmarketing surveillance.* Invest Radiol, 2006. **41**(6): p. 500-9.
111. Weinmann, H.J., et al., *A new lipophilic gadolinium chelate as a tissue-specific contrast medium for MRI.* Magnetic Resonance in Medicine, 1991. **22**(2): p. 233-237.
112. Park, G., et al., *Diagnostic efficacy of gadoxetic acid-enhanced MRI in the detection of hepatocellular carcinomas: comparison with gadopentetate dimeglumine.* Br J Radiol, 2010. **83**(996): p. 1010-6.
113. Frericks, B.B., et al., *Qualitative and Quantitative Evaluation of Hepatocellular Carcinoma and Cirrhotic Liver Enhancement Using Gd-EOB-DTPA.* American Journal of Roentgenology, 2009. **193**(4): p. 1053-1060.
114. Bashir, M.R., et al., *Hepatocellular carcinoma in a North American population: Does hepatobiliary MR imaging with Gd-EOB-DTPA improve sensitivity and confidence for diagnosis?* Journal of Magnetic Resonance Imaging, 2013. **37**(2): p. 398-406.
115. Kogita, S., et al., *Gd-EOB-DTPA-enhanced magnetic resonance images of hepatocellular carcinoma: correlation with histological grading and portal blood flow.* European Radiology, 2010. **20**(10): p. 2405-2413.
116. Bartolozzi, C., et al., *Contrast-enhanced magnetic resonance imaging of 102 nodules in cirrhosis: correlation with histological findings on explanted livers.* Abdominal Imaging, 2013. **38**(2): p. 290-296.
117. Korkusuz, H., et al., *Different signal intensity at Gd-EOB-DTPA compared with Gd-DTPA-enhanced MRI in hepatocellular carcinoma transgenic mouse model in delayed phase hepatobiliary imaging.* J Magn Reson Imaging, 2012. **35**(6): p. 1397-402.
118. Ferrucci, J. and D. Stark, *Iron oxide-enhanced MR imaging of the liver and spleen: review of the first 5 years.* AJR. American journal of roentgenology, 1990. **155**(5): p. 943-950.
119. Yamamoto, H., et al., *Hepatocellular carcinoma in cirrhotic livers: detection with unenhanced and iron oxide-enhanced MR imaging.* Radiology, 1995. **195**(1): p. 106-112.
120. Guo, D.M., et al., *Detection and characterization of hepatocellular carcinoma in rats with liver cirrhosis: diagnostic value of combined use of MR positive and negative contrast agents.* Hepatobiliary Pancreat Dis Int, 2009. **8**(1): p. 65-70.
121. Cameron, I.L., V.A. Ord, and G.D. Fullerton, *Characterization of proton NMR relaxation times in normal and pathological tissues by correlation with other tissue parameters.* Magnetic resonance imaging, 1984. **2**(2): p. 97-106.
122. POLAK, J.F., M.T. VIVALDI, and F.J. SCHOEN, *Proton magnetic resonance of early myocardial infarction in rats.* Investigative radiology, 1988. **23**(6): p. 428-432.
123. Frey, H., et al., *Proton spin-lattice relaxation studies of nonmalignant tissues of tumorous mice.* Journal of the National Cancer Institute, 1972. **49**(3): p. 903-906.

124. Raza, S.A., et al., *Assessment of colorectal hepatic metastases by quantitative T2 relaxation time.* European Journal of Radiology, 2012. **81**(4): p. e536-e540.
125. Nitz, W.R. and P. Reimer, *Contrast mechanisms in MR imaging.* European Radiology, 1999. **9**(6): p. 1032-1046.
126. Damadian, R., *Tumor Detection by Nuclear Magnetic Resonance.* Science, 1971. **171**(3976): p. 1151-1153.
127. Fenlon, H.M., et al., *Signal characteristics of focal liver lesions on double echo T2-weighted conventional spin echo MRI: Observer performance versus quantitative measurements of T2 relaxation times.* Journal of computer assisted tomography, 2000. **24**(2): p. 204-211.
128. Cieszanowski, A., et al., *Discrimination of benign from malignant hepatic lesions based on their T2-relaxation times calculated from moderately T2-weighted turbo SE sequence.* European radiology, 2002. **12**(9): p. 2273-2279.
129. Gambarota, G., et al., *Measurements of T1 and T2 relaxation times of colon cancer metastases in rat liver at 7 T.* Magnetic Resonance Materials in Physics, Biology and Medicine, 2004. **17**(3-6): p. 281-287.
130. Goldberg, M.A., et al., *Value of T1 and T2 relaxation times from echoplanar MR imaging in the characterization of focal hepatic lesions.* American Journal of Roentgenology, 1993. **160**(5): p. 1011-1017.
131. Farraher, S.W., et al., *Differentiation of hepatocellular carcinoma and hepatic metastasis from cysts and hemangiomas with calculated T2 relaxation times and the T1/T2 relaxation times ratio.* Journal of Magnetic Resonance Imaging, 2006. **24**(6): p. 1333-1341.
132. Le Bihan, D., et al., *Diffusion tensor imaging: Concepts and applications.* Journal of Magnetic Resonance Imaging, 2001. **13**(4): p. 534-546.
133. Chrysikopoulos, H.S., *Clinical MR Imaging and Physics.* EBOOK, 2009.
134. Derek, K., *Diffusion MRI: Theory, methods, and applications.* 2011.
135. Taouli, B. and D.-M. Koh, *Diffusion-weighted MR Imaging of the Liver1.* Radiology, 2010. **254**(1): p. 47-66.
136. Filippi, M., et al., *Diffusion tensor magnetic resonance imaging in multiple sclerosis.* Neurology, 2001. **56**(3): p. 304-311.
137. Bammer, R., *Basic principles of diffusion-weighted imaging.* European journal of radiology, 2003. **45**(3): p. 169-184.
138. Vilanova, J.C. and J. Barceló, *Diffusion-weighted whole-body MR screening.* European Journal of Radiology, 2008. **67**(3): p. 440-447.
139. Kwee, T.C., et al., *Whole-body diffusion-weighted magnetic resonance imaging.* European Journal of Radiology, 2009. **70**(3): p. 409-417.
140. Bruegel, M., et al., *Characterization of focal liver lesions by ADC measurements using a respiratory triggered diffusion-weighted single-shot echo-planar MR imaging technique.* European radiology, 2008. **18**(3): p. 477-485.
141. Taouli, B., et al., *Evaluation of Liver Diffusion Isotropy and Characterization of Focal Hepatic Lesions with Two Single-Shot Echo-planar MR Imaging Sequences: Prospective Study in 66 Patients 1.* Radiology, 2003. **226**(1): p. 71-78.
142. Kim, T., et al., *Diffusion-weighted single-shot echoplanar MR imaging for liver disease.* AJR. American journal of roentgenology, 1999. **173**(2): p. 393-398.
143. Kojiro, M. and T. Roskams. *Early hepatocellular carcinoma and dysplastic nodules.* in *Seminars in liver disease*. 2005. Copyright© 2005 by Thieme Medical Publishers, Inc., 333 Seventh Avenue, New York, NY 10001, USA.

144. Kanematsu, M., et al., *Detection and characterization of focal hepatic lesions with diffusion-weighted MR imaging: a pictorial review.* Abdominal imaging, 2013. **38**(2): p. 297-308.
145. Xu, H., et al., *Diffusion-Weighted Magnetic Resonance Imaging of Focal Hepatic Nodules in an Experimental Hepatocellular Carcinoma Rat Model.* Academic Radiology, 2007. **14**(3): p. 279-286.
146. Xu, P.-J., et al., *Contribution of Diffusion-Weighted Magnetic Resonance Imaging in the Characterization of Hepatocellular Carcinomas and Dysplastic Nodules in Cirrhotic Liver.* Journal of computer assisted tomography, 2010. **34**(4): p. 506-512.
147. Sandrasegaran, K., et al., *The usefulness of diffusion-weighted imaging in the characterization of liver lesions in patients with cirrhosis.* Clinical radiology, 2013.
148. Muhi, A., et al., *High‐b‐value diffusion‐weighted MR imaging of hepatocellular lesions: Estimation of grade of malignancy of hepatocellular carcinoma.* Journal of Magnetic Resonance Imaging, 2009. **30**(5): p. 1005-1011.
149. Nasu, K., et al., *Diffusion-weighted imaging of surgically resected hepatocellular carcinoma: imaging characteristics and relationship among signal intensity, apparent diffusion coefficient, and histopathologic grade.* American Journal of Roentgenology, 2009. **193**(2): p. 438-444.
150. Lyng, H., O. Haraldseth, and E.K. Rofstad, *Measurement of cell density and necrotic fraction in human melanoma xenografts by diffusion weighted magnetic resonance imaging.* Magnetic resonance in medicine, 2000. **43**(6): p. 828-836.
151. Gibbs, P., et al., *Correlation of ADC and T2 measurements with cell density in prostate cancer at 3.0 Tesla.* Investigative radiology, 2009. **44**(9): p. 572-576.
152. Lang, P., et al., *Osteogenic sarcoma: noninvasive in vivo assessment of tumor necrosis with diffusion-weighted MR imaging.* Radiology, 1998. **206**(1): p. 227-235.
153. Maier, C.F., et al., *Quantitative diffusion imaging in implanted human breast tumors.* Magnetic resonance in medicine, 1997. **37**(4): p. 576-581.
154. *Animal models for magnetic resonance imaging research of the liver.* Investigative radiology, 1992. **27**(5): p. 390-393.
155. Taouli, B., et al., *Evaluation of Liver Diffusion Isotropy and Characterization of Focal Hepatic Lesions with Two Single-Shot Echo-planar MR Imaging Sequences: Prospective Study in 66 Patients1.* Radiology, 2003. **226**(1): p. 71-78.
156. Qian, T., et al., *Diffusion-weighted magnetic resonance imaging to evaluate microvascular density after transarterial embolization ablation in a rabbit VX2 liver tumor model.* Magnetic resonance imaging, 2014.
157. Sun, X., et al., *Diffusion‐weighted MRI of hepatic tumor in rats: Comparison between in vivo and postmortem imaging acquisitions.* Journal of Magnetic Resonance Imaging, 2009. **29**(3): p. 621-628.
158. Voert, E.t., et al., *In vivo magnetic resonance spectroscopy of liver tumors and metastases.* 2011.
159. Foley, L., R. Towner, and D. Painter, *In vivo image-guided< sup> 1</sup> H-magnetic resonance spectroscopy of the serial development of hepatocarcinogenesis in an experimental animal model.* Biochimica et Biophysica Acta (BBA)-General Subjects, 2001. **1526**(3): p. 230-236.
160. Maris, J.M., et al., *31P nuclear magnetic resonance spectroscopic investigation of human neuroblastoma in situ.* The New England journal of medicine, 1985. **312**(23): p. 1500-1505.

161. Towner, R.A., L.M. Foley, and D.M. Painter, *Hepatocarcinogenesis tumor grading correlated with in vivo image-guided 1H-NMR spectroscopy in a rat model.* Toxicology and Applied Pharmacology, 2005. **207**(2, Supplement): p. 237-244.
162. Xu, H., et al., *In Vivo< sup> 1</sup> H MR Spectroscopy in the Evaluation of the Serial Development of Hepatocarcinogenesis in an Experimental Rat Model.* Academic radiology, 2006. **13**(12): p. 1532-1537.
163. Brix, G., et al., *MR imaging of fat-containing tissues: Valuation of two quantitative imaging techniques in comparison with localized proton spectroscopy.* Magnetic Resonance Imaging, 1993. **11**(7): p. 977-991.
164. Cassidy, F.H., et al., *Fatty Liver Disease: MR Imaging Techniques for the Detection and Quantification of Liver Steatosis 1.* Radiographics, 2009. **29**(1): p. 231-260.
165. Li, Y., Z.-Y. Tang, and J.-X. Hou, *Hepatocellular carcinoma: insight from animal models.* Nature Reviews Gastroenterology and Hepatology, 2011. **9**(1): p. 32-43.
166. Festing, M.F. and D.G. Altman, *Guidelines for the design and statistical analysis of experiments using laboratory animals.* ILAR J, 2002. **43**(4): p. 244-58.
167. Festing, M.F., *How to reduce the number of animals used in research by improving experimental design and statistics.* ANZCCART Fact Sheet, 2011. **10**: p. 1-11.
168. Delfour, C., et al., *RCL2, a new fixative, preserves morphology and nucleic acid integrity in paraffin-embedded breast carcinoma and microdissected breast tumor cells.* The Journal of Molecular Diagnostics, 2006. **8**(2): p. 157-169.
169. Thoolen, B., et al., *Proliferative and nonproliferative lesions of the rat and mouse hepatobiliary system.* Toxicologic pathology, 2010. **38**(7 suppl): p. 5S-81S.
170. Hashemi, R.H., W.G. Bradley, and C.J. Lisanti, *MRI: the basics*. 2012: Lippincott Williams & Wilkins.
171. Valls, C., et al., *Fat in the liver: diagnosis and characterization.* European radiology, 2006. **16**(10): p. 2292-2308.
172. Rummeny, E., et al., *Primary liver tumors: diagnosis by MR imaging.* American Journal of Roentgenology, 1989. **152**(1): p. 63-72.
173. Hennig, J., *Echoes—how to generate, recognize, use or avoid them in MR-imaging sequences. Part I: Fundamental and not so fundamental properties of spin echoes.* Concepts in Magnetic Resonance, 1991. **3**(3): p. 125-143.
174. Graham, S.J., P.L. Stanchev, and M.J. Bronskill, *Criteria for analysis of multicomponent tissue T2 relaxation data.* Magnetic Resonance in Medicine, 1996. **35**(3): p. 370-378.
175. Grau, V., et al., *Improved watershed transform for medical image segmentation using prior information.* IEEE Transactions on Medical Imaging, 2004. **23**(4): p. 447-458.
176. Yuan, Z., et al. *A novel automatic liver segmentation technique for MR images*. in *Proceedings - 2010 3rd International Congress on Image and Signal Processing, CISP 2010*. 2010.
177. Ma, Z., et al., *A review of algorithms for medical image segmentation and their applications to the female pelvic cavity.* Computer Methods in Biomechanics and Biomedical Engineering, 2010. **13**(2): p. 235-246.
178. Artan, Y., M.A. Haider, and I.S. Yetik. *Graph-based active contours using shape priors for prostate segmentation with MRI*. in *Biomedical Imaging: From Nano to Macro, 2011 IEEE International Symposium on*. 2011. IEEE.
179. Paradis, V. and P. Bedossa, *Definition and natural history of metabolic steatosis: histology and cellular aspects.* Diabetes & metabolism, 2008. **34**(6): p. 638-642.
180. Harrison, S.A. and B.A. Neuschwander-Tetri, *Nonalcoholic fatty liver disease and nonalcoholic steatohepatitis.* Clinics in liver disease, 2004. **8**(4): p. 861-879.

181. Sass, D.A., P. Chang, and K.B. Chopra, *Nonalcoholic fatty liver disease: a clinical review*. Digestive diseases and sciences, 2005. **50**(1): p. 171-180.
182. Brunt, E.M. *Nonalcoholic steatohepatitis*. in *Seminars in liver disease*. 2004. GEORG THIEME VERLAG.
183. McCullough, A.J., *The clinical features, diagnosis and natural history of nonalcoholic fatty liver disease.* Clin Liver Dis, 2004. **8**(3): p. 521-33, viii.
184. Cuadrado, A., et al., *Non-alcoholic steatohepatitis (NASH) and hepatocellular carcinoma.* Obesity surgery, 2005. **15**(3): p. 442-446.
185. Smedile, A. and E. Bugianesi, *Steatosis and hepatocellular carcinoma risk.* European review for medical and pharmacological sciences, 2005. **9**(5): p. 291.
186. Guiu, B., et al., *Quantification of liver fat content: comparison of triple-echo chemical shift gradient-echo imaging and in vivo proton MR spectroscopy.* Radiology, 2009. **250**(1): p. 95-102.
187. Thomas, E.L., et al., *Hepatic triglyceride content and its relation to body adiposity: a magnetic resonance imaging and proton magnetic resonance spectroscopy study.* Gut, 2005. **54**(1): p. 122-127.
188. Westphalen, A.C., et al., *Liver Fat: Effect of Hepatic Iron Deposition on Evaluation with Opposed-Phase MR Imaging 1.* Radiology, 2007. **242**(2): p. 450-455.
189. Springer, F., et al., *Liver fat content determined by magnetic resonance imaging and spectroscopy.* World Journal of Gastroenterology : WJG, 2010. **16**(13): p. 1560-1566.
190. Guiu, B., et al., *Quantification of Liver Fat Content: Comparison of Triple-Echo Chemical Shift Gradient-Echo Imaging and in Vivo Proton MR Spectroscopy 1.* Radiology, 2009. **250**(1): p. 95-102.
191. Reeder, S.B., et al., *Quantification of hepatic steatosis with MRI: the effects of accurate fat spectral modeling.* Journal of Magnetic Resonance Imaging, 2009. **29**(6): p. 1332-1339.
192. Serkova, N.J. and M.S. Brown, *Quantitative analysis in magnetic resonance spectroscopy: from metabolic profiling to in vivo biomarkers.* Bioanalysis, 2012. **4**(3): p. 321-341.
193. Shah, B., et al., *Quantitative MR imaging: physical principles and sequence design in abdominal imaging.* Radiographics, 2011. **31**(3): p. 867-880.
194. Hernando, D., et al., *Quantification of liver iron with MRI: State of the art and remaining challenges.* Journal of Magnetic Resonance Imaging, 2014. **40**(5): p. 1003-1021.
195. Kaldoudi, E. and S.C. Williams, *Relaxation time measurements in NMR imaging. Part I: Longitudinal relaxation time.* Concepts in Magnetic Resonance, 1993. **5**(3): p. 217-242.
196. Yuan, J., et al., *Observation of bi-exponential T1ρ relaxation of in-vivo rat muscles at 3T.* Acta Radiologica, 2012. **53**(6): p. 675-681.
197. Kjær, L., C. Thomsen, and O. Henriksen, *Evaluation of biexponential relaxation behaviour in the human brain by magnetic resonance imaging.* Acta Radiologica, 1989. **30**(4): p. 433-437.
198. Ma, J.F., *Dixon techniques for water and fat imaging.* Journal of Magnetic Resonance Imaging, 2008. **28**(3): p. 543-558.
199. Bernard, C.P., et al., *Comparison of fat quantification methods: A phantom study at 3.0T.* Journal of Magnetic Resonance Imaging, 2008. **27**(1): p. 192-197.
200. Horwitz, A.F., W.J. Horsley, and M.P. Klein, *Magnetic resonance studies on membrane and model membrane systems: Proton magnetic relaxation rates in*

sonicated lecithin dispersions. Proceedings of the National Academy of Sciences, 1972. **69**(3): p. 590-593.

201. Tesiram, Y.A., D. Saunders, and R.A. Towner, *Application of proton NMR spectroscopy in the study of lipid metabolites in a rat hepatocarcinogenesis model.* Biochimica Et Biophysica Acta-Molecular and Cell Biology of Lipids, 2005. **1737**(1): p. 61-68.
202. Menon, R., M. Rusinko, and P. Allen, *Multiexponential proton relaxation in model cellular systems.* Magnetic resonance in medicine, 1991. **20**(2): p. 196-213.
203. Saab, G., R.T. Thompson, and G.D. Marsh, *Multicomponent T2 relaxation of in vivo skeletal muscle.* Magnetic resonance in medicine, 1999. **42**(1): p. 150-157.
204. Wells, J.A., et al., *Measuring biexponential transverse relaxation of the ASL signal at 9.4 T to estimate arterial oxygen saturation and the time of exchange of labeled blood water into cortical brain tissue.* Journal of Cerebral Blood Flow & Metabolism, 2013. **33**(2): p. 215-224.
205. Chow, A.M., et al., *Measurement of liver T1 and T2 relaxation times in an experimental mouse model of liver fibrosis.* Journal of Magnetic Resonance Imaging, 2012. **36**(1): p. 152-158.
206. Cieszanowski, A., et al., *Characterization of focal liver lesions using quantitative techniques: comparison of apparent diffusion coefficient values and T2 relaxation times.* European radiology, 2012. **22**(11): p. 2514-2524.
207. Hazlewood, C.F., et al., *Nuclear magnetic resonance transverse relaxation times of water protons in skeletal muscle.* Biophysical Journal, 1974. **14**(8): p. 583.
208. Cole, W.C., A.D. Leblanc, and S.G. Jhingran, *The origin of biexponential T2 relaxation in muscle water.* Magnetic resonance in medicine, 1993. **29**(1): p. 19-24.
209. Bryant, N.D., et al., *Multi‐parametric MRI characterization of inflammation in murine skeletal muscle.* NMR in biomedicine, 2014. **27**(6): p. 716-725.
210. Scalera, J.E., et al., *Multiexponential T2 analyses in a murine model of hepatic fibrosis at 11.7 T MRI.* NMR in Biomedicine, 2013. **26**(1): p. 83-90.
211. D, N., *World Cancer Report* World Health Organisation, 2014: p. 404.
212. Welzel, T.M., et al., *Metabolic Syndrome Increases the Risk of Primary Liver Cancer in the United States: A Study in the SEER-Medicare Database.* Hepatology, 2011. **54**(2): p. 463-471.
213. Griffitts, J., et al., *In vivo MRS assessment of altered fatty acyl unsaturation in liver tumor formation of a TGFα/c-myc transgenic mouse model.* Journal of lipid research, 2009. **50**(4): p. 611-622.
214. Schnabl, B., et al., *Staging of fibrosis in experimental non-alcoholic steatohepatitis by quantitative molecular imaging in rat models.* Nuclear Medicine and Biology, 2016. **43**(2): p. 179-187.
215. Sharma, P., et al., *Measurement of liver fat fraction and iron with MRI and MR spectroscopy techniques.* Diagnostic and Interventional Radiology, 2014. **20**(1): p. 17.
216. Lau, J.K.C., X. Zhang, and J. Yu, *Animal models of non‐alcoholic fatty liver disease: current perspectives and recent advances.* The Journal of pathology, 2016.
217. Denda, A., et al., *Increased expression of cyclooxygenase-2 protein during rat hepatocarcinogenesis caused by a choline-deficient, l-amino acid-defined diet and chemopreventive efficacy of a specific inhibitor, nimesulide.* Carcinogenesis, 2002. **23**(2): p. 245-256.
218. Ma, J., *Dixon techniques for water and fat imaging.* Journal of Magnetic Resonance Imaging, 2008. **28**(3): p. 543-558.

219. Reeder, S.B. and C.B. Sirlin, *Quantification of liver fat with magnetic resonance imaging.* Magnetic resonance imaging clinics of North America, 2010. **18**(3): p. 337-357.

220. Masi, B., et al., *In Vivo MRI Assessment of Hepatic and Splenic Disease in a Murine Model of Schistosmiasis.* PLoS Negl Trop Dis, 2015. **9**(9): p. e0004036.

221. Mandel, J., *The statistical analysis of experimental data*. 2012: Courier Corporation.

222. Akaike, H., *Information theory and an extension of the maximum likelihood principle*, in *Selected Papers of Hirotugu Akaike*. 1998, Springer. p. 199-213.

223. Denda, A., et al., *Increased expression of cyclooxygenase-2 protein during rat hepatocarcinogenesis caused by a choline-deficient, L-amino acid-defined diet and chemopreventive efficacy of a specific inhibitor, nimesulide.* Carcinogenesis, 2002. **23**(2): p. 245-256.

224. Thoolen, B., et al., *Comparative histomorphological review of rat and human hepatocellular proliferative lesions.* Journal of toxicologic pathology, 2012. **25**(3): p. 189-199.

225. Hamilton, G., et al., *Effect of PRESS and STEAM sequences on magnetic resonance spectroscopic liver fat quantification.* Journal of Magnetic Resonance Imaging 2009. **30**(1): p. 145-52.

226. Thomsen, C., et al., *Quantification of liver fat using magnetic resonance spectroscopy.* Magn Reson Imaging, 1994. **12**(3): p. 487-95.

227. Ludden, T.M., S.L. Beal, and L.B. Sheiner, *Comparison of the Akaike Information Criterion, the Schwarz criterion and the F test as guides to model selection.* Journal of pharmacokinetics and biopharmaceutics, 1994. **22**(5): p. 431-445.

228. Chai, J.W., et al., *In vivo magnetic resonance (MR) study of fatty liver: importance of intracellular ultrastructural alteration for MR tissue parameters change.* Journal of Magnetic Resonance Imaging, 2001. **14**(1): p. 35-41.

229. Bernardino, M.E., et al., *Multiple NMR T2 relaxation values in human liver tissue.* American Journal of Roentgenology, 1983. **141**(6): p. 1203-1208.

230. Duvvuri, U., et al., *Quantitative T1ρ Magnetic Resonance Imaging of RIF-1 Tumors in Vivo Detection of Early Response to Cyclophosphamide Therapy.* Cancer research, 2001. **61**(21): p. 7747-7753.

231. Kuesel, A.C., et al., *Mobile lipids and metabolic heterogeneity of brain tumours as detectable by Ex Vivo1H MR spectroscopy.* NMR in Biomedicine, 1994. **7**(4): p. 172-180.

232. Rémy, C., et al., *Evidence that mobile lipids detected in rat brain glioma by 1H nuclear magnetic resonance correspond to lipid droplets.* Cancer research, 1997. **57**(3): p. 407-414.

233. Hakumäki, J.M., et al., *Quantitative 1H nuclear magnetic resonance diffusion spectroscopy of BT4C rat glioma during thymidine kinase-mediated gene therapy in vivo: identification of apoptotic response.* Cancer research, 1998. **58**(17): p. 3791-3799.

234. Margaret Cheng, H.L., et al., *Practical medical applications of quantitative MR relaxometry.* Journal of Magnetic Resonance Imaging, 2012. **36**(4): p. 805-824.

235. Vaughan, J.T., et al., *7T vs. 4T: RF power, homogeneity, and signal ‐ to ‐ noise comparison in head images.* Magnetic resonance in medicine, 2001. **46**(1): p. 24-30.

236. Healy, J. and R. Reznek, *The peritoneum, mesenteries and omenta: normal anatomy and pathological processes.* European radiology, 1998. **8**(6): p. 886-900.

237. Ferizi, U., et al., *White matter compartment models for in vivo diffusion MRI at 300 mT/m.* NeuroImage, 2015. **118**: p. 468-483.

238. Winfield, J.M., et al., *Modelling DW-MRI data from primary and metastatic ovarian tumours.* European radiology, 2015. **25**(7): p. 2033-2040.

239. Juras, V., et al., *Quantitative MRI analysis of menisci using biexponential T2* fitting with a variable echo time sequence.* Magnetic resonance in medicine, 2014. **71**(3): p. 1015-1023.

240. McPherson, S., et al., *Magnetic resonance imaging and spectroscopy accurately estimate the severity of steatosis provided the stage of fibrosis is considered.* Journal of hepatology, 2009. **51**(2): p. 389-397.

241. Bergers, G. and L.E. Benjamin, *Tumorigenesis and the angiogenic switch.* Nature reviews cancer, 2003. **3**(6): p. 401-410.

242. Bonkovsky, H.L., *Iron and the liver.* The American journal of the medical sciences, 1991. **301**(1): p. 32-43.

243. Eguchi, A., et al., *Adenomatous hyperplasia in the vicinity of small hepatocellular carcinoma.* Hepatology, 1992. **15**(5): p. 843-8.

244. Terada, T., et al., *Fatty macroregenerative nodule in non-steatotic liver cirrhosis. A morphologic study.* Virchows Arch A Pathol Anat Histopathol, 1989. **415**(2): p. 131-6.

245. Yu, J.-S., et al., *Fat-containing nodules in the cirrhotic liver: chemical shift MRI features and clinical implications.* American Journal of Roentgenology, 2007. **188**(4): p. 1009-1016.

246. Choi, J.-Y., J.-M. Lee, and C.B. Sirlin, *CT and MR imaging diagnosis and staging of hepatocellular carcinoma: part II. Extracellular agents, hepatobiliary agents, and ancillary imaging features.* Radiology, 2014. **273**(1): p. 30-50.

Appendix

For T_2 mapping using MATLAB, a single script including two functions was used: a) Function for mono-exponential model, and b) Function for bi-exponential model.

Main script

```
% addpath('/home/s4219677/matlab/NIfTI_20140122'); % this tells matlab where the functions are that you want to use.

 %-----------------------
% Specify graph options: 0 means not using the option, 1 means using the option
---------------
  figure_savedir = '~/Desktop/benfitting/';
plot_ 50_vs _ 130 = 0;
plot_me _vs _be = 1;
mnexp_opts.plot_fit = 1;
biexp_opts.plot_fit = 1;
mnexp_opts.plot_components=0; % This plots T2L and T2 short and their sum
biexp_opts.plot_components=0; % This plots T2L and T2 short and their sum
disp_best _params = 1; % display values in matlab window
parr_proc = 0;  % can't do parallel processing if you want to debug or plot
 n_procs= 10;
estimate_noise = 0;

%-----------------------
% Specify monoexp and biexp specific option
   %-----------------------


   n_params _me = 3+1;
  n_params _be = 5+1;


  mnexp_opts.fit = 1;
```

```
 biexp_opts.fit = 1;
 mnexp_opts.include_offset = 1;
 biexp_opts.include_offset = 1;
 mnexp_opts.Algorithm = 'Trust-Region';
 biexp_opts.Algorithm = 'Trust-Region';

 biexp_opts.usef = 1; % 0 means not using f
  reorganise_biexp = 1;

 % Constraints
  mnexp_opts.StartPoint = [50 4000 0];                % T2M S0 C
  mnexp_opts.Lower = [1 0 0];
 mnexp_opts.Upper = [211 inf inf ];
 if biexp_opts.usef
      biexp_opts.StartPoint = [10 70 0.7 4000 0];     % T2S T2L f S0 C
      biexp_opts.Lower = [1 1 0 0 0];
    biexp_opts.Upper = [100 211 1 inf inf];
 else
      biexp_opts.StartPoint = [10 70 4000 4000 0];    % T2S T2L S0S S0L C
      biexp_opts.Lower = [1 1 0 0 0];
    biexp_opts.Upper = [100 211 inf inf inf];
 end

  biexp_opts.biexpFixedParams_from_mnexp = 0; % this sets S0 and C and doesnt allow them to vary
  biexp_opts.biexpStartPoint_from_mnexp = 1; % this sets starting point for S0, C, T2L and T2S from monexponential
  data_driven _startpoint = 1; % This sets S0 and C (monexponential and biexponential)

  %-----------------------
  % Specify input and output
  %-----------------------
```

```
    save_img = 0; % e.g im MIPAV

    % data_dir _base = '/home/s4219677/Documents/MCD.MIPAV';
   data_dir _base = '/data/dumu/brereton/s4219677/MCD.MIPAV';

  identifier = 'T2';
  % identifier = 'T2CA'; % with contrast agent
   study_dir = 'Optimisation_TR _Constraints _DDSP _BEfromME _f _validate';

   subjects = {'CON3'};
  %   subjects = {'MCD4' 'MCD1' 'MCD2' 'MCD3'  'MCD5' 'MCD6' 'CON1' 'CON2' 'CON3'
'CON4' 'CON5' 'CON6' };
  weeks = {'24'};
  %   weeks = {'12' '24' '32' '4' '8' '40'};

  % specify maps you want to save
   % DO NOT change names, these names are hard-coded later in the script
     SaveImgNames = cell(0);
  if mnexp_opts.fit
        SaveImgNames = [SaveImgNames, {'T2M_map _me','S0_map _me','C_map
_me','RSquare_map _me','AIC_map _me'}];
  end
    if biexp_opts.fit
        SaveImgNames = [SaveImgNames, {'T2L_map _be','T2S_map _be','T2min_map
_be','T2max_map _be','RSquare_map _be','AIC_map _be','AIC_map _diff'}];
      if biexp_opts.usef
            SaveImgNames = [SaveImgNames, {'f_map _be', 'S0_map _be'}];
      else
            SaveImgNames = [SaveImgNames, {'S0S_map _be', 'S0L_map _be'}];
      end
    end

    % select what region you want to calculate the T2 for
```

```
      region_of _interest = 'single_voxel';
  % region_of _interest = 'roi';
  %   region_of _interest = 'all_voxels';
  % region_of _interest = 'MIPAV';

  if strcmp(region_of _interest,'single_voxel')
      % vox_of _interest = [86,110,16]; % This voxel is bad for {noC,noD}, but good for {C, noD}
      % vox_of _interest = [111,115,20]; % This voxel is bad for {C,noD}, but good for {C, D}
    vox_of _interest = [73,123,21];
     % vox_of _interest = [121,100,14];
  elseif strcmp(region_of _interest,'roi')
      roi_name _ext = '_nmask';
     roi_name _ext = '_mask';
  elseif strcmp(region_of _interest,'time_series')
      MIPAV_signal = [35 23 15 10 6 4 3 2 1 1 1 1 1];
  end

   %   TE_unwanted = [5,60:10:130];
    TE_unwanted = [5,60:20:120];
  % TE_unwanted = [];



   %------------------------------------------------------------------------
    %------------------------------------------------------------------------
    % Step 1: read in data
     %------------------------------------------------------------------------
    %------------------------------------------------------------------------

    data_dir _CON = fullfile(data_dir _base,'control');
  data_dir _MCD = fullfile(data_dir _base,'treated');

  n_sub = length(subjects);
```

```
n_weeks = length(weeks);

if parr_proc
     poolobj = parpool(n_procs); % this has changed acording to new matlab software
 %     matlabpool(n_procs);

end

  %------------------
  % loop over subjects
  %------------------
  for i_sub=1:n_sub



       tstart=tic;
    sub_name = subjects{i_sub};
    % select correct directory depending on whether subject name includes
      % CON or MCD
      if strfind(sub_name,'CON')
          data_dir _all = data_dir _CON;
    elseif strfind(sub_name,'MCD')
          data_dir _all = data_dir _MCD;
    end

      for i_week = 1:n_weeks


            try % try for week


            week_name = ['WEEK',weeks{i_week}];
        week_number = week_name(5:end);


        %-----------
          % read in data
```

```
   %-----------
  data_dir _sub = fullfile(data_dir _all,sub_name,week_name);

data_name = [sub_name,'_',identifier,'W',week_number];
% data_name = dir(data_dir _sub,'*T2*');
data_fname = fullfile(data_dir _sub,[data_name,'.nii']);
disp(data_fname);

% read in mask
  mask_dir = data_dir _sub;
mask_name = [data_name,'_mask'];
try
      mask_tmp = load_nii(fullfile(mask_dir,[mask_name,'.nii'])); % mask
      mask_tmp = flip_img(mask_tmp);
catch ME
     disp(ME.message)
     continue;
end
  mask_img = double(mask_tmp.img);

save_dir = [data_dir _sub,'/',study_dir];
if ~exist(save_dir,'dir')
     mkdir(save_dir);
end



  % read in roi
  if strcmp(region_of _interest,'roi')
      roi_dir = data_dir _sub;
    roi_name = [data_name,roi_name _ext];
    try
          roi_tmp = load_nii(fullfile(roi_dir,[roi_name,'.nii'])); % roi
          roi_tmp = flip_img(roi_tmp);
```

```
    catch ME
        disp(ME.message)
        continue;
    end
      roi_img = double(roi_tmp.img);

end


  % read in T2 weighted image
  try
      data_tmp = load_nii(data_fname); % this line reads in the image data
      % load_nii.m flips image in x and y dimensions. Need to Flip back.
       data_tmp = flip_img(data_tmp);
catch ME
     disp(ME.message); % display error meassage
     continue; % break from for loop and go onto next week if T2 image not found
  end


  % extract/specify image dimensions.
   n_x = data_tmp.hdr.dime.dim(2);
n_y = data_tmp.hdr.dime.dim(3);
n_slices _ 4D = data_tmp.hdr.dime.dim(4);

if n_slices _ 4D==240
       n_slices = 24;
    n_TE = 10; % number of TE in raw data
      TE = [5:5:50];
elseif n_slices _ 4D==360
       n_slices = 20;
    n_TE = 18; % nt = number of TEs points
       TE = [5:5:50,60:10:130];
```

```
elseif n_slices _ 4D==260
      n_slices = 26;
   n_TE = 10;
   TE = [5:5:50];
elseif n_slices _ 4D==432
      n_slices = 24;
   n_TE = 18;
   TE = [5:5:50,60:10:130];
elseif n_slices _ 4D==960
      n_slices = 24;
   n_TE = 40;
   TE = [5:5:200];
elseif n_slices _ 4D==1040
      n_slices = 26;
   n_TE = 40;
   TE = [5:5:200];
elseif n_slices _ 4D==312 % T2star
      n_slices = 26;
   n_TE = 12;
   TE = [4:6:70];
end
  n_voxels = n_x*n_y*n_slices;


%---------------------------------------------------------------------------
   %---------------------------------------------------------------------------
   % Step 2: create time series for each voxel
    %---------------------------------------------------------------------------
   %---------------------------------------------------------------------------


   signal = zeros(n_x,n_y,n_slices,n_TE);
signal_std = zeros(n_x,n_y,n_slices,n_TE);
```

```
% loop over echo times to put 3D data into 4D (time) matrix
 for i_slice=1:n_slices
     % signal(:,:,1,:) = data_tmp.img(:,:,1:18);
   % signal(:,:,2,:) = data_tmp.img(:,:,19:36);
   % signal(:,:,3,:) = data_tmp.img(:,:,37:48);

   signal(:,:,i_slice,:) = data_tmp.img(:,:,(i_slice-1)*n_TE +1 : i_slice*n_TE);

end

 signal_original = signal;

%-------------------------------------------------------------------------
  %-------------------------------------------------------------------------
  % Step 3: Get rid of unwanted TE
   %-------------------------------------------------------------------------
  %-------------------------------------------------------------------------

  [C,ind_unwanted,IB] = intersect(TE,TE_unwanted); % this finds the indices of TE which include the unwanted times specificed in TE_unwanted

 signal(:,:,:,ind_unwanted) = [];    % Get rid of the signal at bad TEs
 TE_wanted = TE;                     % create new TE vector called TE_wanted
 TE_wanted(ind_unwanted) = [];       % get rid of bad TEs
 n_TE _wanted = length(TE_wanted);
TE_wanted _highres=[0:0.1:max(TE_wanted)];

 %------------------------------------
 % calculate noise from image
 %------------------------------------
 if estimate_noise
    noisemask_dir = data_dir _sub;
   noisemask_tmp = load_nii(fullfile(noisemask_dir,'BENMASK_noise.nii')); % mask
```

```
        noisemask_img = double(noisemask_tmp.img);

       ind_mask = find(noisemask_img);
       for i_TE=1:n_TE _wanted
           noise(:,:,:,i_TE) = signal (:,:,:,i_TE) .* noisemask_img; % this multiplies the signal by the mask (0,1)
        end
        avg_noise = mean(noise(find(noise))); % get noise in voxels which are non-zero (ROI), then take mean over x,y,z,TE
      end

      %-----------------------------------------------
      % Mask the T2 weighted image
      %-----------------------------------------------
      for i_TE=1:n_TE _wanted
         signal(:,:,:,i_TE) = signal (:,:,:,i_TE) .* mask_img; % this multiplies the signal by the mask (0,1)
      end

      % get list of voxels equal to one (i.e. inside the mask)
      ind_mask = find(mask_img);
     n_voxels _mask = length(ind_mask);
     n_voxels _loop = n_voxels _mask;

     %----------------
      % instantiate images
      %----------------
      if save_img
        for i_img _save=1:length(SaveImgNames)
           SaveImgNames_tmp = SaveImgNames{i_img _save};
         eval([SaveImgNames_tmp,'= zeros(1,n_voxels _mask);']);
       end
      end
```

```
 %----------------
 % Specify/create input voxels
 %----------------
 if strcmp(region_of _interest,'all_voxels')

   ind_voi = ind_mask;

elseif strcmp(region_of _interest,'single_voxel')

   vox_of _interest = vox_of _interest + 1;  % to convert between fslview/mipav and matlab coordinates
   ind_voi = sub2ind(size(mask_img),vox_of _interest(1),vox_of _interest(2),vox_of _interest(3));

elseif strcmp(region_of _interest,'roi')

   inds_voi = find(roi_img);
  % get mean voxel location
    [x_inds,y_inds,z_inds] = ind2sub(size(roi_img),inds_voi);
  x_mean = ceil(mean(x_inds)); y_mean = ceil(mean(y_inds)); z_mean = ceil(mean(z_inds));
  ind_voi = sub2ind(size(roi_img),x_mean,y_mean,z_mean);
  n_voxels _loop = length(ind_voi);

  for i_TE=1:n_TE _wanted
      signal(:,:,:,i_TE) = signal (:,:,:,i_TE) .* roi_img; % this multiplies the signal by the mask (0,1)
   end
   % set all voxels to zero, other than the mean location, set to
      % mean signal in ROI
      for i_TE=1:n_TE _wanted
         signal_ 3D =  signal(:,:,:,i_TE);
```

```
            signal(:,:,:,i_TE) = 0;
            signal(x_mean,y_mean,z_mean,i_TE) = mean(signal_ 3D(inds_voi));
            signal_std(x_mean,y_mean,z_mean,i_TE) = std(signal_ 3D(inds_voi));
          end

        end
        n_voxels _loop = length(ind_voi);


       %------------------------------
        % NEED TO CHANGE THIS IF DOING PARRALLEL PROCESSING
        %------------------------------
    %          parfor i_ind=1:n_voxels _loop
           for i_ind=1:n_voxels _loop

              try % try for voxel

              % initiate structures (required for parfor)
              fixed_params = struct;
          mnexp_params = struct;
          mnexp_opts _tmp = mnexp_opts;
          biexp_opts _tmp = biexp_opts;

          %-----------------------------------
            % extract signal at voxel
            %-----------------------------------
            i_voxel = ind_voi(i_ind);
          % disp(['ind: ',num2str(i_ind),' voxel: ',num2str(i_voxel)]);
          [i_x,i_y,i_z] = ind2sub(size(mask_img),i_voxel); % this converts a 1D index into a
3D subscript
          % extract signal from single voxel
          signal_voxel = squeeze(signal(i_x,i_y,i_z,:));
        signal_voxel _original = squeeze(signal_original(i_x,i_y,i_z,:));
```

```
        if strcmp(region_of _interest,'roi')
           signal_std _voxel = squeeze(signal_std(i_x,i_y,i_z,:));
        end



         %-----------------------------------
         % Set data driven startpoint
         %-----------------------------------
         if data_driven _startpoint
           mnexp_opts _tmp.StartPoint(2) = 1.1*signal_voxel(1); % S0;  signal_voxel(1)=
first data point
            mnexp_opts _tmp.StartPoint(3) = signal_voxel(end); % C; signal_voxel(end)=
last data point

            if ~biexp_opts.biexpStartPoint_from_mnexp % if were not getting biexp
startpoint from mnexp fitting
              biexp_opts _tmp.StartPoint(4) = 1.1*signal_voxel(1); % S0
             biexp_opts _tmp.StartPoint(5) = signal_voxel(end); % C
            end
          end

          %-----------------------------------
          % calculate noise from image
          %-----------------------------------

          %-----------------------------------------------------------------
         %-----------------------------------------------------------------
         % Step 4: Fit mn-exponential curve to each voxel
          %-----------------------------------------------------------------
         %-----------------------------------------------------------------
         if mnexp_opts.fit

             [bfp_me,gof_me,coeff_names            _me,fitresult_me]          =
```

```
fit_monoexponential(TE_wanted',signal_voxel,mnexp_opts _tmp);
          RSS_me = gof_me.sse;
          AIC_me = n_TE _wanted * log(RSS_me/n_TE_wanted) + 2 * n_params _me;



          T2M_me _ind = find(strcmp(coeff_names _me,'T2M'));
          S0_me _ind = find(strcmp(coeff_names _me,'S0'));
          C_me _ind = find(strcmp(coeff_names _me,'C'));

          T2M_me = bfp_me(T2M_me _ind);
          S0_me = bfp_me(S0_me _ind);
          C_me = bfp_me(C_me _ind);

          if disp_best _params
             disp(['T2M: ',num2str(bfp_me(T2M_me _ind))]);
            disp(['S0: ',num2str(bfp_me(S0_me _ind))]);
            disp(['C: ',num2str(bfp_me(C_me _ind))]);
          end




           if plot_ 50_vs _ 130
              TE_wanted _ 50_inds = find(TE_wanted<=50);
            TE_wanted _ 50 = TE_wanted(TE_wanted _ 50_inds);
            signal_voxel _ 50 = signal_voxel(TE_wanted _ 50_inds);
            [bfp_me _ 50,gof_me _ 50,coeff_names _me _ 50,fitresult_me _ 50] =
fit_monoexponential(TE_wanted _ 50',signal_voxel _ 50,mnexp_opts _tmp);



           model_me = feval(fitresult_me,TE_wanted _highres);
           model_me _ 50 = feval(fitresult_me _ 50,TE_wanted _highres);


           h=figure;
```

```
        hold on;

        plot(TE_wanted,signal_voxel,'k.','markersize',20);
        plot(TE_wanted _highres,model_me, 'r-','linewidth',5);
        plot(TE_wanted _highres,model_me _ 50,'g-','linewidth',5);
        if strcmp(region_of _interest,'roi')
            errorbar(TE_wanted,signal_voxel,signal_std _voxel,'k.');
        end
         hold on;
        legend( 'signal', '13 TEs', '9 TEs' );
        xlabel( 'TE' ,'fontsize',24);
        ylabel( 'Signal Intensity','fontsize',24 );
        % title([sub_name,' ',week_name,': mn-exponential']);
        if strcmp(region_of _interest,'single_voxel')
             title_str = [subjects{i_sub},', mnexponential, voxel: [' num2str(vox_of
_interest(1)),',',num2str(vox_of _interest(2)),',',num2str(vox_of _interest(3)),']'];
        elseif strcmp(region_of _interest,'roi')
             title_str = [subjects{i_sub},', mnexponential, ',roi_name];
        end

         title(title_str,'fontsize',16);
        set(gca,'fontsize',20);
        hold off;
        saveas(h,fullfile(figure_savedir,title_str),'fig');
        saveas(h,fullfile(figure_savedir,title_str),'jpg');
     end


    end % if fit_mnexp

    %-----------------------------------------------
    % Step 4: Fit bi-exponential curve to each voxel
      %-----------------------------------------------
```

```
if biexp_opts.fit

   if biexp_opts.biexpFixedParams_from_mnexp | biexp_opts.biexpStartPoint_from_mnexp  % retrieve best fit parameters from mnexponential

     T2M_me _ind = find(strcmp(coeff_names _me,'T2M'));
   S0_me _ind = find(strcmp(coeff_names _me,'S0'));
   C_me _ind = find(strcmp(coeff_names _me,'C'));

   T2M_me = bfp_me(T2M_me _ind);
   S0_me = bfp_me(S0_me _ind);
   if mnexp_opts.include_offset
       C_me = bfp_me(C_me _ind);
   end

 end

   if biexp_opts.biexpFixedParams_from_mnexp    % specify fixed parameters (taken from mnexponential)

    fixed_params.S0 = S0_me;
   if biexp_opts.include_offset
       if mnexp_opts.include_offset
           fixed_params.C = C_me;
     else
          disp('error: you have asked to fix biexponential offset from mnexponential without including offset in mnexponential');
     end

    end
 end
```

```
          if biexp_opts.biexpStartPoint_from_mnexp    % specify starting parameters for
biexponential (taken from mnexponential)
            biexp_opts _tmp.StartPoint(1)=0.5*T2M_me;       % T2S
            biexp_opts _tmp.StartPoint(2)=1.5*T2M_me;       % T2L
            if biexp_opts.usef
              biexp_opts _tmp.StartPoint(4)=S0_me;
           else
              biexp_opts _tmp.StartPoint(3)=S0_me/2;      % S0S
              biexp_opts _tmp.StartPoint(4)=S0_me/2;      % S0L
            end
            if biexp_opts.include_offset
              biexp_opts _tmp.StartPoint(5)=C_me;         % C
            end
          end

          % fit model to data
          if biexp_opts.biexpFixedParams_from_mnexp
             [bfp_be,gof_be,coeff_names _be,fitresult_be] =
fit_biexponential(TE_wanted',signal_voxel,biexp_opts _tmp,fixed_params);
         else
            [bfp_be,gof_be,coeff_names _be,fitresult_be] =
fit_biexponential(TE_wanted',signal_voxel,biexp_opts _tmp);
         end

          T2S_be _ind = find(strcmp(coeff_names _be,'T2S'));
         T2L_be _ind = find(strcmp(coeff_names _be,'T2L'));
         f_be _ind = find(strcmp(coeff_names _be,'f'));
         S0_be _ind = find(strcmp(coeff_names _be,'S0'));
         S0S_be _ind = find(strcmp(coeff_names _be,'S0S'));
         S0L_be _ind = find(strcmp(coeff_names _be,'S0L'));
         C_be _ind = find(strcmp(coeff_names _be,'C'));
```

```
         RSS_be = gof_be.sse;
         AIC_be = n_TE _wanted * log(RSS_be/n_TE_wanted) + 2 * n_params _be;


         if disp_best _params
            disp(['T2S: ',num2str(bfp_be(T2S_be _ind))]);
           disp(['T2L: ',num2str(bfp_be(T2L_be _ind))]);
           if biexp_opts.usef
              disp(['S0: ',num2str(bfp_be(S0_be _ind))]);
             disp(['f: ',num2str(bfp_be(f_be _ind))]);
           else
              disp(['S0S: ',num2str(bfp_be(S0S_be _ind))]);
             disp(['S0L: ',num2str(bfp_be(S0L_be _ind))]);
           end

            disp(['C: ',num2str(bfp_be(C_be _ind))]);
         end

        end % fit biexponential

        %-----------------------------------------------
        % Step 5: Compare mn-exponential and bi-exponential, compare R^2, compare
Aikikes Information Criterion
        %-----------------------------------------------
        % AIC = -2*LL + 2*k; % LL = log likelhood, k=number of parameters
         % LL = ln ( p(model | parameters, data) ) ;


       if plot_me _vs _be

          model_me = feval(fitresult_me,TE_wanted _highres);
         model_be = feval(fitresult_be,TE_wanted _highres);
```

```
          h=figure;
          hold on;
          plot(TE_wanted,signal_voxel,'k.','markersize',16);
          plot(TE_wanted _highres,model_me,'r-','linewidth',1.5);
          plot(TE_wanted _highres,model_be,'g-','linewidth',1.5);
          if strcmp(region_of _interest,'roi')
                errorbar(TE_wanted,signal_voxel,signal_std _voxel,'k.');
          end
           hold on;
          legend( 'signal','mn-exponential', 'bi-exponential');
          xlabel( 'TE' ,'fontsize',16);
          ylabel( 'Signal Intensity','fontsize',16 );
          % title([sub_name,' ',week_name,': mn-exponential']);

          if strcmp(region_of _interest,'single_voxel')
              title_str = [subjects{i_sub},', me vs be, voxel: [' num2str(vox_of
_interest(1)),',',num2str(vox_of _interest(2)),',',num2str(vox_of _interest(3)),']'];
          elseif strcmp(region_of _interest,'roi')
              title_str = [subjects{i_sub},', me vs be, ',roi_name];
          end

           title(title_str,'fontsize',16);
          set(gca,'fontsize',16);
          hold off;
          saveas(h,fullfile('~/Desktop/benfitting/',title_str),'fig');
          saveas(h,fullfile('~/Desktop/benfitting/',title_str),'jpg');
        end

          %-----------------------------------------------
          % Step 6: Fill T2_maps image with T2 values
          %-----------------------------------------------

          if mnexp_opts.fit
```

```
   S0_map _me(i_ind) = bfp_me(S0_me _ind);
 T2M_map _me(i_ind) = bfp_me(T2M_me _ind);
 RSquare_map _me(i_ind) = gof_me.rsquare;
 AIC_map _me(i_ind) = AIC_me;
 ftest_me(i_ind)=F_me;
 if mnexp_opts.include_offset
     C_map _me(i_ind) = bfp_me(C_me _ind);
 end

end

if biexp_opts.fit

   if biexp_opts.usef
     f_map _be(i_ind) = bfp_be(f_be _ind);
 else
     S0S_map _be(i_ind) = bfp_be(S0S_be _ind);
   S0L_map _be(i_ind) = bfp_be(S0L_be _ind);
 end

     T2S_map _be(i_ind) = bfp_be(T2S_be _ind);
 T2L_map _be(i_ind) = bfp_be(T2L_be _ind);
 RSquare_map _be(i_ind) = gof_be.rsquare;
 AIC_map _be(i_ind) = AIC_be;
 ftest_be(i_ind)=F_be;

 if ~biexp_opts.biexpFixedParams_from_mnexp
     S0_map _be(i_ind) = bfp_be(S0_be _ind);
   if biexp_opts.include_offset
       C_map _be(i_ind) = bfp_be(C_be _ind);
   end
  end
```

```
 end


 catch ME % line 244

     disp(['error for voxel: ',num2str(i_x),',',num2str(i_y),',',num2str(i_z)]);

    if mnexp_opts.fit
          disp(ME.message)
          T2M_map _me(i_ind) = nan;
        S0_map _me(i_ind) = nan;
        C_map _me(i_ind) = nan;
        RSquare_map _me(i_ind) = nan;
        AIC_map _me(i_ind) = nan;
    end
      if biexp_opts.fit
          T2_map _be _ 1(i_ind) = nan;
        T2_map _be _ 2(i_ind) = nan;
        T2S_map _be(i_ind) = nan;
        T2L_map _be(i_ind) = nan;
        RSquare_map _be(i_ind) = nan;
        AIC_map _be(i_ind) = nan;
    end
    end


end % loop over voxels



%-----------------------------------------------
% get diffrerence in AIC
%-----------------------------------------------
```

```
        if mnexp_opts.fit & biexp_opts.fit
          AIC_map _diff = AIC_map _be - AIC_map _me; % if positive ==> AIC me is lower, if negative AIC be is lower
        end

        %----------------------------------------------
        % Step 6: reorgaise biexponential components
        %----------------------------------------------
        if reorganise_biexp & biexp_opts.fit
          % initiate output images
          T2max_map _be = zeros(size(T2L_map _be));
        T2min_map _be = zeros(size(T2L_map _be));

        % get maximum (of the two compnents) T2M value and put it in T2M_map _max, and take minimum and put in T2M_map _min
          T2max_map _be = max(T2L_map _be,T2S_map _be);
        T2min_map _be = min(T2L_map _be,T2S_map _be);
      end

       %----------------------------------------------
       % Step 7: Convert Vectors to Images and save
       %----------------------------------------------

       if save_img

           save_dir = [data_dir _sub,'/',study_dir];
        if ~exist(save_dir,'dir')
            mkdir(save_dir);
        end

         for i_img _save=1:length(SaveImgNames)

             SaveImgNames_tmp = SaveImgNames{i_img _save};
```

```
          disp(['saving ',SaveImgNames_tmp]);
          ImgSave = zeros(1,n_voxels);
          eval(['ImgSave(ind_mask) = ',SaveImgNames_tmp,';']); % ind_mask gives the voxel indices in the full image
           ImgSave = reshape(ImgSave,n_x,n_y,n_slices); % this turns a 1D vector into a 3D images
           TempImg = mask_tmp;
          TempImg.img = ImgSave;
          TempImg.hdr.dime.datatype = 64;
          TempImg.hdr.dime.bitpix = 64;
          save_nii(TempImg,fullfile(save_dir,[SaveImgNames_tmp,'.nii']));
          clear ImgSave TempImg;

        end
       end % if save_img

       telapsed=toc(tstart);
      disp(['telspased: ',num2str(telapsed)]);0.5



     catch ME % try for weeks
      disp(ME.message);
    end



     end % loop over weeks



  end % loop over subjects


  if parr_proc
     matlabpool close;
 end
```

----

a) Function to fit mono-exponential model

```
function [ bfp,gof,coeff_names,fitresult ] = fit_monexponential( TE,signal,mnexp_opts)

    if mnexp_opts.include_offset
        ft = fittype( @(T2M,S0,C,x) S0*exp(-x/T2M) + C);
    else
        ft = fittype( @(T2M,S0,x) S0*exp(-x/T2M) );
    end

    opts = fitoptions( ft );
    opts.StartPoint = mnexp_opts.StartPoint; %[C S0_ 1 R21]
    opts.Display = 'Off';
    opts.Algorithm = mnexp_opts.Algorithm;


    if strcmp(mnexp_opts.Algorithm,'Trust-Region')
        if isfield(mnexp_opts,'Lower')
            opts.Lower = mnexp_opts.Lower;
        end
        if isfield(mnexp_opts,'Upper')
            opts.Upper = mnexp_opts.Upper;
        end
    end


    % Fit model to data.
       [fitresult, gof] = fit( TE, signal, ft, opts ); % "_me" means mnexponential
    bfp = coeffvalues(fitresult); % bfp = bestfit parameters;
```

```
    coeff_names = coeffnames(fitresult);
    % plot best fit parameters
    if mnexp_opts.plot_fit

        model = feval(fitresult,TE); % should equal betot;
        me1 = bfp(2) * exp(-TE/bfp(1));
        metot = me1 + bfp(3);

        figure;
        hold on;

        h(1)=plot( TE, signal,'k.');
        h(2)=plot( TE, model,'b-');
        if mnexp_opts.plot_components
            h(3)=plot( TE, me1,'r--','linewidth',1.5 );
            h(4)=plot( TE, repmat(bfp(3),[1,length(TE)]),'c--', 'linewidth',1.5);
        end

        legend( h, 'signal', 'model fit', 'T2', 'C' );
        % Label axes
        xlabel( 'TE','fontsize',16 );
        ylabel( 'Signal Intensity','fontsize',16 );
        % title([sub_name,' ',week_name,': bi-exponential']);
        title('mnexponential','fontsize',16);
        set(gca,'fontsize',16);
        hold off;
    end

end
```

---

b) Function for bi-exponential model

```
function [ bfp,gof,coeff_names,fitresult] = fit_biexponential(varargin)
    approx_T2L=0;
    %---------
     % Assign Varargin
    %---------

       TE = varargin{1};
    signal = varargin{2};
    if nargin>2
        biexp_opts = varargin{3};
    end
    if nargin>3
        fixed_params = varargin{4};
        C_fixed = fixed_params.C;
        S0_fixed = fixed_params.S0;
    end

    %---------
      % Step 1: estimate initial values of S0, f, R21 and R2star
    %---------

     %---------
     % estimate R21 by fiting a monoexponential to high TE
    % values > 60 (Equation 3)
    % Here we tried to reduce the redundancy between free parameters by
    % forcing a sensible strating point. This involved fitting a
    % monoexponential to the last few data points and assuming the
    % resulting T2 was T2L. It didn't work because the last few data points
    % are too noisy.
       %---------
     if approx_T2L
        inds_long = find(TE_long>=60);
        TE_long = TE_wanted(inds_long);
```

```
        signal_voxel _long = signal_voxel(inds_long);
        [TE_wanted, yData] = prepareCurveData( TE_long', signal_voxel _long );
        if include_offset
            ft = fittype( 'S0_ 1*exp(-x*R21) + C', 'independent', 'x', 'dependent', 'y' );
            opts = fitoptions( ft ); % this line must go before setting any other options
            n_params = 3+1;
            opts.StartPoint = [0  1/50 4000]; %[C S0_ 1 R21]
        else
            ft = fittype( 'S0_ 1*exp (-x*R21)', 'independent', 'x', 'dependent', 'y' );
            opts = fitoptions( ft );
            n_params = 2+1;
            opts.StartPoint = [ 1/50 4000]; %[C S0_ 1 R21]
        end
        % Fit model to data.
           [fitresult_long, gof_long] = fit( TE_wanted', yData, ft, opts ); % "" means monoexponential
        bfp_long = coeffvalues(fitresult_long); % bfp = bestfit parameters;
        Shigh = bfp_long(1);nted
        D = bfp_long(2);
    end
    %---------
      % Step 2: fit biexponential using initial values of S0, f, R21 and R2star
    %---------

     if exist('fixed_params','var')
        if biexp_opts.usef
            if biexp_opts.include_offset
                ft = fittype( @(T2S,T2L,f,x) S0_fixed * ( f*exp(-x/T2S) + (1-f)*exp(-x/T2L) ) + C_fixed );
            else
                ft = fittype( @(T2S,T2L,f,x) S0_fixed * ( f*exp(-x/T2S) + (1-f)*exp(-x/T2L) ) );
            end
        else
```

```
         if biexp_opts.include_offset
            ft = fittype( @(T2S,T2L,x)  S0S_fixed*exp(-x/T2S) + S0L_fixed*exp(-x/T2L)  +
C_fixed );
         else
            ft = fittype( @(T2S,T2L,x)   S0S_fixed*exp(-x/T2S) + S0L_fixed*exp(-x/T2L)  );
         end
      end
   else
      if biexp_opts.usef
         if biexp_opts.include_offset
            ft = fittype( @(T2S,T2L,f,S0,C,x) S0 * ( f*exp(-x/T2S) + (1-f)*exp(-x/T2L) ) + C );
         else
            ft = fittype( @(T2S,T2L,f,S0,x) S0 * ( f*exp(-x/T2S) + (1-f)*exp(-x/T2L) ) );
         end
      else
         if biexp_opts.include_offset
            ft = fittype( @(T2S,T2L,S0S,S0L,C,x)  S0S*exp(-x/T2S) + S0L*exp(-x/T2L)  + C );
         else
            ft = fittype( @(T2S,T2L,S0S,S0L,x)    S0S*exp(-x/T2S) + S0L*exp(-x/T2L)  );
         end

      end
   end

   opts = fitoptions(ft);
   opts.Display = 'Off';
   opts.Algorithm = biexp_opts.Algorithm;
   opts.StartPoint = biexp_opts.StartPoint;


   if strcmp(biexp_opts.Algorithm,'Trust-Region')
      if isfield(biexp_opts,'Lower')
         opts.Lower = biexp_opts.Lower;
```

```
        end
        if isfield(biexp_opts,'Upper')
            opts.Upper = biexp_opts.Upper;
        end
    end

    % plot initial params
    %{
      y_init = S0_fixed * ( 0.5*exp(-TE*1.3*(monoexp_params.R2)) + (1-0.5)*exp(-TE*0.7*(monoexp_params.R2)) ) + C_fixed;
      figure;
      hold on;
      plot(TE,signal,'bx')
       plot(TE,y_init,'r-');
      hold off;
      %}

    % Fit model to data.
        [fitresult, gof] = fit( TE, signal, ft,opts);
    bfp = coeffvalues(fitresult); % bfp = bestfit parameters
    coeff_names = coeffnames(fitresult);
    T2S_ind = find(strcmp(coeff_names,'T2S')); T2L_ind = find(strcmp(coeff_names,'T2L')); S0_ind = find(strcmp(coeff_names,'S0')); S0S_ind = find(strcmp(coeff_names,'S0S')); S0L_ind = find(strcmp(coeff_names,'S0L')); C_ind = find(strcmp(coeff_names,'C')); f_ind = find(strcmp(coeff_names,'f'));



    % plot best fit parameters
    if biexp_opts.plot_fit

        TE_plot=[1:0.01:max(TE)];

        if biexp_opts.usef
```

```
    if exist('fixed_params','var')
        beS = S0_fixed * ( bfp(f_ind)*exp(-TE_plot/(bfp(T2S_ind))));
        beL = S0_fixed * ( (1-bfp(f_ind))*exp(-TE_plot/(bfp(T2L_ind))));
        betot = beS + beL + C_fixed;
    else
        beS = bfp(S0_ind) * ( bfp(f_ind)*exp(-TE_plot/bfp(T2S_ind)));
        beL = bfp(S0_ind) * ( (1-bfp(f_ind))*exp(-TE_plot/bfp(T2L_ind)));
        betot = beS + beL + bfp(C_ind);
    end
else
    if exist('fixed_params','var')
        beS = bfp(S0S_ind)*exp(-TE_plot/(bfp(T2S_ind)));
        beL = bfp(S0L_ind)*exp(-TE_plot/(bfp(T2L_ind)));
        betot = beS + beL + C_fixed;
    else
        beS = bfp(S0S_ind)*exp(-TE_plot/bfp(T2S_ind));
        beL = bfp(S0L_ind)*exp(-TE_plot/bfp(T2L_ind));
        betot = beS + beL + bfp(C_ind);
    end
end
model = feval(fitresult,TE_plot); % should equal to betot;

figure;
hold on;

h(1)=plot( TE, signal,'k.');
% h(2)=plot( TE_plot, model,'b-');
h(2)=plot( TE_plot, betot,'b','linewidth',1.5);
if biexp_opts.plot_components
    h(3)=plot( TE_plot, beS,'r--','linewidth',1.5 );
    h(4)=plot( TE_plot, beL,'g--', 'linewidth',1.5);
    h(5)=plot( TE_plot, repmat(bfp(C_ind),[1,length(TE_plot)]),'c--', 'linewidth',1.5);
end
```

```
        legend( h, 'signal', 'model fit', 'T2S', 'T2L', 'C', 'model fit' );
        % Label axes
        xlabel( 'TE','fontsize',16 );
        ylabel( 'Signal Intensity','fontsize',16 );
        % title([sub_name,' ',week_name,': bi-exponential']);
        title('biexponential','fontsize',16);
        set(gca,'fontsize',16);
        hold off;
    end
end
```